

University of Richmond

UR Scholarship Repository

Honors Theses

Student Research

2024

Functionalized Gold Nanoparticles and Halogen Bond Interactions with Neonicotinoid Pesticides

Molly McCuen "Mackey" Sherard

Follow this and additional works at: <https://scholarship.richmond.edu/honors-theses>



Part of the [Biochemistry Commons](#), and the [Molecular Biology Commons](#)

Recommended Citation

Sherard, Molly McCuen "Mackey", "Functionalized Gold Nanoparticles and Halogen Bond Interactions with Neonicotinoid Pesticides" (2024). *Honors Theses*. 1777.

<https://scholarship.richmond.edu/honors-theses/1777>

This Thesis is brought to you for free and open access by the Student Research at UR Scholarship Repository. It has been accepted for inclusion in Honors Theses by an authorized administrator of UR Scholarship Repository. For more information, please contact scholarshiprepository@richmond.edu.

Functionalized Gold Nanoparticles and Halogen Bond Interactions with Neonicotinoid Pesticides

by

Molly McCuen “Mackey” Sherard

Honors Thesis

Submitted to:

Program in Biochemistry and Molecular Biology

University of Richmond

Richmond, VA

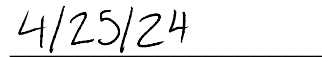
1 May 2024

Advisor: Dr. Michael Leopold

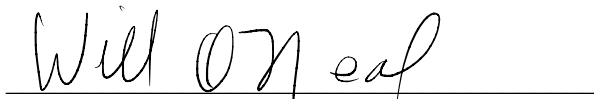
This thesis has been accepted as part of the honors requirements
in the Program in Biochemistry and Molecular Biology.



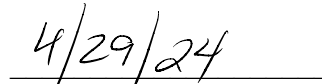
(advisor signature)



(date)



(reader signature)



(date)

Abstract

Neonicotinoid (NN) pesticides have emerged globally as one of the most widely used agricultural tools for protecting crops from pest damage and boosting food production. Unfortunately, some NN compounds, such as extensively employed imidacloprid-based pesticides, have also been identified as likely endangering critical pollinating insects like honey bees. To this end, NN pesticides pose a potential threat to world food supplies. As more countries restrict or prohibit the use of NN pesticides, tools are needed to effectively and quickly identify the presence of NN compounds like imidacloprid on site (e.g., in storage areas on farms or pesticide distribution warehouses). This study represents a proof-of-concept where the colloidal properties of specifically modified gold nanoparticles (Au-NPs) able to engage in the rare intermolecular interaction of halogen bonding (XB) can result in the detection of certain NN compounds. Density functional theory (DFT) and diffusion-ordered NMR spectroscopy (DOSY NMR) are used to explore fundamental XB interactions between strong XB donor structures and NN compounds with the latter found to possess multiple XB-acceptor binding sites. Fundamental understanding of these XB interactions allows for the functionalization of alkanethiolate-stabilized Au-NPs, known as monolayer-protected gold clusters (MPCs), with XB-donor capability (*f*-MPCs). In the presence of certain NN compounds such as imidacloprid, the *f*-MPCs subsequently exhibit visual XB-induced aggregation that is also measured with absorption (UV-Vis) spectroscopy and verified with transmission electron microscopy (TEM) imaging. The demonstrated *f*-MPC-aggregation detection scheme has a number of favorable attributes including quickly reporting the presence of the NN target, requiring only micrograms of suspect material, and being highly selective for imidacloprid, the most prevalent and most important NN insecticide compound. Requiring no instrumentation, the presented methodology can be envisioned as a simple screening test in which dipping a cotton swab of an unknown powder from a surface in a *f*-MPC solution causes *f*-MPCs to aggregate and yield a preliminary indication of imidacloprid presence.

I. Introduction and Background

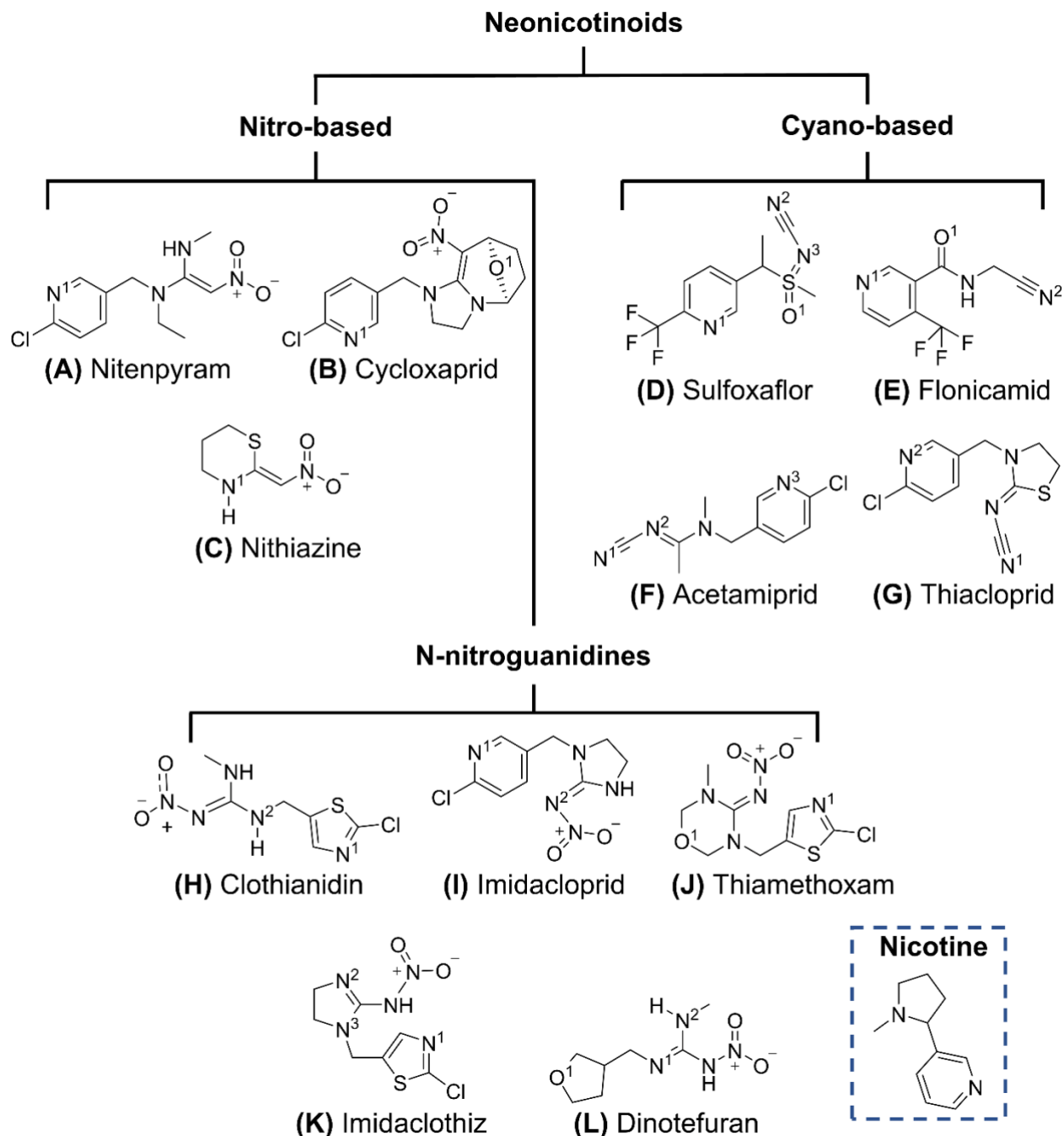
Pollinating insects remain critical to world-wide food production that is needed to meet the needs of the fast-growing global population. Honey bees (*Apis mellifera*) represent the most important group of pollinating insects with ~35% of world crop production, an estimated \$160 billion industry, dependent on their assistance¹⁻⁷ in maintaining a balanced and healthy ecosystem through pollination of both crop-producing and wild plants.¹ Food production is also dependent on chemical pesticides, which provide protection of harvested crops from chewing insects (e.g., plant hoppers, beetles, and moths). Most pesticides work systemically, diffusing throughout all parts of the plant tissues, including nectar and pollen, and thus presenting direct exposure to foraging insects that can carry contaminated materials back to their colony hives.^{4, 8, 9} Governmental authorization of specific pesticide usage is typically preceded by required mortality testing that shows field concentrations of a pesticide are non-lethal to bees.⁸ Despite the recognition of risks to bees and increasing government regulations, the last two decades have seen drastic and continual declines in bee populations across the globe. In the winter of 2007, for example, ~30% of U.S. beekeepers reported rapid and alarming losses of bee colonies, a phenomenon known as colony collapse disorder (CCD).⁶

Scientists have identified a number of contributing factors to declining bee populations and increasing CCD incidents that include habitat loss, invasive species (e.g., murder hornet), and the use of popular pesticides.^{4, 10} Research has already established that repeated exposure even to non-lethal concentrations of pesticides may result in both *direct* adverse effects where pollinating insects' foraging behaviors such as learning, memory, and organizational/communication skills are significantly impaired,^{1, 8, 11} and *indirect* consequences where exposure is linked to an increased vulnerability to virus infection and intestinal parasites (e.g., *Nosema*).¹⁰ As of 2021, most research now affirms that the most widely used class of pesticides are an inherent and unacceptable danger to honey bees, bumble bees, and solitary pollinating bees.^{1, 4, 9, 12}

A class of systemic pesticides known as neonicotinoids (NNs) (**Scheme 1**) now dominates the global agricultural scene.^{4, 5, 13} NNs, literally interpreted as “new nicotine-like” pesticides, are now registered for combating chewing insects in over 120 countries and represent 25% of all insecticide sales worldwide (~\$3.7 billion in 2014).⁴ In the U.S, it is estimated that more than 3.5 million kgs of NNs are applied to crops annually. Perceived as a safer alternative to

organophosphate and carbamate-based pesticides while also offering broad spectrum toxicity, easy application, and high environmental persistence (fewer required treatments), NNs increasingly became the most commonly used commercial insecticide since the pyrethrum-based pesticides (1980s).^{4, 5, 8, 10, 13} Research suggests that NN usage has negative implications for both pollinating insects and human health as the compounds are found in increasing concentrations in drinking water as well as children's spinal fluid, blood, and urine.¹⁴ Additionally, it is now believed that targeted pests are developing resistance to certain NN pesticides, which causes an increase in number and concentration of applications. This increase, in turn, exacerbates the risk to both pollinators and humans.^{2, 3, 13, 15} In recent years, this risk has been recognized with mitigation attempts that include policy adjustments and legislation to slow or reverse the observed trends of declining pollinating insect populations.^{4, 16, 17} With the problems now being acknowledged, it is more critical than ever to develop practical tools to detect NN compounds on-site by non-experts without requiring significant lab instrumentation. As such, research efforts have targeted NN detection, though the methodologies remain very instrumentation and/or personnel dependent^{15, 18-}²¹ including fluorescence methods^{22, 23} and more portable electrochemical techniques that often involve nanomaterials (NMs).^{6, 15, 24, 25} With increasing legal measures to prohibit their use, the development of an easy-to-use, low preparation NN detection system that is usable by non-expert inspectors at manufacturing plants or pesticide storage centers on farms, remains of high interest. As of today, commercial methodologies and materials of this nature are still rare with only a few colorimetric test strips targeting organophosphate and carbonate pesticides.¹⁵

NN compounds (**Scheme 1**) can be sub-classified into three structural categories: N-nitroguanidines (e.g., dinofuran, **Scheme 1-L**), nitromethylenes (e.g., nitenpyram, **Scheme 1-A**), and N-cyanoamidines (e.g., acetamiprid, **Scheme 1-F**) or NN-“like” compounds (e.g., cycloxaprid, **Scheme 1-B**, and sulfoxaflor, **Scheme 1-D**).⁴ While many NN structures share chloropyridine or furan moieties, it is the electron-rich functional groups (nitromethylene, nitroimine, and cyanoimine) that form the basis of their effectiveness as pesticides and that make them of interest in our study. Once ingested by a pest insect, NNs selectively and irreversibly bind to the nicotinic acetylcholine receptor (nAChR) which triggers nerve signaling. Acetylcholine esterase normally metabolizes acetylcholine but cannot break down the NN compounds, which causes sustained nerve stimulation at the receptor and eventually leads to paralysis and insect



Scheme 1. Chemical structures of neonicotinoid pesticides and nicotine.

death. The nAChRs are present in significantly greater amounts in insects making NNs ~5-fold more selective in targeting insects compared to other pesticides.⁴

Chemical screening methods that can be used on-site for fast indication of the presence of a targeted compound are often associated with the forensic chemistry field and known as

presumptive tests (e.g., Marquis test for opioid detection, luminol or leucomomalachite green for blood detection, Meisenheimer and Griess tests for gun-shot residues).²⁶⁻³³ Many of these commercialized tests are colorimetric or spectroscopic based and used in the field to give a preliminary indication of the presence of specific chemicals without requiring significant time, trained personnel, or costly instrumentation. A colorimetric NP system was developed as an on-site testing method for determining the “age” and chemical composition of whiskey in wooden casks.³⁴ Presumptive tests can be prone to occasional false positives and always require secondary confirmatory lab analysis (e.g., GC-MS). That said, they remain crucial on-site tools for identifying or narrowing unknown substances to a class of compounds, identifying specific chemical presence, or reporting solution conditions.^{26, 27}

All chemical sensing methods require a fundamental interaction of significant strength to be established between the molecules of interest and the sensing platform. Recent work in our group has focused on exploring halogen bonding (XB) as a potential interaction to be exploited for such a purpose. XB involves a positive region of electron deficiency (δ^+), known as a sigma (σ) hole found on a polarized halogen atom within one molecule (XB donor) interacting with an electron-rich region (δ^-) on another molecule (XB acceptor).³⁵⁻³⁷ Molecular structure motifs, such as iodo-perfluoro aromatic compounds, offer optimization of the σ -hole size (**Figure 1A**) and thus XB-donor strength.³⁸ Here, the σ -hole of iodopentafluorobenzene (IPFB) at the iodine atom is created because of electron-withdrawing fluorine substitutions at multiple aromatic positions. Recently, we have reported the synthesis of thiolate ligands featuring an optimized XB-donor moiety ($-\text{C}_6\text{F}_4\text{I}$) featuring a σ -hole of significant strength. The thiol group opposite the XB-donor moiety on the ligand allows for the functionalization of the ligands onto the periphery of alkanethiolate-protected Au-NPs, known as monolayer protected clusters (MPCs),³⁹ to create XB-donor functionalized MPCs (*f*-MPCs). By harnessing XB-donor capabilities to Au-NPs, the unique properties of Au-NPs, such as their surface plasmon resonance, can be utilized to directly observe XB interactions with XB-acceptor molecules.⁴⁰

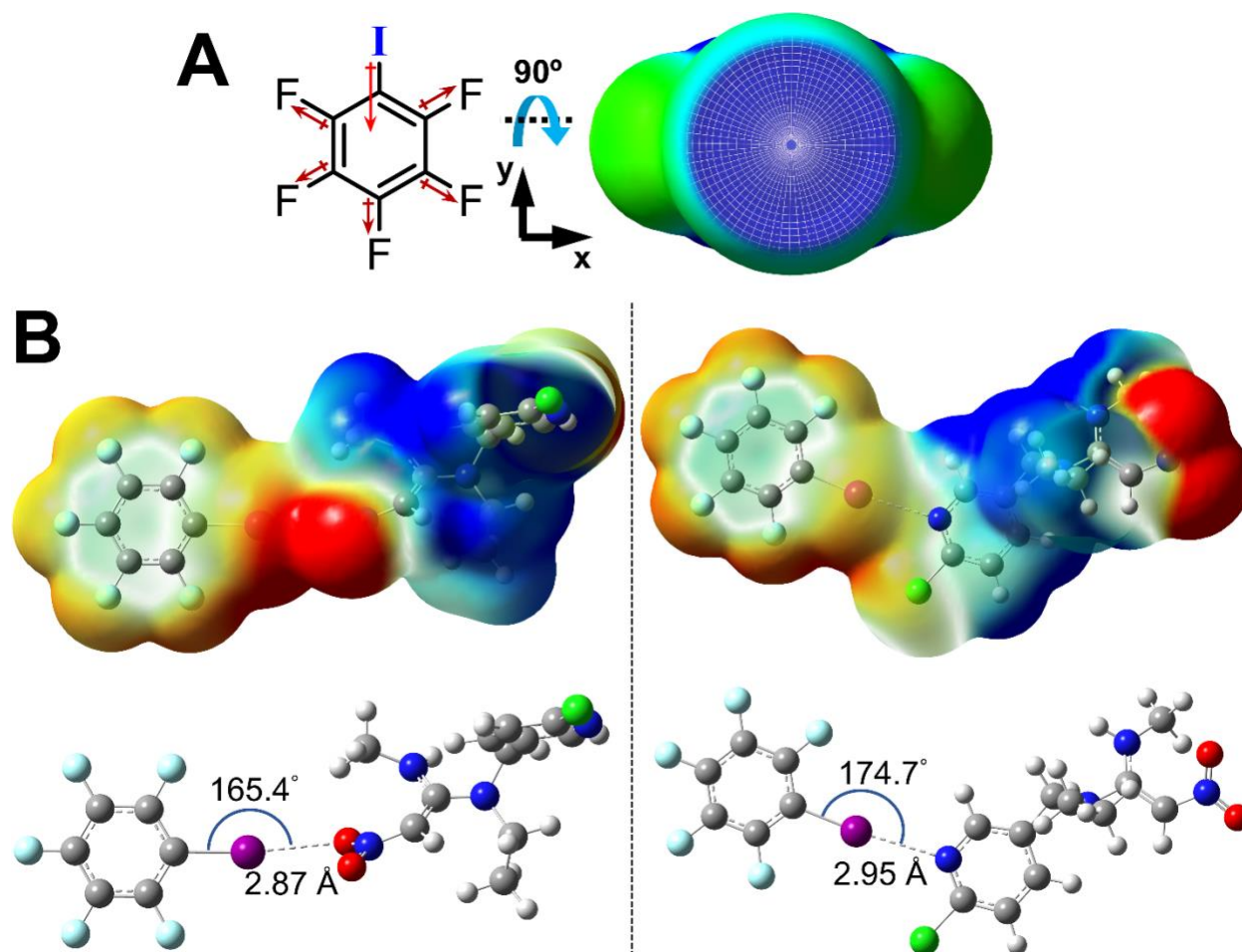


Figure 1. (A) IPFB represents a model XB donor molecule in which (left) electron-withdrawing fluorines on the aromatic ring create the overall dipole that results in an electron deficient region known as the “ σ -hole” at the iodine atom; the σ -hole is visualized from left to right after rotating IPFB’s structure 90° about the x-axis. (B) DFT-generated, space-filled electrostatic potential maps (top) and geometry-optimized structures (bottom) of XB adducts of IPFB (XB donor) with nitenpyram (XB acceptor) at the NO₂ (left) and N¹ (right) binding sites. Note: Geometry-optimized XB adducts of IPFB with other NNs are in Supporting Information (Figures S1–S20).

In this paper, XB interactions between *f*-MPCs (XB donors) and XB-acceptor sites on NN compounds with are explored. While XB interactions between molecules have been extensively explored using computational tools, the translation of theoretical understanding of XB interactions to a functional chemical system is a more rarely achieved phenomenon. DFT and diffusion-ordered NMR spectroscopy (DOSY) are used to gain a greater fundamental understanding of interactions between electron-rich functional groups found on XB-acceptor NN compounds (e.g.,

nitromethylene, nitroimine, and cyanoimine—**Scheme 1**) and the XB-donor IPFB. XB interactions, along with hydrogen bonding (HB) interactions, have both already been identified as potentially playing a role in NN binding to insect nAChRs,⁴¹ which makes XB an interaction to explore in this capacity. Herein, we demonstrate that *f*-MPCs with XB-donor capability can detect the presence NN compounds via XB-induced aggregation of the Au-NPs that is visually observable and further investigated using spectroscopy (NMR and UV-Vis), dynamic light scattering, and electron microscopy—a proof-of-concept methodology with important environmental implications.

II. Experimental Details

A. Materials and Instrumentation. Chemical materials were purchased in highest available purity (Millipore-Sigma, Oakwood Chemical, and TCI Chemicals), including NN compounds (Cayman Chemical, A2B Chem, and LGC Standards), and used without further purification or modification. NN compounds that were not tested were not commercially available at the time of the study. All aqueous solutions and experiments were prepared or conducted with 18.2 M Ω ·cm ultrapurified (UP) water. A high-performance supercomputer (SPYDUR) was used for density functional theory (DFT) calculations. UV-Vis spectroscopy data was collected on an Agilent 8453 Photodiode Array Spectrophotometer to characterize *unf*-MPC and *f*-MPC solutions and *f*-MPCs' XB-induced aggregation events. Transmission electron microscopy (TEM; JEOL 1010 with Advanced Microscopy Techniques XR-100 CCD image collection) was operated at 80–100 kV for assessment of the as-prepared MPC's average diameter as well as to visualize XB-induced *f*-MPC aggregation events. NMR spectroscopy was carried out using a Bruker Avance III (400 MHz) spectrometer with chemical shifts reported relative to tetramethylsilane (TMS) and trichlorofluoromethane (CFCl₃) for ¹H and ¹⁹F NMR, respectively. NMR spectra were subsequently analyzed using Mestrelab's MestreNova (v14.2) software. Dynamic light scattering (DLS) measurements were taken on a Malvern Instrument (Model ZEN3600) at Virginia Commonwealth University (Carpenter Research Lab).

B. Computational Methodology. As in prior reports^{38, 40}, DFT calculations of XB interactions, carried out using the Gaussian16 software⁴², use the M06 functional⁴³ with the cc-pVDZ (geometry optimization)⁴⁴ and cc-pVTZ (single point) basis sets⁴⁵ to estimate energy of interaction (ΔE_{int}) or binding energy, XB bond lengths ($X\cdots B$), and XB bond angles ($R-X\cdots B$). In this study, relative comparisons rather than absolute energies were the goals of computational analyses. More negative ΔE_{int} values, shorter $X\cdots B$ bond lengths, more linear (180°) $R-X\cdots B$ bond angles indicated stronger XB interactions.⁴⁶ The optimized geometries of all XB adducts were visualized using the GaussView program.⁴⁷ Additional experimental details of computational measurements for this study are included in Supporting Information (p. S2).

C. NMR Measurements. As in prior studies,⁴⁰ diffusion-ordered NMR spectroscopy (DOSY NMR) was used to measure the diffusion coefficients (D) of NN compounds (XB acceptors) and solvent molecules (control) in the presence and absence of either XB donor molecules like IPFB, control compound perfluorotoluene (non-XB donor), or *unf*-MPC and *f*-MPC solutions. As in previous measurements of this nature for XB interactions,^{38, 40} samples were prepared with equal concentrations of either IPFB (XB donor) or PFT (non-XB-donor control) and NN compounds (imidacloprid, nitenpyram, and thiachloprid) before transferring to 7 inch–5 mm heavy-wall NMR tubes (Norell) for DOSY NMR measurements. Similarly, *f*-MPC and *unf*-MPC solutions (whose concentration is equivalent to $\text{Abs}_{@518\text{nm}} = 0.2$ a.u. in THF or toluene) were well-mixed with either 11mM nitenpyram, 50mM imidacloprid, or 100mM thiachloprid before transferring to heavy-wall NMR tubes (Norell) for DOSY NMR measurements. Additional DOSY NMR experimental parameters are provided in Supporting Information (p. S2).

D. Gold Nanoparticle Synthesis and Functionalization. Hexanethiolate-protected Au-NPs, also known as C6-MPCs, were synthesized via a modified Brust-Schiffrin reaction⁴⁸ and characterized as previously described in significant detail.⁴⁰ As in prior reports utilizing the same type of MPCs, characterization (UV-Vis spectroscopy, NMR spectroscopy, and TEM imaging with histogram analysis) of C6-MPCs revealed an *average* diameter of 4.46 (± 0.08) nm and a composition of $\text{Au}_{2951}(\text{C6})_{876}$.⁴⁹

C6-MPCs were converted to XB-donor functionalized MPCs (*f*-MPCs) via established place-exchange reactions⁵⁰ with a previously in-house synthesized XB-donor ligand.⁴⁰ The ligand

features a 2,3,5,6-tetrafluoriodobenzene moiety ($-C_6F_4I$) that has been shown in a prior study to engage in strong XB interactions.^{38, 40} Place-exchanged (or functionalized) MPCs were purified via size-exclusion chromatography (SEC) as reported in the literature⁵¹ and previously replicated in our laboratory.⁴⁰ In brief, the successful formation of *f*-MPCs bearing peripheral XB-donor ligands with $-C_6F_4I$ moieties was confirmed using 1H and ^{19}F NMR measurements after iodine degradation that liberates the MPCs peripheral ligands as disulfides, known as the iodine “death” reactions.⁵⁰ From 1H NMR analysis, the *average* composition of the *f*-MPCs was estimated to be $Au_{2951}(C_6)_{438}(\text{ligand}-C_6F_4I)_{438}$ (equivalent to 50% degree of functionalization).⁴⁰

E. Nanoparticle (MPC) Aggregation Experiments. The aggregation of *f*-MPCs via XB interactions or lack thereof for *unf*-MPCs was monitored and characterized via UV-Vis spectroscopy, visual photography, DLS, and TEM imaging. For a typical sample, 600 μL of a *f*-MPC (or *unf*-MPC) solution (i.e., $Abs_{@518nm} = 0.2$ a.u. in THF or toluene) was placed in a 0.75 mL-capacity, 10 x 2 mm pathlength, screw-capped, quartz cuvette (Type 46, FireflySci). As demonstrated in the literature, gold NPs of this diameter correspond to an estimated extinction coefficient of $7.06 \times 10^6 \text{ M}^{-1}\text{cm}^{-1}$ which Beer’s Law translates to ~ 28 nM or 70 nM for MPC solutions with $Abs_{@518nm} = 0.2$ or 0.5 a.u., respectively.⁵² UV-Vis spectra of *f*-MPC (XB donor) or *unf*-MPC (non-XB material) solutions in THF or toluene (solvent selection promotes strong XB interactions³⁸ and the solubility of NNs, *f*-MPCs, and *unf*-MPCs) were measured before and after the addition of XB-acceptor molecules (NN compounds or positive-control molecule DABCO) at different time intervals. Carefully measured masses of each tested NN compound were added to the *f*-MPC solution in the cuvette. Cuvettes were cleaned with aqua regia in between samples. **Caution:** *Aqua regia, a 3:1 ratio of concentrated HCl/HNO₃, is extremely dangerous, requires appropriate PPE, and should never be placed in a sealed container.* Visual changes to the solution were recorded and compared to as-prepared *f*-MPC (or *unf*-MPC) solutions without added XB acceptors. At various time intervals, aliquots (5 μL) of the *f*- or *unf*-MPC–NN mixtures were extracted, drop-cast on 200-mesh Formvar-coated (Electron Microscopy Sciences) or carbon-coated copper (SPI Supplies) TEM grids, allowed to dry inverted, and then imaged. *Note: carbon-coated copper grids were more effective with aggregated samples as the bulk material often caused heating issues with the microscope electron beam.* Each TEM grid was imaged ≥ 5 different areas and all used for a composite characterization of the MPC materials at that stage of the analysis.

Interferent testing and limit of detection (LOD) determinations used a similar methodology as described above. UV-Vis spectra of *f*-MPC solutions (XB donor) were measured before and after addition of 50 mM interferent compounds (including acetamiprid, clothianidin, parathion, chlorpyrifos, carbaryl, dioctyl phthalate) in the presence or absence of 50 mM imidacloprid. For minimal analyte concentration detectable, UV-Vis spectra of *f*-MPC solutions ($Abs_{@518nm} = 0.2$ a.u. in THF or toluene an estimated concentration of ~ 28 nM)⁵² were collected before and after the smallest amount of imidacloprid or nitenpyram that yielded a measurable and repeatable reduction in SPR intensity.

III. Results and Discussion

A. Density Functional Theory Calculations. When exploring specific molecular interactions of an entire class of molecules, computational methods serve as an instructive tool to inform subsequent experimental design and execution in the lab. In the case of neonicotinoids (NNs) engaging in potential XB interactions with a model XB donor (e.g., iodopentafluorobenzene or IPFB), computational modeling with density functional theory (DFT) allowed for evaluation of several interaction parameters of each XB adduct: interaction energy (ΔE_{int}), XB “bond” length ($X\bullet\bullet B$) or distance, and XB “bond” angle ($R-X\bullet\bullet B$, θ_{XB}). Stronger XB interactions should correlate with more negative ΔE_{int} values, shorter $X\bullet\bullet B$ distances, and more linear $R-X\bullet\bullet B$ angles ($\theta_{XB} \sim 180^\circ$). **Figure 1B** provides an example of the computationally modeled XB adduct of IPFB (XB donor) with the NN compound nitenpyram (XB acceptor) (**Scheme 1–A**). It is immediately notable from DFT evaluation of the IPFB–nitenpyram adduct that this particular NN compound has two potential XB-acceptor sites for XB interactions with IPFB or other XB donors. DFT results of the IPFB–nitenpyram adduct show significant XB taking place at the nitro (NO_2) group ($\Delta E_{int} = -11.38$ kcal/mol) *and* at the nitrogen (N^1) group ($\Delta E_{int} = -5.99$ kcal/mol). To place these values in context, an XB adduct of IPFB (XB donor) with tributylphosphine oxide (Bu_3PO , XB acceptor), established in prior work from our lab, exhibited a DFT-measured ΔE_{int} of -10.95 kcal/mol.^{38, 40} For context of intermolecular interaction strength, computational measurements (quantum mechanical calculations) show that hydrogen bonding (HB) within simple adducts of this nature exhibited ΔE_{int} values ranging between 7 and 11 kJ/mol (~ 1.7 – 2.6 kcal/mol).⁵³ While ΔE_{int} values energies provided guidance on

XB interaction strength, we note that DFT-measured R–X••B angles at nitro groups (Fig. 1B, *left*) were observed to deviate significantly from 180° because they are measured from one of the nitro oxygens rather than the midpoint of the bifurcated interaction with both oxygens. R–X••B angles measured at the N¹ acceptor site (Fig. 1B, *right*) were consistently measured closer to 180° because the interaction involved only one lone pair of electrons on the nitrogen with the smaller deviation attributable to other intermolecular interactions and steric effects present in molecules of this complexity. Optimized geometries of other NN compounds engaging in XB interactions with IPFB are provided in the Supporting Information (Figures S1–S20), and a summary of all interaction parameters of all IPFB–NN adducts is provided in **Table 1**. DFT analysis indicates that *all* the NNs explored in this work possess at least two XB-acceptor sites that could interact with the XB donor IPFB. The presence of two or more potentially strong XB-acceptor sites on the NN compounds is highly relevant to their proposed detection via functionalized NP (*f*-MPC)-based aggregation. For example, HB-capable ligands affixed to citrate-stabilized Au-NPs were shown able to use HB's intermolecular interaction strength to detect the molecule melamine in solution via NP aggregation.³⁰ Similarly, in our prior work investigating XB interactions with Au-NPs showed that a model molecule with two XB-acceptor sites known as 1,4-diazabicyclo[2.2.2]octane (DABCO) was able to engage in strong enough XB interactions with *f*-MPCs featuring XB-donor –C₆F₄I moieties to induce an NP aggregation event in solution.⁴⁰ As described in the next section, DOSY NMR measurements were successfully employed to confirm the XB interactions in the *f*-MPCs–DABCO mixture.⁴⁰ For the current study, the collection of DFT results (**Table 1**) was then used to narrow the focus to the detection of specific NN compounds of high relevance and serve as proof-of-concept for establishing XB as a viable interaction to be exploited for their molecular detection.

Table 1. DFT Computational Interaction Energies (ΔE_{int}), Bond Distances (XBD), and Bond Angles of XB Adducts of XB Donor IPFB and Various Neonicotinoid Compounds (XB Acceptors).

Neonicotinoid	XB Acceptor Sites	ΔE_{int} (kcal/mol) ^a	X••B Distance (Å)	R–X••B Angle (θ)
A	Nitenpyram	NO ₂	2.87	165.4
		N ¹	2.95	174.7
B	Cycloxaprid	N ¹	2.94	174.3
		O ¹	2.90	175.4
		NO ₂	2.86	167.3
C	Nithiazine	N ¹	3.07	176.0
		NO ₂	2.90	173.9
D	Sulfoxaflor	N ¹	3.01	173.7
		N ²	2.99	165.2
		N ³	3.06	164.9
		O ¹	2.94	166.2
E	Flonicamid	N ¹	2.94	177.9
		N ²	3.04	179.2
		O ¹	2.98	170.3
F	Acetamiprid	N ¹	2.93	178.5
		N ²	3.09	178.0
		N ³	2.96	173.9
G	Thiacloprid	N ¹	2.94	178.7
		N ²	3.08	171.0
H	Clothianidin	NO ₂	2.94	174.1
		N ¹	2.98	177.4
		N ²	3.17	164.2
I	Imidacloprid	NO ₂	2.92	172.8
		N ¹	2.95	173.5
		N ²	3.31	166.1
J	Thiamethoxam	NO ₂	2.90	171.3
		N ¹	2.95	178.0
		O ¹	2.95	174.6
K	Imidaclothiz	N ¹	2.96	178.4
		N ²	2.91	172.8
		N ³	3.19	173.2
		NO ₂	3.01	174.9
L	Dinotefuran	NO ₂	3.02	164.3
		N ¹	2.93	175.3
		N ²	3.00	171.0
		O ¹	2.82	175.4

Notes: ^a $\Delta E_{\text{int}} = E(\text{XB adduct}) - [E(\text{XB donor}) + E(\text{XB acceptor})]$ (gas-phase values). DFT functional and basis sets: M06-2X/cc-pVTZ//M06-2X/cc-pVDZ.

B. DOSY NMR Measurements of XB Interactions. Prior work in our group established diffusion-ordered NMR spectroscopy (DOSY NMR) as a feasible method to detect XB interactions and quantitate their strength between equimolar mixtures of XB donor and XB acceptor molecules in solution.⁴⁰ In principle, DOSY NMR-measured diffusion coefficients (D) of XB-acceptor molecules (e.g., NN compounds) should indicate significantly slower diffusion when they engage in XB interactions with a strong XB donor molecule like IPFB.⁴⁰ In this study, a limited number of DOSY NMR measurements of this nature were conducted between IPFB and representative molecules from each NN sub-class (**Scheme 1**) including nitenpyram (nitro-based NNs), imidacloprid (N-nitroguanidine-based NNs) and thiacloprid (cyano-based NNs). Results from these measurements and the corresponding control experiments are summarized in **Table 2** and in the Supporting Information (Table S1) (i.e., thiamethoxam system). The corresponding ¹H NMR spectra of the tested NN compounds are provided in the Supporting Information (Figures S21–S22). For the following discussion of DOSY NMR results, it is helpful to refer to the **experiment number (#)** in the first column of **Table 2** where experiment **#1–6**, **#7–12**, and **#13–18** examine the XB adducts of IPFB with nitenpyram, imidacloprid, and thiacloprid, respectively. For all the systems tested, log D values represent the relative diffusion (mobility) rate of the targeted molecules, with more negative values indicating slower diffusion/low mobility due to the presence of additional intermolecular interactions (i.e., XB interactions). For each NN system, in addition to interactions with IPFB, two major control measurements were conducted with perfluorotoluene (PFT) as a non-XB donor (i.e., a molecule of similar size/structure that does not engage in strong XB interactions) and solvent molecules (which were expected to remain relatively constant across the different experiments).

Experiments **#1–6** (**Table 2**) focus on nitenpyram in toluene in the presence and absence of IPFB or PFT. DOSY NMR measurements of ¹H NMR signals of nitenpyram by itself and in the presence of PFT (experiments **#1 vs. #3**) show similar values of $-8.78 (\pm 0.04)$ and $-8.80 (\pm 0.03)$. Notably, in the presence of IPFB (experiment **#2**), nitenpyram's diffusion is notably slower with a measured log D of $-8.86 (\pm 0.04)$. These results suggest that IPFB and nitenpyram engage in specific, strong XB interactions, further bolstered by the results of solvent control experiments **#4–6** that show nearly identical log D values for protonated toluene in the same systems. The same trends are observed for the other NN systems as well. In experiments **#7–9**, imidacloprid (**Scheme 1–I**) diffuses more slowly in the presence of IPFB (-8.84 ± 0.04) than in IPFB's absence (-8.76

Table 2. Diffusion-Ordered Spectroscopy (DOSY) NMR Measurements of Diffusion Coefficients (D) in Various Experimental XB and Control Systems.

#	XB Acceptor	Solvent	XB Donor	Target	Log D (log(m ² /sec))
1			None		-8.78 (±0.04)
2	Nitenpyram (11 mM)	Toluene-d ₈	IPFB (11 mM)	¹ H Nitenpyram	-8.86 (±0.04)
3			PFT (11 mM)		-8.80 (±0.03)
4			None		-8.59 (±0.02)
5	Imidacloprid (50 mM)	Tetrahydrofuran-d ₈	IPFB (11 mM)	¹ H Toluene-d ₇ h ₁	-8.62 (±0.03)
6			PFT (11 mM)		-8.60 (±0.03)
7			None		-8.76 (±0.04)
8	Thiacloprid (100 mM)	Tetrahydrofuran-d ₈	IPFB (50 mM)	¹ H Imidacloprid	-8.84 (±0.04)
9			PFT (50 mM)		-8.77 (±0.04)
10			None		-8.53 (±0.03)
11	Thiacloprid (100 mM)	Tetrahydrofuran-d ₈	IPFB (50 mM)	¹ H Tetrahydrofuran-d ₇ h ₁	-8.52 (±0.02)
12			PFT (50 mM)		-8.52 (±0.04)
13			None		-8.75 (±0.04)
14	Thiacloprid (100 mM)	Tetrahydrofuran-d ₈	IPFB (100 mM)	¹ H Thiacloprid	-8.77 (±0.05)
15			PFT (100 mM)		-8.76 (±0.04)
16			None		-8.52 (±0.02)
17	Thiacloprid (100 mM)	Tetrahydrofuran-d ₈	IPFB (100 mM)	¹ H Tetrahydrofuran-d ₇ h ₁	-8.52 (±0.05)
18			PFT (100 mM)		-8.53 (±0.04)

Note: ¹H toluene-d₇h₁ and ¹H tetrahydrofuran-d₇h₁ refers to the ¹H NMR residual solvent signals of toluene and tetrahydrofuran molecules, respectively, that contain one less deuterium atom than toluene-d₈ and tetrahydrofuran-d₈, respectively.

± 0.04) or in PFT's presence (non XB-donor) (-8.77 ± 0.04). The solvent controls again showed nearly identical log D values for protonated tetrahydrofuran (THF) in the same systems (experiments #10–12). Similar results were obtained for the thiacloprid (**Scheme 1–G**) system, though we note that the XB interactions between IPFB and thiacloprid were less substantial. Taken collectively, the DOSY experiments on these representative examples reinforce the results of the DFT calculations indicating that these molecules can engage in XB interactions. The question, however, remained as to whether such intermolecular interactions were strong enough to be harnessed for a specific purpose or application.

C. Detection of Neonicotinoid Compounds with XB-Capable Functionalized Au-NPs – Aggregation Model. Of all NN compounds, imidacloprid or (2E)-1-((6-chloro-3-pyridinyl)methyl)-N-nitro-2-imidazolidinimine (**Scheme 1–E**), developed by Bayer-CropScience in the mid-1990s, remains one of the most successful and widely utilized compounds of the group.^{4,5} On a global scale, the usage of imidacloprid, which features chloropyridine and nitroguanidine moieties, as a pesticide is second only to that of glyphosphate.^{54,55} Additionally, imidacloprid is widely used in veterinary medicine as the main active ingredient in a number of prescribed topical treatments for flea, tick, and heartworm prevention/treatment (e.g., Advantage-Multi®, Advantix®, Seresto®).⁵⁶ As previously mentioned for NN compounds in general, the advantage of imidacloprid as a pesticide stems from its easy application (e.g., soil drenching, trunk injection, spraying), environmental persistence (highly leachable with a half-life of 100–1250 days), and well-documented acute toxicity toward pest insects (EC_{50} of $\sim 0.86 \mu\text{M}$ for insect nAChRs vs. two orders of magnitude higher for mammals).⁴ Unfortunately, imidacloprid has also been identified as one of the primary NN chemicals thought to negatively impact bee populations^{1,57} as well as having potential long-term effects on mammals.⁴ In 2013, in direct response to declining honey bee populations, the EU halted the use of imidacloprid on corn fields and identified the compound as a neurotoxin while the U.S. EPA conducted a 2020 study on imidacloprid's impact on human health.⁴ Concerns about imidacloprid were heightened as it started to be found in drinking water (not regulated), fresh-water streams (Canada), and was prevalent in food crops.⁴ Simultaneously, studies involving mouse models showed imidacloprid exposure related to reproduction development defects (i.e., teratogenicity effects), motor activity decline, and hepatotoxicity.^{4,10} Because of its prevalent usage globally, environmental

persistence, and emergence in scientific literature regarding potential detrimental health effects, the development of a detection method for imidacloprid represents one of the most significant goals in this area of study, particularly if the method is fast and executable in the field by non-experts.^{6, 15, 25} As such, imidacloprid is a major target molecule for our proposed XB-capable *f*-MPC detection scheme.

Structural DFT calculations of imidacloprid (**Table 1–I**) show that, like many of the NN compounds examined, it exhibits three potential XB-acceptor binding sites. According to DFT calculations, sulfoxaflor, imidaclothiz, and dinotefuran (**Table 1–D, K, and L**, respectively) have four potential XB-acceptor sites while nitenpyram and thiacloprid (**Table 1–A and G**) have only two potential XB-acceptor sites. In the case of imidacloprid, DFT calculations identify three nearly equally strong XB-acceptor sites on the molecule: N¹ in the chloropyridine group, N² in the nitroguanidine group, and the terminal nitro (NO₂) group. In theory, if each XB-acceptor site could strongly engage with a XB-donor moiety that can be easily monitored, the imidacloprid molecule could be detected via XB interactions (see below).

Alkanethiolate-stabilized Au-NPs or MPCs are well-known for their stability in different solvents, ease of modification, and distinctive optical properties, including a strong surface plasmon resonance (SPR) band that can be readily observed using UV-Vis spectroscopy.³⁹ The SPR band observed with larger MPCs is a surface phenomenon captured when the oscillation of the collective electrons at the surface of the gold core comprising the Au-NPs matches the frequency of incident light and causes a broad absorption band in the visible region of the electromagnetic spectrum. Over the past two decades, research has established that the SPR band's intensity and maximum absorbance (λ_{max}) are specific to certain NP characteristics including core size and composition, gold surface modifiers, and interparticle spacing, the latter being most critical to the current study.⁴⁰ Hexanethiolate-protected Au-NPs or C6-MPCs were prepared with an initial *average* composition of Au₂₉₅₁(C6)₈₇₆ and average diameter of 4.46 (± 0.08) nm (**Figure 2A**) before surface-functionalization with an in-house prepared XB-donor ligand (**Figure 2B**) via well-known place exchange reactions⁴⁰ to yield functionalized MPCs (*f*-MPCs) with an *average* composition of Au₂₉₅₁(C6)₄₃₈(ligand–C₆F₄I)₄₃₈. Notably, the *f*-MPCs feature XB-donor –C₆F₄I moieties extending from the MPC's periphery into solution to facilitate XB interactions with XB-acceptor molecules. **Figure 2C** shows the characteristic SPR band at 518 nm of C6-MPCs (referred to as unfunctionalized MPCs (*unf*-MPCs) hereafter) red shifts slightly upon the

functionalization of XB-donor ligands to form *f*-MPCs. Both the UV-Vis spectra of *unf*-MPCs and *f*-MPCs are also compared that of imidacloprid, which has nearly zero absorbance after 425

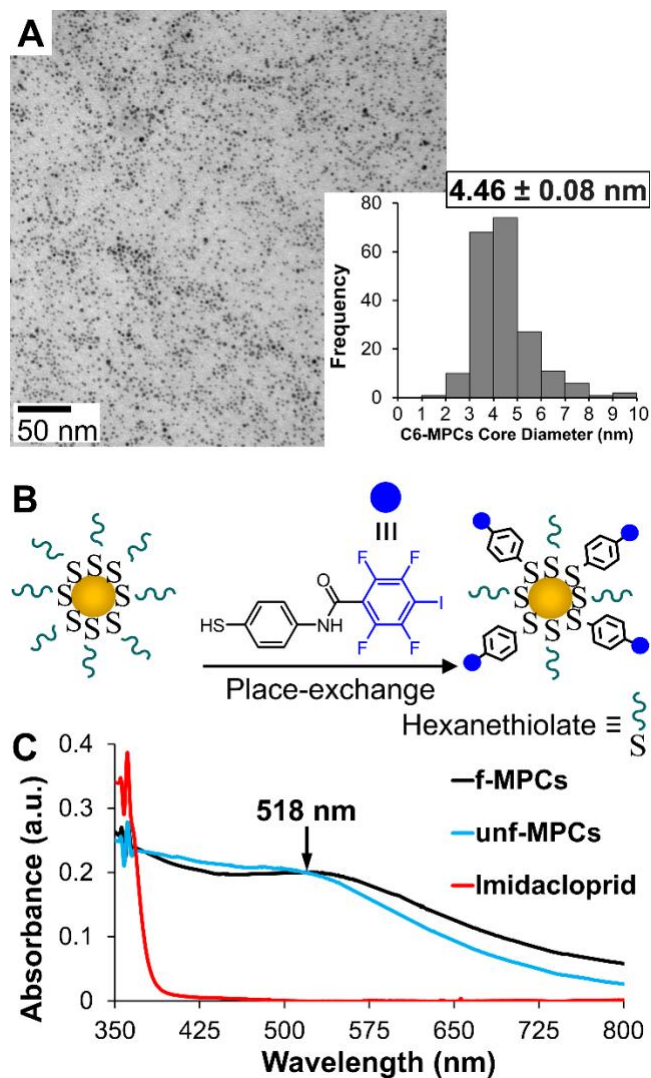
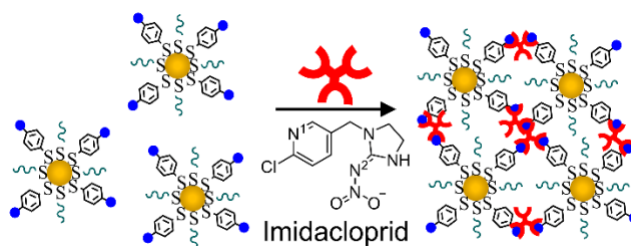


Figure 2. (A) Transmission electron microscopy (TEM) imaging and histogram analysis (inset) of *average* core diameter of as-prepared C6-MPCs (or *unf*-MPCs). (B) Schematic representation of the functionalization of C6-MPCs with XB-donor ligand via place-exchange reactions that results in *f*-MPCs with XB-donor capabilities. (C) UV-Vis spectra of *unf*-MPCs and *f*-MPCs in toluene with characteristic surface plasmon bands at ~ 518 nm ($Abs_{@518} = 0.20$ a.u.) as well as the spectrum of imidacloprid (50 mM) in THF.

nm. UV-Vis spectra of all the NNs examined in this study are provided in the Supporting Information (Figures S23–S27) for reference.

It was hypothesized that imidacloprid's three potential XB-acceptor binding sites (identified by DFT calculations) would form XB interactions with multiple *f*-MPCs simultaneously via the XB-donor –C₆F₄I moieties. Engaging the multiple-site XB interactions should, in turn, decrease interparticle spacing between multiple *f*-MPCs and lead to NP agglomeration and eventual aggregation. In the proposed experiment (**Scheme 2**), the addition of imidacloprid to a *f*-MPC solution should result in the disappearance and/or significant red shift of the SPR band, which is consistent with other NP-based aggregation events in the literature.^{30-32, 40,}



Scheme 2. Illustration of aggregation events upon exposure of *f*-MPCs (XB donor) to imidacloprid (XB acceptor).

^{58, 59} **Figure 3A** shows the UV-vis spectra of the *f*-MPC solution in THF after the addition of imidacloprid. When imidacloprid was initially added to the *f*-MPC solution, the spectral signature of imidacloprid and the SPR band (**Fig. 3**) of *f*-MPCs were both visibly evident. However, upon mixing, there were already an immediate red shift and a corresponding decrease in absorbance of *f*-MPCs' SPR band's λ_{max} . Both responses are consistent with the agglomeration of *f*-MPCs in solution due to diminished interparticle spacing that,⁴⁰ in this case, was instigated by XB interactions between *f*-MPCs and imidacloprid. Over time, this XB-induced *f*-MPC agglomeration resulted in significant aggregation, with evident precipitation of aggregated *f*-MPCs on the bottom of the cuvette (**Figure 3C, left**). **Figures 3B** and **C** show the expected TEM images of independent *f*-MPCs and aggregated *f*-MPCs before and 1 day after the addition of imidacloprid, respectively. TEM images of aggregated *f*-MPCs with imidacloprid after 2 minutes are provided in the Supporting Information (Figure S28). Over longer periods of time, aggregated *f*-MPCs eventually precipitated out of solution completely and, if agitated, the UV-Vis spectrum temporarily reflected

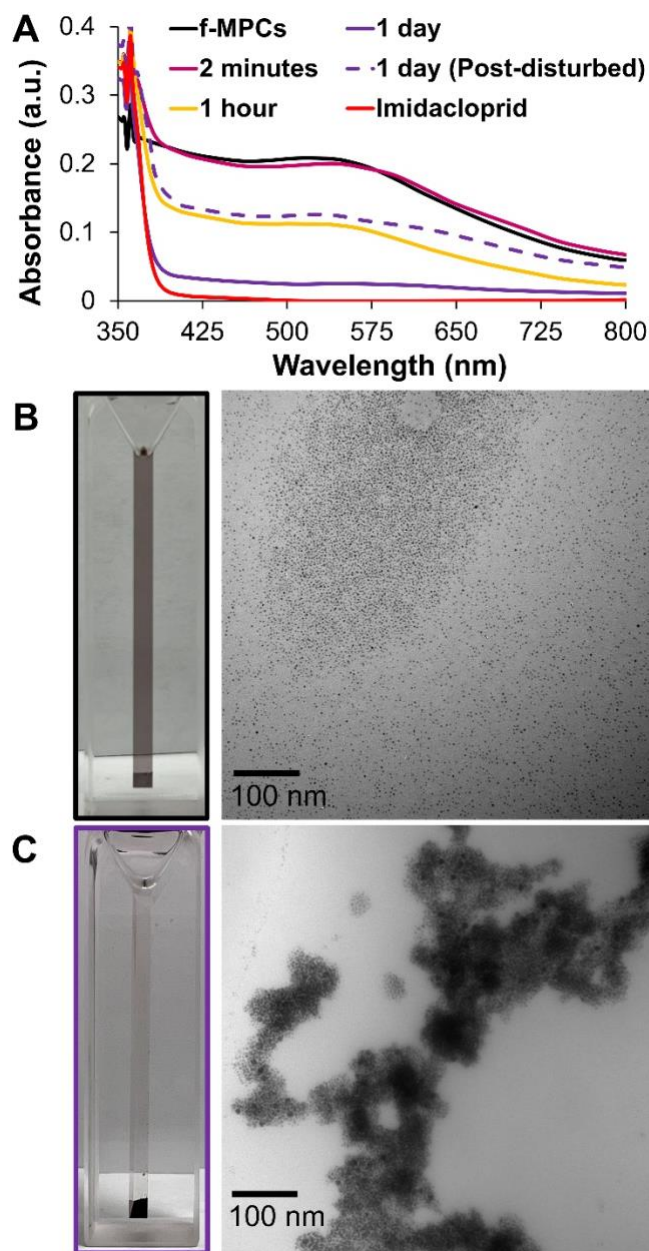


Figure 3. (A) UV-Vis spectra of *f*-MPCs in THF upon exposure to imidacloprid (50 mM) over time. (B, C) TEM images (right) with visual pictures (left) of *f*-MPCs (B) before and (C) 1 day after the addition of imidacloprid (50 mM). The dashed UV-Vis spectrum in (A) was taken briefly after the temporary resuspension of precipitated *f*-MPC aggregates at the bottom of the cuvette (after 1 day).

the resuspension of *f*-MPC aggregates that precipitated once again in a matter of minutes (Figure 3A, dashed UV-Vis spectrum).

As a natural extension of the study, it was of interest to explore if the *f*-MPCs would successfully detect other neonicotinoids that had either (a) similar structures to imidacloprid (e.g., clothianidin, thiamethoxam) or (b) different numbers of potential XB-acceptor sites (see below). Regarding the latter factor, nitenpyram (**Scheme 1–A**) was targeted. Also developed in the mid-1990s (Sumitomo Chemical Takeda Agro Co.), nitenpyram presents a fitting complementary NN compound for detection. While not nearly as widely used as imidacloprid, nitenpyram, featuring chloropyridine and nitromethylene groups, is another NN in the sub-class of nitro-based NNs that are known to be more toxic than their cyano-family counterparts (**Scheme 1**). With a shorter half-life (weeks), moderate leaching, greater water solubility, and higher vapor pressure, nitenpyram is a fast-acting NN compound that has the potential to be found in water sources and more pedestrian (vs. agricultural) applications.²⁻⁴ For example, veterinarians administer nitenpyram as an oral treatment (Capstar®) for immediate treatment of pets for flea and tick infestations prior to prescribing more long-term solutions with imidacloprid-based treatments. As such, nitenpyram is a popular target in the literature for sensing schemes.^{18, 60, 61} For this study, nitenpyram represents an interesting target because DFT calculations (**Table 1**) show only *two* viable XB-acceptor sites at the nitro (NO₂) and N¹ groups within the chloropyridine ring, the former being one of the most negative ΔE_{int} values recorded in **Table 1**. It was of interest to test nitenpyram to see if the number of XB-acceptor sites (>2) was required to achieve detection and/or if it provides some contextual selectivity to the method.

Figure 4 captures the results of *f*-MPCs engaging in XB with nitenpyram and clearly shows that the system detects the nitenpyram in a similar fashion to imidacloprid. In brief, when nitenpyram was added to an *f*-MPC solution in toluene, the early UV-vis spectra (e.g., 2 minutes) (**Fig. 4A**) reflected the spectroscopic signature of both *f*-MPCs and nitenpyram including the expected and prominent SPR band at 518 nm of the MPC material (**Fig. 2**). After mixing, over time, the same notable red shift in the SPR band and a significant decrease in absorbance due to XB-induced aggregation of the *f*-MPCs were observed. As with the imidacloprid system, aggregation could be visually confirmed as aggregates “crashed out” of solution (**Fig. 4C, left**), a phenomenon that was observed in the corresponding TEM image (**Fig. 4C, right**).

As in other NP aggregation-based molecular detection schemes, control experiments are key to demonstrating the observed phenomenon is due to XB interactions. As will be shown, these control experiments produced significantly different spectral trends. In the case of imidacloprid,

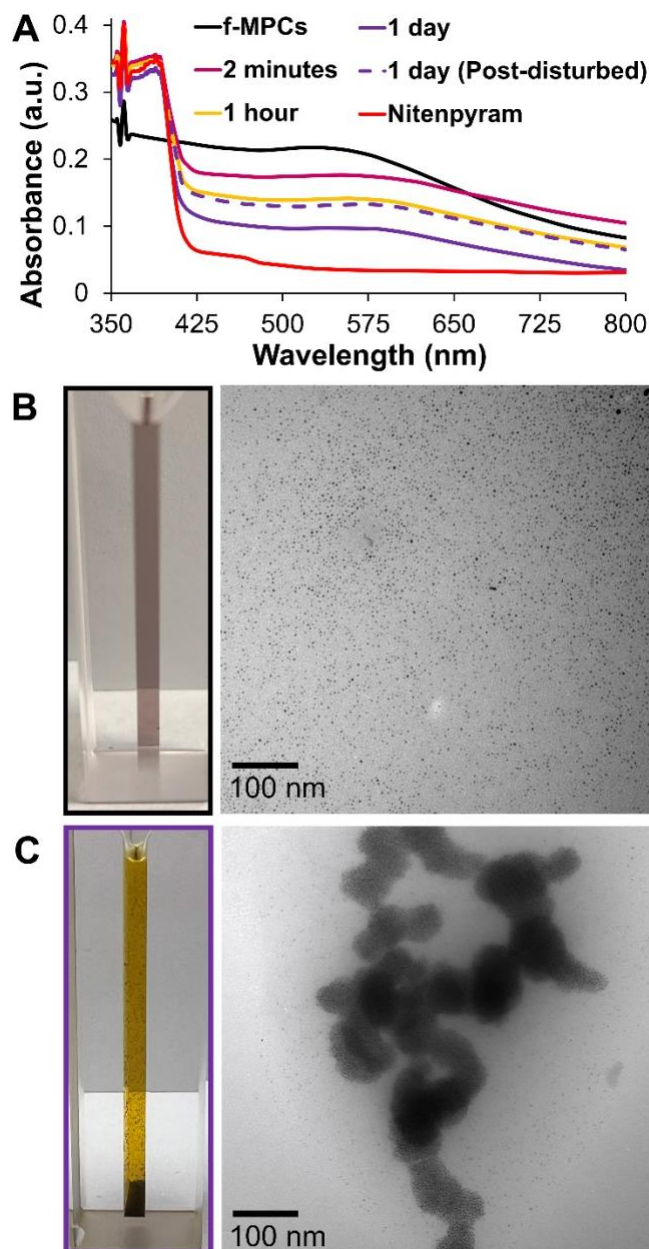


Figure 4. (A) UV-Vis spectra of *f*-MPCs in toluene upon exposure to nitenpyram (11 mM) over time. (B, C) TEM images (right) with visual pictures (left) of *f*-MPCs (B) before and (C) 1 day after the addition of nitenpyram (11 mM). The dashed UV-Vis spectrum in (A) was taken briefly after the temporary resuspension of precipitated *f*-MPC aggregates at the bottom of the cuvette (after 1 day).

it was mixed with *unf*-MPCs (not place-exchanged with the XB-donor ligands) that lacked the –C₆F₄I moieties to engage in XB interactions. As shown in **Figure 5A**, mixing *unf*-MPCs with imidacloprid did not result in the same UV-Vis spectral behaviors expected for NP aggregation events even after days of exposure. This result suggests aggregation of *f*-MPCs was indeed due to

decreased interparticle spacing induced by significant XB interactions. Similar experiments mixing *unf*-MPCs with nitenpyram also showed no spectral shifts or diminished SPR signal (**Figure 5B**) on the scale observed with the *f*-MPCs–nitenpyram mixture, again supporting that the observed aggregation events were XB-induced (**Figs. 3** and **4**). The *f*-MPCs–nitenpyram aggregation event was also successfully repeated using THF as the solvent (Supporting Information, Figure S31), an important result given that our prior work established that solvent can significantly affect the strength of XB interactions.³⁸ Solvent effects are discussed more in the Conclusions section.

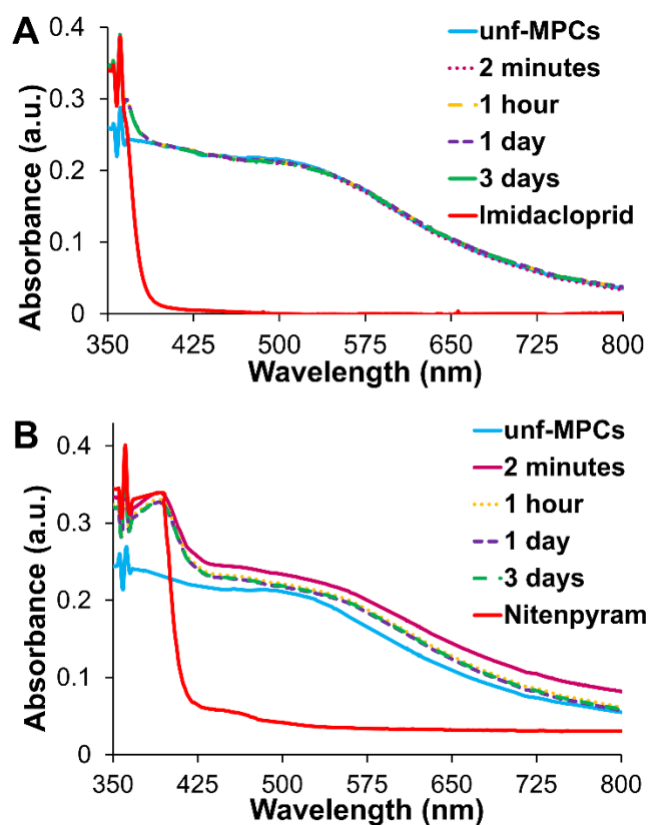


Figure 5. UV-Vis spectra of control experiments of exposing *unf*-MPCs to either (A) imidacloprid (50 mM) or (B) nitenpyram (11 mM) over time.

In terms of using *f*-MPCs for the quick detection of imidacloprid or nitenpyram, it is important to examine the UV-Vis spectral response of the systems in the first few minutes versus hours after initial mixing. **Figure 6** summarizes the UV-Vis spectral responses in the early timeframe (1 hour) for both *f*-MPCs and *unf*-MPCs exposed to imidacloprid and nitenpyram. As a quick detection system, the UV-Vis spectra of *f*-MPCs in the presence of either NN compound

exhibited a notable decrease of ~35% in the first 20 minutes compared to only 1–2% decreases seen with corresponding *unf*-MPCs in the same timeframe. Longer timeframes (days) showed that the decrease in absorbance of the *f*-MPCs–imidacloprid mixture was more pronounced and ongoing than the *f*-MPCs–nitenpyram mixture after the first hour. In comparison, mixtures of *unf*-MPCs (incapable of XB interactions) with either nitenpyram or imidacloprid yielded stable UV-Vis spectra for days. The longer timeframe results are provided in the Supporting Information

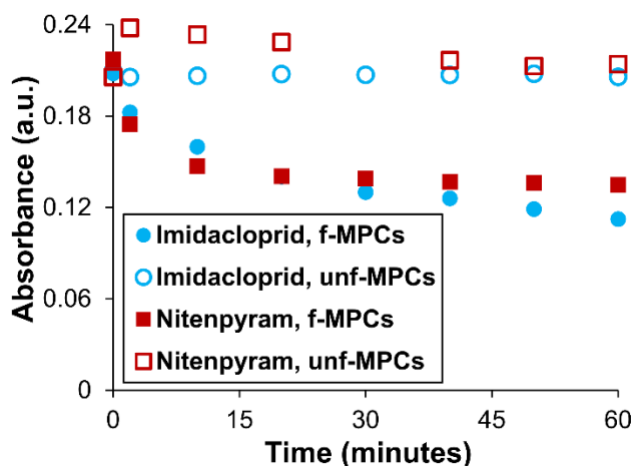


Figure 6. Spectral tracking of $Abs_{@518nm}$ as a function of time of the mixtures of either *f*-MPCs or *unf*-MPCs exposed to either imidacloprid or nitenpyram (shorter time-scale analysis).

(Figure S29). It is notable that the behaviors of these mixtures (i.e., red-shifting SPR band and decreasing absorbance due to XB-induced aggregation of *f*-MPCs vs. comparatively negligible UV-Vis spectral changes seen with *unf*-MPCs) are entirely consistent with the previously reported XB-induced aggregation event of the same *f*-MPCs mixed with a model, two-binding-site XB-acceptor molecule, DABCO.⁴⁰ This DABCO result was reproduced for the current study and shown in Supporting Information (Figure S30) as a positive control test for the functionality of the *f*-MPCs. Taken collectively, these results suggest that the systematic decrease in the SPR band of *f*-MPCs in the presence of these two NN compounds are directly attributable to XB-induced agglomeration and subsequent aggregation of these XB adducts, while no notable shifts or changes in the UV-Vis spectra are observed with *unf*-MPCs in the presence of those same compounds.

¹H DOSY NMR was used to measure diffusion coefficients for nitenpyram, imidacloprid, and thiacloprid, each of which is representative of each major category of NN compound (**Scheme 1**), and solvent molecules (controls) in the presence of either *f*-MPCs or *unf*-MPCs. The results of

these experiments are shown in **Table 3**; it is again useful to refer to the **experiment number (#)** in the first column in discussing the results. Essentially, the hypothesis of these experiments is that if there are significant XB interactions between *f*-MPCs and a NN compound, the latter will diffuse more slowly because of its strong, specific binding to the bulky *f*-MPCs. This effect should be absent with *unf*-MPCs, which cannot engage in XB interactions. This comparison, a NN with either *f*-MPCs or *unf*-MPCs, is shown in **Table 3** for nitenpyram (**experiments #1–2**), imidacloprid (**experiments #5–6**), and thiacloprid (**experiments #9–10**). Each NN compound exhibited a more negative log D value when mixed with *f*-MPCs than with *unf*-MPCs. While this supports the hypothesis, it is notable that nitenpyram and imidacloprid showed significantly more negative log D values with *f*-MPCs vs. *unf*-MPCs than thiacloprid. These results agree with our aggregation experiments in which *f*-MPCs aggregated and “crashed out” of solution in the presence of imidacloprid (Fig. 3) or nitenpyram (Fig. 4). Similar observations were absent in the mixtures of *f*-MPCs with thiacloprid or thiamethoxam (Supporting Information, Figures S32 and S33). UV-Vis spectra of the *f*-MPCs exposed to thiacloprid or thiamethoxam gradually decreased over three days but never resulted in visible *f*-MPC aggregation. This “selectivity” for imidacloprid and nitenpyram, believed to be related to NN solubility, is further discussed in the Conclusions section. Also notable from **Table 3** are the log D values of solvent molecules (control experiments) in the MPCs–NN mixtures, which stay relatively constant across all respective system environments (**experiments #3 vs. #4** for toluene; **experiments #7 vs. #8** and **experiments #11 vs. #12** for THF).

Table 3. Diffusion-Ordered Spectroscopy (DOSY) NMR Measurements of Diffusion Coefficients (D) of Nitenpyram, Imidacloprid, and Thiamethoxam in the Presence of *unf*-MPCs and *f*-MPCs.

#	XB Acceptor	Solvent	XB Donor	Target	Log D (log(m ² /sec))
1	Nitenpyram (11 mM)	Toluene-d ₈	<i>unf</i> -MPCs	¹ H	-8.65 (±0.06)
2			<i>f</i> -MPCs	Nitenpyram	-8.76 (±0.03)
3			<i>unf</i> -MPCs	¹ H	-8.55 (±0.07)
4			<i>f</i> -MPCs	Toluene-d ₇ h ₁	-8.56 (±0.06)
5	Imidacloprid (50 mM)	Tetrahydrofuran-d ₈	<i>unf</i> -MPCs	¹ H	-8.63 (±0.04)
6			<i>f</i> -MPCs	Imidacloprid	-8.73 (±0.04)
7			<i>unf</i> -MPCs	¹ H	-8.48 (±0.03)
8			<i>f</i> -MPCs	Tetrahydrofuran-d ₇ h ₁	-8.48 (±0.05)
9	Thiacloprid (100 mM)	Tetrahydrofuran-d ₈	<i>unf</i> -MPCs	¹ H	-8.61 (±0.06)
10			<i>f</i> -MPCs	Thiacloprid	-8.63 (±0.05)
11			<i>unf</i> -MPCs	¹ H	-8.49 (±0.06)
12			<i>f</i> -MPCs	Tetrahydrofuran-d ₇ h ₁	-8.48 (±0.04)

Notes: Concentrations of *unf*-MPCs and *f*-MPCs are equivalent to A₅₁₈ = 0.50 a.u. DOSY NMR measurements of the sample of each NN with either *unf*-MPCs or *f*-MPCs were carried out at 15 minutes after sample preparation.

¹H toluene-d₇h₁ and ¹H tetrahydrofuran-d₇h₁ refers to the ¹H NMR residual solvent signals of toluene and tetrahydrofuran molecules, respectively, that contain one less deuterium atom than toluene-d₈ and tetrahydrofuran-d₈, respectively.

Given its widespread global use, imidacloprid detection using the *f*-MPCs was also observed using DLS. As shown in **Figure 7**, a solution of *f*-MPCs prior to exposure to imidacloprid had an expected average diameter of ~ 4.5 nm that is consistent with TEM histogram measurements. Upon exposure of *f*-MPCs to imidacloprid, there was nearly immediate evidence of increased NP average diameter due to the *f*-MPCs agglomerating in solution after only 2 minutes. Persistent increases in particle size over time were observed for the *f*-MPCs in the presence of imidacloprid particularly over the first hour. After 24 hours, nearly complete aggregation or visible precipitation of *f*-MPCs was again observed. DLS measurements of the 1-day sample after being physically perturbed via inversions show a significantly broadened peak representing even larger particle average diameter, large aggregates temporarily suspended in solution. An analogous experiment using a solution of *unf*-MPCs show no change in NP average diameter after exposure to imidacloprid over the same time frame (Supporting Information, Figure S35).

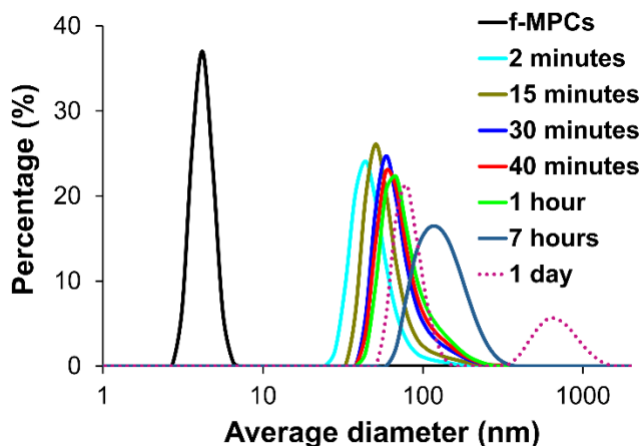


Figure 7. DLS results of *f*-MPCs in THF ($Abs_{518} = 0.20$ a.u.) before and after the addition of imidacloprid (12 mM) as a function of time. A control DLS experiment using *unf*-MPCs is included in Supporting Information (Figure S35) and shows no change in particle average diameter over time.

D. Interferent and Limit of Detection Considerations. With any molecular detection scheme, even one that targets on-site, fast identification of an unknown powder or heavy residue that can be collected, it is important to establish effective selectivity in the

presence of interferent species and sufficient sensitivity in terms of detection limits toward a targeted analyte. In both cases, the much more desirable NN target molecule remains the increasingly used and environmentally dangerous imidacloprid. As such, the *f*-MPC scheme was executed for imidacloprid in the presence of four different interferent groups: (1) other non-aggregating NN pesticides (acetamiprid and clothianidin, **Scheme 1-H** and **1-F**; see Section III–E below); (2) commonly employed organophosphate pesticides (parathion and chlorpyrifos); (3) a commonly used carbamate pesticide (carbaryl);⁶² and (4) a plasticizer commonly found in the environment (dioctyl phthalate). As conducted in other studies of this nature,²³ simple mixtures of these compounds were added to *f*-MPC solutions in the presence and absence of imidacloprid. UV-Vis spectra collected for these experiments show that, in all cases, *f*-MPCs aggregated in the presence of imidacloprid as expected and regardless of the presence of any of the interferents, while analogous control solutions containing only the interferent species with no imidacloprid resulted in no evidence of aggregation on the time-scale of the experiment (24 hours). These results are shown in Supporting Information (Figures S36–S38) and establish that these *f*-MPCs are highly selective for imidacloprid even when other NN compounds, environmental contaminants, or other organophosphate or carbamate pesticides are present in significant amounts (50 mM).

In terms of sensitivity, NP aggregation schemes of this nature have two major considerations when it comes to limit of detection (LOD) evaluation. Like other colorimetric or visual NP aggregation schemes,⁵⁸ it is not unusual to have *both* a visible (no calibration curve) and an instrumental-based LOD, the latter requiring a hand-held device to be developed. Indeed, given that aggregation was observed instrumentally using spectroscopy, DLS, and TEM, it seems that the instrumental LOD detection will be linked to the ability to detect the *f*-MPCs themselves. In this study, spectroscopy was mainly used to correspond to visual aggregation of the *f*-MPCs, which means that the LOD is linked to the *ratio* of soluble NN molecules to *f*-MPCs as well as the available instrumentation capability to observe aggregation. For a visible indication of imidacloprid, we systematically lowered the mass of the NN in the sample holder to determine the minimum concentration of imidacloprid that caused obvious aggregation. Spectroscopically, we based estimated LOD on the minimum concentration of imidacloprid that caused a measurable and repeatable spectral shift and/or decrease. In this manner, as shown in **Figure 8**, aggregation was visible with 1 μ M imidacloprid (or 25 μ g) while spectral shifts suggested a 3 μ M LOD for

imidacloprid (Supporting Information, Figure S39). In either case, it is important to note that visual observation of aggregation will depend on the size/shape of the sample holder to see NP precipitation while development of a dedicated, hand-held spectroscopic instrument with a smaller volume chamber for sample would likely achieve a lower LOD.

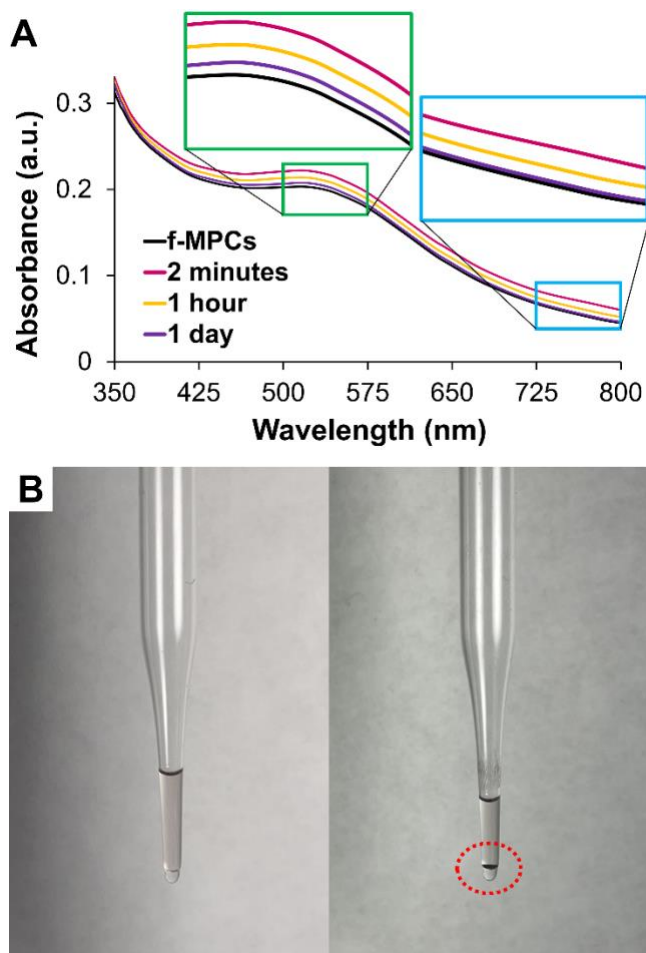


Figure 8. (A) UV-Vis spectra of *f*-MPCs in THF exposed to 1 μ M imidacloprid over time. (B) Visual images of 10 μ L of *f*-MPC solution in THF in a sealed Pasteur pipette before (left) and 1 hour after (right) the addition of 25 μ g of imidacloprid. Note: Similar analysis of nitenpyram resulted in a minimal mass of 11 μ g and a LOD of 1 μ M (Supporting Information, Figure S40).

E. Less Prominent Neonicotinoid Compound Testing. Even though not used as extensively as imidacloprid in NN applications, XB-induced aggregation of *f*-MPCs was also investigated for other N-nitroguanidine-based NNs with similar structures to imidacloprid's

including clothianidin, thiamethoxam, and dinotefuran (**Scheme 1–H, J, and L**, respectively). Interestingly, for thiamethoxam, red-shifts of *f*-MPCs' SPR band and decreasing absorbance in UV-Vis spectra were again observed, though eventual aggregation was not visible on the same timescale (Supporting Information, Figure S33). It is speculated that this is related to the solubility limits of thiamethoxam in that there was not enough amount of the NN compound solubilized to interact with a significant number of *f*-MPCs, a concept discussed further in the Conclusions section. UV-Vis spectra of *f*-MPCs in the presence of clothianidin and dinotefuran did not diminish over time (Supporting Information, Figures S33 and S34), an example of systems that likely did not engage in significant XB interactions. Another N-nitroguanidine classified NN compound called imidaclothiz (**Scheme 1–K**) was not tested experimentally due to a lack of commercial availability.

Cyano-based NN compounds sulfoxaflor, acetamiprid, and thiacloprid (**Scheme 1–D, F, and G**, respectively) were tested with *f*-MPCs while flonicamid (**Scheme 1–E**) was not tested for XB-induced aggregation. Spectroscopic tracking of the UV-Vis spectra of *f*-MPCs exposed to sulfoxaflor, acetamiprid, and thiacloprid showed very little spectral shift or decrease over time, suggesting the absence of XB-induced aggregation (Supporting Information, Figures S31–S32). These systems were again severely limited by the solubility of the compounds in the solvent (THF). However, it is also reasonable to assess from the collective experimental and computational results that the cyano groups in this subclass of NN compounds may simply represent weaker XB acceptors (vs. nitro groups) that are unable to engage in strong enough XB interactions for a measurable response.⁶³ That said, the stability of *f*-MPCs observed with clothianidin and dinotefuran, nitro-containing NN compounds, suggests that solubility may play the most critical role (see the Conclusions section). Cycloxaprid and nithiazine, the remaining nitro-based NN compounds (**Scheme 1–B and C**, respectively) were not tested in this study due to insolubility in toluene and THF (tested solvents) and commercial unavailability, respectively. As such, from the significant number of NNs tested, the specific *f*-MPC aggregation-based detection scheme in this study appears to be self-selective for signaling the presence of two critical NN compounds: imidacloprid, one of the most widely used NNs globally, and nitenpyram.

F. Imidacloprid Sensors. Even though the focus of our study was the functionalized NPs and their XB-induced aggregation, we recognize that these materials could serve as a

functional component of a sensing system. As with the development of any sensing scheme, it is important to contextualize the potential analytical performance in the broader field where there have been several developed sensors targeting imidacloprid.⁶⁴⁻⁶⁹ A study in 2022 employed the fluorescence signal of a Zr metal-organic structure and its aggregation to detect imidacloprid and thiamethoxam with excellent LODs, including in real samples of fruit juice analyzed in a laboratory environment. Additionally, the report tested selectivity of the sensor against only three other NN compounds.⁶⁶ An electrochemical sensor, reported in 2022 by Harraz et al., featuring an electrode modified with a composite film of Ag-NPs in a carbon/hematite ore, performed in a similar capacity to this study in terms of sensitivity, yielding detection in the μM range with a LOD of $\sim 1 \mu\text{M}$. As with most modified electrodes, it is susceptible to fouling, particularly in environmental testing and, in this study, was tested against an interferent array not including other pesticides.⁶⁷ A very encouraging trend in the literature on imidacloprid sensors is the number of colorimetric/spectroscopic studies utilizing the same techniques used in our study (i.e., UV-Vis spectroscopy and TEM imaging),^{64, 65, 68-70} including some reports employing different Au-NPs and observing similar magnitude spectral shifts.^{64, 68, 69} Moghaddam and coworkers demonstrated colorimetric sensing of imidacloprid using graphene-Au quantum dots (QDs) that visibly changed color, though sometimes visibly indistinguishable between certain concentrations, or exhibited spectroscopy attenuation of the SPR in the presence of only ppm pesticide—the latter technique was required for imidacloprid quantitative analysis. The QDs, which interacted with imidacloprid's imidazole group, are non-trivial to synthesize and were demonstrated to detect the pesticide on vegetables requiring significant preparation after simulated treatments that may or may not expectation in the environment. Targeting the imidazole group has the disadvantage in that imidacloprid is not the only NN compound with that functionality.⁷⁰ A study by Feng et al. this year (2023) used colorimetry/spectroscopy with a Prussian blue polymer NPs for imidacloprid detection. However, their selectivity testing did not include other NN compounds and focused on other types of pesticides, some of which yielded the same colorimetric response as imidacloprid (parathion and fenthion). Interestingly, these authors observed that a contributing factor to their observed selectivity was the polarity of their solvent⁶⁵—a similar conclusion to our study as discussed below. Other researchers who employed Au-NPs to detect imidacloprid used visible spectroscopy to monitor water-soluble Au-NPs (i.e., citrate-based Au-NPs), reporting small SPR spectral shifts, like our study, with exposure to increasing imidacloprid concentrations as well as

similar LODs (0.5-1.0 μM).^{68, 69} These type of aqueous NPs, some requiring intensive synthesis for this application, are notorious for poor long-term stability, with one report indicating that the NPs only lasted 15 days.⁶⁸ Another recent study by Zhao and coworkers employed thiol-protected Au-NPs which are more stable, but their methodology required the use of an automated shaker and colorimetric imager.⁶⁴ In all the Au-NP studies mentioned, however, imidacloprid selectivity was established in the presence of other non-neonicotinoid pesticides and only a limited number of competing neonicotinoid compounds. Assessed collectively, we can surmise a number of advantages of our proposed NN detection scheme using our *f*-MPCs compared to other systems in the literature including: (1) high selectivity for imidacloprid against an array of other NN pesticides (the only exception being nitenpyram); (2) the use of highly-stable Au-NPs where the *f*-MPCs remained selective for imidacloprid for a year or more; (3) the aggregation is a visible, non-instrument indication of the presence of the NN compound, even if interferents are present in significant amounts. In addition to these advantages, the *f*-MPC scheme presented appears to have response times and LODs of similar magnitude to the aforementioned sensor literature, suggesting the functionality of these materials is promising if developed into an instrumental, hand-held sensor.

IV. Conclusions

The goals of this research project were two-fold: (1) achieving a greater fundamental understanding of XB interactions between strong XB-donor moieties and different types of NN compounds; and (2) the synthesis of XB-donor functionalized MPCs (*f*-MPCs) that serve as the functional component of uniquely functionalized NMs capable of aggregation-based detection of one of the most widely used NN pesticides globally, imidacloprid—a platform that can serve as the basis for a developing detection tools that do not require instrumentation or trained personnel. The observed aggregation events of *f*-MPCs featuring strong XB-donor ligands, which are selective for only imidacloprid and nitenpyram, establish the viability of using these NMs for such an application. While the *f*-MPC system in this study is self-selective for imidacloprid and nitenpyram, the results suggest that these systems may have more applications and offer parameters that can be tuned for selectivity to other compounds of interest. Like other NP

aggregation schemes,³⁴ we strongly suspect that our system can be adjusted to be applied for other NN compounds, albeit with important limitations. A critical component of this methodology, established here and in other studies, is the role of solvent in XB-based systems where certain solvents can “shield”/weaken the XB interactions.^{38, 40, 71} Absent that shielding effect of the solvent, our demonstrated experimental system is effective because *both* the specific diameter *f*-MPCs *and* the targeted NNs are soluble in a solvent that promotes strong XB interactions. For example, while imidacloprid, nitenpyram, and *f*-MPCs were soluble in THF, we suspect that sulfoxaflor, acetamiprid, thiacloprid, clothianidin, thiamethoxam, and dinotefuran are not soluble in THF to the same degree and thus self-limiting in detection by this method. Given our understanding and ability to manipulate the solubility of *f*-MPCs (e.g., altering gold core sizes, peripheral ligand properties/functional groups, and degrees of XB-donor ligand functionalization), it is conceivable that specific *f*-MPC systems could be designed for other NN compounds—studies that are currently underway in our laboratory. The current work represents a fundamental proof-of-concept application of XB-capable *f*-MPCs for fast, on-site identification of imidacloprid and nitenpyram. One can envision dipping a cotton swab sampling of an unknown powder found at a pesticide manufacturer or storage area into *f*-MPC solution exhibiting XB-induced NP aggregation and thus yielding a preliminary indication of the presence of imidacloprid, an increasingly regulated or prohibited pesticide in many parts of the world.

Supporting Information

Experimental details of DFT calculations and DOSY NMR measurements; DFT geometry-optimized XB adducts of IPFB with all neonicotinoid compounds; DOSY NMR measurements of thiamethoxam in the presence of IPFB, PFT, *f*-MPCs, and *unf*-MPCs, ¹H NMR spectra of DOSY-tested neonicotinoid compounds; UV-Vis spectra of neonicotinoid compounds; UV-Vis spectra and/or TEM images of aggregation events of *f*-MPCs with nitenpyram (in THF), imidacloprid (after 2 minutes), and DABCO (positive control); UV-Vis spectral tracking over long periods for *f*-MPCs and *unf*-MPCs (control) exposed to imidacloprid, nitenpyram, and DABCO; UV-Vis spectra of *f*-MPCs in the presence of less prominent NN compounds; DLS results of *unf*-MPCs with imidacloprid; Interferent testing with other NN compounds; Imidacloprid calibration curve; UV-Vis spectra and visual imaging of *f*-MPCs with nitenpyram.

References

1. Blacquiere, T.; Smaghe, G.; van Gestel, C. A. M.; Mommaerts, V., Neonicotinoids in bees: a review on concentrations, side-effects and risk assessment. *Ecotoxicology* **2012**, *21* (4), 973-992.
2. Pisa, L.; Goulson, D.; Yang, E.-C.; Gibbons, D.; Sánchez-Bayo, F.; Mitchell, E.; Aebi, A.; Van Der Sluijs, J.; Macquarrie, C. J. K.; Giorio, C.; Long, E. Y.; McField, M.; Bijleveld Van Lexmond, M.; Bonmatin, J.-M., An update of the Worldwide Integrated Assessment (WIA) on systemic insecticides. Part 2: impacts on organisms and ecosystems. *Environ Sci Pollut R* **2021**, *28* (10), 11749-11797.
3. Giorio, C.; Safer, A.; Sánchez-Bayo, F.; Tapparo, A.; Lentola, A.; Girolami, V.; Van Lexmond, M. B.; Bonmatin, J.-M., An update of the Worldwide Integrated Assessment (WIA) on systemic insecticides. Part 1: new molecules, metabolism, fate, and transport. *Environ Sci Pollut R* **2021**, *28* (10), 11716-11748.
4. Thompson, D. A.; Lehmler, H. J.; Kolpin, D. W.; Hladik, M. L.; Vargo, J. D.; Schilling, K. E.; LeFevre, G. H.; Peeples, T. L.; Poch, M. C.; LaDuca, L. E.; Cwiertny, D. M.; Field, R. W., A critical review on the potential impacts of neonicotinoid insecticide use: current knowledge of environmental fate, toxicity, and implications for human health. *Environ Sci-Proc Imp* **2020**, *22* (6), 1315-1346.
5. Elbert, A.; Haas, M.; Springer, B.; Thielert, W.; Nauen, R., Applied aspects of neonicotinoid uses in crop protection. *Pest Manag Sci* **2008**, *64* (11), 1099-1105.
6. Oliveira, A. E. F.; Bettio, G. B.; Pereira, A. C., An Electrochemical Sensor Based on Electropolymerization of ss-Cyclodextrin and Reduced Graphene Oxide on a Glassy Carbon Electrode for Determination of Neonicotinoids. *Electroanal* **2018**, *30* (9), 1918-1928.
7. Lundin, O.; Rundlöf, M.; Smith, H. G.; Fries, I.; Bommarco, R., Neonicotinoid Insecticides and Their Impacts on Bees: A Systematic Review of Research Approaches and Identification of Knowledge Gaps. *PLoS One* **2015**, *10* (8), e0136928.
8. Henry, M.; Béguin, M.; Requier, F.; Rollin, O.; Odoux, J.-F.; Aupinel, P.; Aptel, J.; Tchamitchian, S.; Decourtye, A., A Common Pesticide Decreases Foraging Success and Survival in Honey Bees. *Science* **2012**, *336* (6079), 348-350.
9. Straub, L.; Villamar-Bouza, L.; Bruckner, S.; Chantawannakul, P.; Kolari, E.; Maitip, J.; Vidondo, B.; Neumann, P.; Williams, G. R., Negative effects of neonicotinoids on male honeybee survival, behaviour and physiology in the field. *J Appl Ecol* **2021**, *58* (11), 2515-2528.
10. Hopwood, J. C., A.; Vaughan, M.; Biddinger, D.; Shepard, M.; Black, S.H.; Lee-Mader, E.; Mazzacano, C. *How Neonicotinoids Can Kill Bees - The Science Behind the Role These Insecticides Play in Harming Bees*; www.xerces.org, 2016, 2016; p 76.
11. Tasman, K.; Hidalgo, S.; Zhu, B. F.; Rands, S. A.; Hodge, J. J. L., Neonicotinoids disrupt memory, circadian behaviour and sleep. *Sci Rep-Uk* **2021**, *11* (1).
12. Singla, A.; Barmota, H.; Sahoo, S. K.; Kang, B. K., Influence of neonicotinoids on pollinators: A review. *J Apicult Res* **2021**, *60* (1), 19-32.
13. Matsuda, K.; Ihara, M.; Sattelle, D. B., Neonicotinoid Insecticides: Molecular Targets, Resistance, and Toxicity. *Annu Rev Pharmacol* **2020**, *60*, 241-255.
14. Laubscher, B.; Diezi, M.; Renella, R.; Mitchell, E. A. D.; Aebi, A.; Mulot, M.; Glauser, G., Multiple neonicotinoids in children's cerebro-spinal fluid, plasma, and urine. *Environ Health-Glob* **2022**, *21* (1).
15. Johnson, Z. T.; Williams, K.; Chen, B.; Sheets, R.; Jared, N.; Li, J.; Smith, E. A.; Claussen, J. C., Electrochemical Sensing of Neonicotinoids Using Laser-Induced Graphene. *Acs Sensors* **2021**, *6* (8), 3063-3071.
16. Erickson, B., Neonicotinoids are likely to harm endangered species. *Chem Eng News* **2021**, *99* (32), 17-17.
17. Erickson, B., California cracks down on neonicotinoids. *Chem Eng News* **2022**, *100* (9), 20-20.
18. Muhammad, N.; Zhang, Y.; Li, W. X.; Zhao, Y. G.; Ali, A.; Subhani, Q.; Mahmud, T.; Liu, J. W.; Cui, H. R.; Zhu, Y., Determination of nitenpyram and 6-chloronicotinic acid in environmental samples

by ion chromatography coupled with online photochemically induced fluorescence detector. *J Sep Sci* **2018**, *41* (22).

19. Wang, D.; Liu, Y. C.; Xu, Z. G.; Ji, Y.; Si, X. X.; Lin, T.; Liu, H. C.; Liu, Z. M., Generic imprinted fiber array strategy for high-throughput and ultrasensitive simultaneous determination of multiple neonicotinoids. *Food Chem* **2022**, *382*.

20. Iancu, V. I.; Galaon, T.; Niculescu, M.; Lehr, C. B., Neonicotinoids Detection by new LC-MS/MS Method in Romanian Surface Waters. *Rev Chim-Bucharest* **2017**, *68* (8), 1716-1722.

21. Martinez-Perez-Cejuela, H.; Pravcova, K.; Ceslova, L.; Simo-Alfonso, E. F.; Herrero-Martinez, J. M., Zeolitic imidazolate framework-8 decorated with gold nanoparticles for solid-phase extraction of neonicotinoids in agricultural samples. *Microchim Acta* **2021**, *188* (6).

22. Zhang, W.; Luo, Y.; Liu, C.; Yang, M.-X.; Gou, J.-X.; Huang, Y.; Ni, X.-L.; Tao, Z.; Xiao, X., Supramolecular Room Temperature Phosphorescent Materials Based on Cucurbit[8]uril for Dual Detection of Dodine. *Acs Appl Mater Inter* **2022**, *14* (45), 51429-51437.

23. Wu, H.; Zhao, J.; Yang, X. N.; Yang, D.; Chen, L. X.; Redshaw, C.; Yang, L. G.; Tao, Z.; Xiao, X., A cucurbit[8]uril-based probe for the detection of the pesticide tricyclazole. *Dyes and Pigments* **2022**, *199*, 110076.

24. Urbanova, V.; Bakandritsos, A.; Jakubec, P.; Szambo, T.; Zboril, R., A facile graphene oxide based sensor for electrochemical detection of neonicotinoids. *Biosens Bioelectron* **2017**, *89*, 532-537.

25. Qiu, J. L.; Ouyang, G. F.; Pawliszyn, J.; Schlenk, D.; Gan, J., A Novel Water-Swelling Sampling Probe for in Vivo Detection of Neonicotinoids in Plants. *Environmental Science & Technology* **2019**, *53* (16), 9686-9694.

26. Girard, J., *Criminalistics : forensic science, crime, and terrorism*. Fourth edition. ed.; Jones & Bartlett Learning: Burlington, MA, 2018; p xix, 497 pages.

27. Bell, S., *Forensic chemistry*. 2nd ed.; Pearson: Boston, 2013; p xi, 632 p., 2 p. of plates.

28. Senesac, L.; Thundat, T. G., Nanosensors for trace explosive detection. *Mater Today* **2008**, *11* (3), 28-36.

29. Chen, Y. F.; Chen, Z.; He, Y. J.; Lin, H. L.; Sheng, P. T.; Liu, C. B.; Luo, S. L.; Cai, Q. Y., L-cysteine-capped CdTe QD-based sensor for simple and selective detection of trinitrotoluene. *Nanotechnology* **2010**, *21* (12).

30. Ai, K.; Liu, Y.; Lu, L., Hydrogen-Bonding Recognition-Induced Color Change of Gold Nanoparticles for Visual Detection of Melamine in Raw Milk and Infant Formula. *Journal of the American Chemical Society* **2009**, *131* (27), 9496-9497.

31. Dasary, S. S. R.; Senapati, D.; Singh, A. K.; Anjaneyulu, Y.; Yu, H. T.; Ray, P. C., Highly Sensitive and Selective Dynamic Light-Scattering Assay for TNT Detection Using p-ATP Attached Gold Nanoparticle. *Acs Appl Mater Inter* **2010**, *2* (12), 3455-3460.

32. Lin, D. Y.; Liu, H. L.; Qian, K.; Zhou, X.; Yang, L. B.; Liu, J. H., Ultrasensitive optical detection of trinitrotoluene by ethylenediamine-capped gold nanoparticles. *Anal Chim Acta* **2012**, *744*, 92-98.

33. Barfidokht, A.; Mishra, R. K.; Seenivasan, R.; Liu, S.; Hubble, L. J.; Wang, J.; Hall, D. A., Wearable electrochemical glove-based sensor for rapid and on-site detection of fentanyl. *Sensors and Actuators B: Chemical* **2019**, *296*, 126422.

34. Gracie, J.; Zamberlan, F.; Andrews, I. B.; Smith, B. O.; Peveler, W. J., Growth of Plasmonic Nanoparticles for Aging Cask-Matured Whisky. *ACS Applied Nano Materials* **2022**, *5* (10), 15362-15368.

35. Politzer, P.; Murray, J. S.; Clark, T., Halogen bonding: an electrostatically-driven highly directional noncovalent interaction. *Phys Chem Chem Phys* **2010**, *12* (28), 7748-7757.

36. Clark, T.; Hennemann, M.; Murray, J. S.; Politzer, P., Halogen bonding: the sigma-hole. *J Mol Model* **2007**, *13* (2), 291-296.

37. Cavallo, G.; Metrangolo, P.; Milani, R.; Pilati, T.; Priimagi, A.; Resnati, G.; Terraneo, G., The Halogen Bond. *Chem Rev* **2016**, *116* (4), 2478-2601.

38. Dang, Q. M.; Simpson, J. H.; Parish, C. A.; Leopold, M. C., Evaluating Halogen-Bond Strength as a Function of Molecular Structure Using Nuclear Magnetic Resonance Spectroscopy and Computational Analysis. *J Phys Chem A* **2021**, *125* (42), 9377-9393.

39. Sardar, R.; Funston, A. M.; Mulvaney, P.; Murray, R. W., Gold Nanoparticles: Past, Present, and Future. *Langmuir* **2009**, *25* (24), 13840-13851.
40. Dang, Q. M.; Gilmore, S. T.; Lalwani, K.; Conk, R. J.; Simpson, J. H.; Leopold, M. C., Monolayer-Protected Gold Nanoparticles Functionalized with Halogen Bonding Capability—An Avenue for Molecular Detection Schemes. *Langmuir* **2022**, *38* (15), 4747-4762.
41. Duan, H.; Zhang, W.; Zhao, J.; Liang, D.; Yang, X.; Jin, S., A novel halogen bond and a better-known hydrogen bond cooperation of neonicotinoid and insect nicotinic acetylcholine receptor recognition. *J Mol Model* **2012**, *18* (8), 3867-3875.
42. Frisch, M. J.; Trucks, G. W.; Schlegel, H. B.; Scuseria, G. E.; Robb, M. A.; Cheeseman, J. R.; Scalmani, G.; Barone, V.; Petersson, G. A.; Nakatsuji, H. *Gaussian 16*, Gaussian Inc.: Wallington, CT, 2016.
43. Zhao, Y.; Truhlar, D. G., The M06 suite of density functionals for main group thermochemistry, thermochemical kinetics, noncovalent interactions, excited states, and transition elements: two new functionals and systematic testing of four M06-class functionals and 12 other functionals. *Theor Chem Acc* **2008**, *120* (1-3), 215-241.
44. Dunning, T. H., Gaussian-Basis Sets for Use in Correlated Molecular Calculations .1. The Atoms Boron through Neon and Hydrogen. *J Chem Phys* **1989**, *90* (2), 1007-1023.
45. Kendall, R. A.; Jr., T. H. D.; Harrison, R. J., Electron affinities of the first-row atoms revisited. Systematic basis sets and wave functions. *The Journal of Chemical Physics* **1992**, *96* (9), 6796-6806.
46. Parker, A. J.; Stewart, J.; Donald, K. J.; Parish, C. A., Halogen Bonding in DNA Base Pairs. *Journal of the American Chemical Society* **2012**, *134* (11), 5165-5172.
47. Zhu, Z.; Xu, Z.; Zhu, W., Interaction Nature and Computational Methods for Halogen Bonding: A Perspective. *Journal of Chemical Information and Modeling* **2020**, *60* (6), 2683-2696.
48. Brust, M.; Walker, M.; Bethell, D.; Schiffrin, D. J.; Whyman, R. J., Synthesis of thiol-derivatised gold nanoparticles in a two-phase Liquid–Liquid system. *J. Chem. Soc.- Chem. Commun.* **1994**, 801.
49. Hostetler, M. J.; Wingate, J. E.; Zhong, C. J.; Harris, J. E.; Vachet, R. W.; Clark, M. R.; Londono, J. D.; Green, S. J.; Stokes, J. J.; Wignall, G. D.; Glish, G. L.; Porter, M. D.; Evans, N. D.; Murray, R. W., Alkanethiolate Gold Cluster Molecules with Core Diameters from 1.5 to 5.2 nm: Core and Monolayer Properties as a Function of Core Size. *Langmuir* **1998**, *14* (1), 17-30.
50. Hostetler, M. J.; Templeton, A. C.; Murray, R. W., Dynamics of place-exchange reactions on monolayer-protected gold cluster molecules. *Langmuir* **1999**, *15* (11), 3782-3789.
51. Sakthivel, N. A.; Jupally, V. R.; Eswaramoorthy, S. K.; Wijesinghe, K. H.; Nimmala, P. R.; Kumara, C.; Rambukwella, M.; Jones, T.; Dass, A., Size Exclusion Chromatography: An Indispensable Tool for the Isolation of Monodisperse Gold Nanomolecules. *Anal Chem* **2021**, *93* (8), 3987-3996.
52. Liu, X.; Atwater, M.; Wang, J.; Huo, Q., Extinction coefficient of gold nanoparticles with different sizes and different capping ligands. *Colloids and Surfaces B: Biointerfaces* **2007**, *58* (1), 3-7.
53. Li, Q. Z.; Jing, B.; Li, R.; Liu, Z. B.; Li, W. Z.; Luan, F.; Cheng, J. B.; Gong, B. A.; Sun, J. Z., Some measures for making halogen bonds stronger than hydrogen bonds in H₂CS-HOX (X = F, Cl, and Br) complexes. *Phys Chem Chem Phys* **2011**, *13* (6), 2266-2271.
54. Myers, J. P.; Antoniou, M. N.; Blumberg, B.; Carroll, L.; Colborn, T.; Everett, L. G.; Hansen, M.; Landrigan, P. J.; Lanphear, B. P.; Mesnage, R.; Vandenberg, L. N.; vom Saal, F. S.; Welshons, W. V.; Benbrook, C. M., Concerns over use of glyphosate-based herbicides and risks associated with exposures: a consensus statement. *Environ Health-Glob* **2016**, *15*.
55. Benbrook, C. M., Trends in glyphosate herbicide use in the United States and globally. *Environ Sci Eur* **2016**, *28*.
56. Arther, R. G.; Cunningham, J.; Dorn, H.; Everett, R.; Herr, L. G.; Hopkins, T., Efficacy of imidacloprid for removal and control of fleas (*Ctenocephalides felis*) on dogs. *Am J Vet Res* **1997**, *58* (8), 848-50.
57. Whitehorn, P. R.; O'Connor, S.; Wackers, F. L.; Goulson, D., Neonicotinoid Pesticide Reduces Bumble Bee Colony Growth and Queen Production. *Science* **2012**, *336* (6079), 351-352.

58. Vilela, D.; Gonzalez, M. C.; Escarpa, A., Sensing colorimetric approaches based on gold and silver nanoparticles aggregation: Chemical creativity behind the assay. A review. *Anal Chim Acta* **2012**, *751*, 24-43.
59. Jiang, Y.; Zhao, H.; Zhu, N. N.; Lin, Y. Q.; Yu, P.; Mao, L. Q., A Simple Assay for Direct Colorimetric Visualization of Trinitrotoluene at Picomolar Levels Using Gold Nanoparticles. *Angew Chem Int Edit* **2008**, *47* (45), 8601-8604.
60. Zhang, M.; Zhang, H.; Zhai, X. C.; Yang, X.; Zhao, H. T.; Wang, J.; Dong, A. J.; Wang, Z. Y., Application of beta-cyclodextrin-reduced graphene oxide nanosheets for enhanced electrochemical sensing of the nitenpyram residue in real samples. *New J Chem* **2017**, *41* (5), 2169-2177.
61. Li, A. J.; Chu, Q. Q.; Zhou, H. F.; Yang, Z. P.; Liu, B.; Zhang, J. W., Effective nitenpyram detection in a dual-walled nitrogen-rich In(III)/Tb(III)-organic framework. *Inorg Chem Front* **2021**, *8* (9), 2341-2348.
62. Gori, M.; Thakur, A.; Sharma, A.; Flora, S. J. S., Organic-Molecule-Based Fluorescent Chemosensor for Nerve Agents and Organophosphorus Pesticides. *Topics Curr Chem* **2021**, *379* (5).
63. Jaini, A. K. A.; Hughes, L. B.; Kitimet, M. M.; Ulep, K. J.; Leopold, M. C.; Parish, C. A., Halogen Bonding Interactions for Aromatic and Nonaromatic Explosive Detection. *Acs Sensors* **2019**, *4* (2), 389-397.
64. Zhao, T.; Liang, X.; Guo, X.; Yang, X.; Guo, J.; Zhou, X.; Huang, X.; Zhang, W.; Wang, Y.; Liu, Z.; Jiang, Z.; Zhou, H.; Zhou, H., Smartphone-based colorimetric sensor array using gold nanoparticles for rapid distinguishment of multiple pesticides in real samples. *Food Chem* **2023**, *404*, 134768.
65. Wang, F.; Zhang, X.; Zhi, H.; Feng, L., Prussian blue analogues based polymer monolith with amphiphilic interface to construct highly selective and sensitive imidacloprid chemosensor. *Talanta* **2023**, *253*, 123870.
66. Xu, Y.; Pu, Y.; Jiang, H.; Huang, Y.; Shen, C.; Cao, J.; Jiang, W., Highly sensitive fluorescent sensing platform for imidacloprid and thiamethoxam by aggregation-induced emission of the Zr(IV) metal – organic framework. *Food Chem* **2022**, *375*, 131879.
67. Rashed, M. A.; Faisal, M.; Alsareii, S. A.; Alsaiari, M.; Jalalah, M.; Harraz, F. A., Highly sensitive and selective electrochemical sensor for detecting imidacloprid pesticide using novel silver nanoparticles/mesoporous carbon/hematite ore ternary nanocomposite. *Journal of Environmental Chemical Engineering* **2022**, *10* (5), 108364.
68. Tan, S.; Zhao, H.; Tian, D.; Wang, F.; Liu, J.; Li, H., Piperidine–calix [4] arene modified gold nanoparticles: Imidacloprid colorimetric sensing. *Sensors and Actuators B: Chemical* **2014**, *204*, 522-527.
69. Zhang, X.; Sun, Z.; Cui, Z.; Li, H., Ionic liquid functionalized gold nanoparticles: Synthesis, rapid colorimetric detection of imidacloprid. *Sensors and Actuators B: Chemical* **2014**, *191*, 313-319.
70. Babazadeh, S.; Moghaddam, P. A.; Keshipour, S.; Mollazade, K., Colorimetric sensing of imidacloprid in cucumber fruits using a graphene quantum dot/Au (III) chemosensor. *Sci Rep-Uk* **2020**, *10* (1), 14327.
71. Sarwar, M. G.; Dragisic, B.; Salsberg, L. J.; Gouliaras, C.; Taylor, M. S., Thermodynamics of Halogen Bonding in Solution: Substituent, Structural, and Solvent Effects. *Journal of the American Chemical Society* **2010**, *132* (5), 1646-1653.

Table of Contents:

- Experimental details of **density functional theory (DFT)** calculations and **diffusion ordered spectroscopy (DOSY) NMR** measurements – p. S2
- **Figures S1 to S20:** Geometry-optimized XB adducts of **XB donor iodopentafluorobenzene (IPFB)** with various XB-acceptor binding sites on **neonicotinoid** compounds: **(B) cycloxaprid** (pp. S3–S4), **(C) nithiazine** (p. S5), **(D) sulfoxaflor** (pp. S6–S7), **(E) flonicamid** (pp. S8–S9), **(F) acetamiprid** (pp. S10–S11), **(G) thiacloprid** (p. S12), **(H) clothianidin** (pp. S13–S14), **(I) imidacloprid** (pp. S15–S16), **(J) thiamethoxam** (pp. S17–S18), **(K) imidaclothiz** (pp. S19–S20), and **(L) dinotefuran** (pp. S21–S22).
- **Tables S1 to S2:** DOSY NMR measurements of **(J) thiamethoxam** and **protonated tetrahydrofuran** (control) in the presence of **IPFB** (XB donor), **perfluorotoluene** (non-XB donor), **f-MPCs**, and **unf-MPCs**. – p. S23
- **Figures S21 to S22:** ¹H NMR spectra for tested **neonicotinoid** compounds in tetrahydrofuran-d₈ (unless otherwise stated) including: **(A) nitenpyram** in toluene-d₈ (p. S24), **(G) thiacloprid** (p. S24), **(I) imidacloprid** (p. S25), and **(J) thiamethoxam** (p. S25).
- **Figures S23 to S27:** UV-Vis spectra for tested **neonicotinoid** compounds in tetrahydrofuran (unless otherwise stated) including: **(A) nitenpyram** in toluene and in tetrahydrofuran (p. S26), **(D) sulfoxaflor** (p. S27), **(F) acetamiprid** (p. S27), **(G) thiacloprid** (p. S28), **(H) clothianidin** (p. S28), **(I) imidacloprid** (p. S29), **(J) thiamethoxam** (p. S29), and **(L) dinotefuran** (p. S30).
- **Figure S28:** TEM analysis of aggregation events of **(I) imidacloprid** with **f-MPCs** in tetrahydrofuran after 2 minutes. – p. S31
- **Figure S29:** Spectral tracking of Abs_{@518nm} as a function of time of the mixtures of either **f-MPCs** or **unf-MPCs** exposed to either **(I) imidacloprid**, **(A) nitenpyram**, or **DABCO** (longer time-scale analysis). – p. S32
- **Figures S30:** UV-Vis spectra and TEM analysis of aggregation events of **f-MPCs** with **DABCO** in toluene. – p. S33
- **Figures S31 to S34:** UV-Vis spectra of **f-MPCs** exposed to other **neonicotinoid** compounds in tetrahydrofuran over time including: **(A) nitenpyram** (p. S34), **(D) sulfoxaflor** (p. S34), **(F) acetamiprid** (p. S35), **(G) thiacloprid** (p. S35), **(H) clothianidin** (p. S36), **(J) thiamethoxam** (p. S36), and **(L) dinotefuran** (p. S37).
- **Figure S35:** DLS results of **unf-MPCs** before and after exposure to imidacloprid (12 mM) – p. S38
- **Figures S36 to S38:** Results of interference tests with **other neonicotinoid** compounds (**acetamiprid** and **clothianidin**, p. S39), common **organophosphate** pesticides (**parathion** and **chlorpyrifos**, p. S40), a common **carbamate** pesticide (**carbaryl**, p. S40), and a **plasticizer** (**dioctyl phthalate**, p. S41).
- **References** – p. S42

Density Functional Theory (DFT) Analysis

Gas-phase geometry optimizations and single-point calculations of the XB donors, XB acceptors, and XB adducts were performed using the Gaussian16 software¹ with the M06 functional² and the cc-pVDZ³ (geometry optimization) and cc-pVTZ⁴ (single point) basis sets. For the larger atoms (iodine, bromine, and selenide), the small (28- e^-) Dirac-Fock (MDF) effective-core pseudopotentials and the corresponding basis sets were used.^{5,6} Frequency analyses were conducted to confirm that the geometry-optimized structures corresponded to true minima (i.e., no imaginary frequencies) on the respective potential energy surfaces. The energy of interaction (ΔE_{int}) or binding energy between XB donors and acceptors was used to estimate the thermodynamic favorability and stability of the XB adducts. Specifically, more negative ΔE_{int} values suggest more thermodynamically favorable adducts. Zero-point energy and basis set superposition corrections were not included in the ΔE_{int} calculations based on the assumption that these harmonic corrections would be very similar for each system as the adducts are structurally similar. The XB bond lengths ($X\cdots B$) and XB bond angles ($R-X\cdots B$) of all XB adducts were also obtained as additional indicators of the strength of XB interactions. Specifically, strong XB interactions are typically characterized by bond lengths shorter than the van der Waals distances of the interacting atoms and nearly linear (180°) $R-X-B$ bond angles.⁸⁻¹²

Experimental Details of Diffusion-Ordered NMR Spectroscopy (DOSY) Measurements

DOSY spectra with convection-compensation were collected using thick-walled 5mm NMR tubes. The DOSYcc parameter set in Bruker Topspin v3.2 was used with the following parameter configuration. The relaxation delay was 3 seconds with 90-degree ^1H RF pulses of 12 microseconds and 180-degree ^1H RF pulses of 24 microseconds. 16 scans were collected over 16 gradient increments from 2% to 95% of the gradient strength, using a linear gradient modulation with a d20 of 60 ms. The data set was processed with an f2 dimension of 16k and an f1 dimension of 32. The dosy2d command in Topspin was executed to process the data set. DOSY peaks were measured with a precision of 0.01 log D units and uncertainties were determined based on the width of the first two cross peak contours.

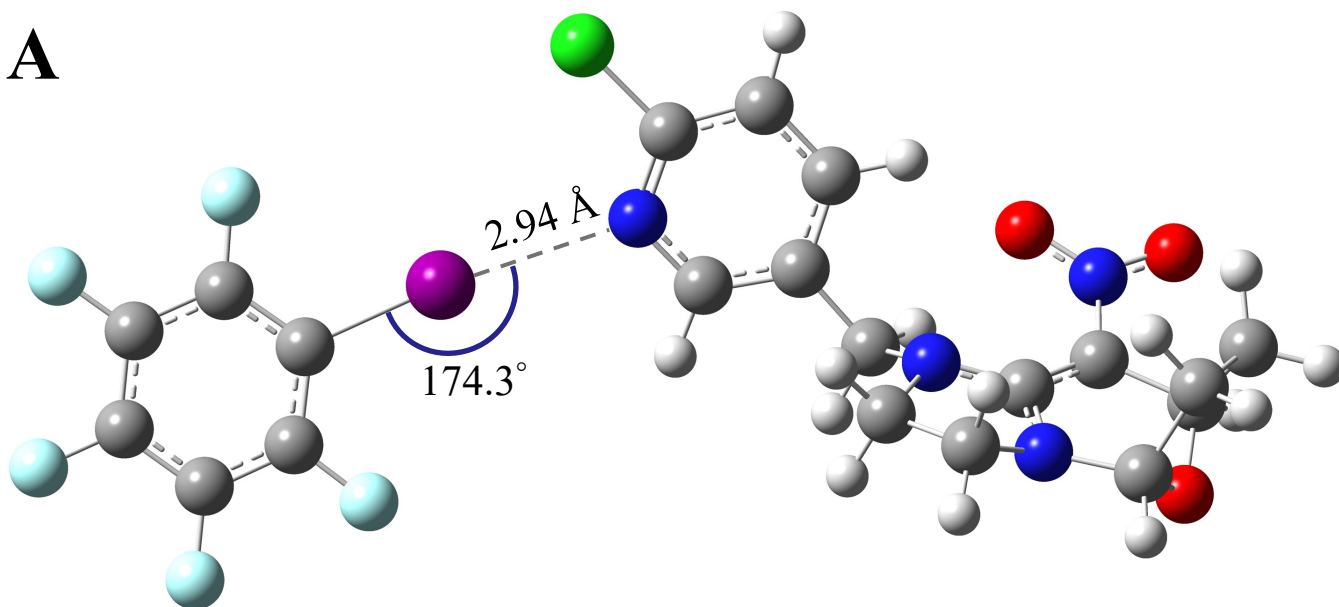
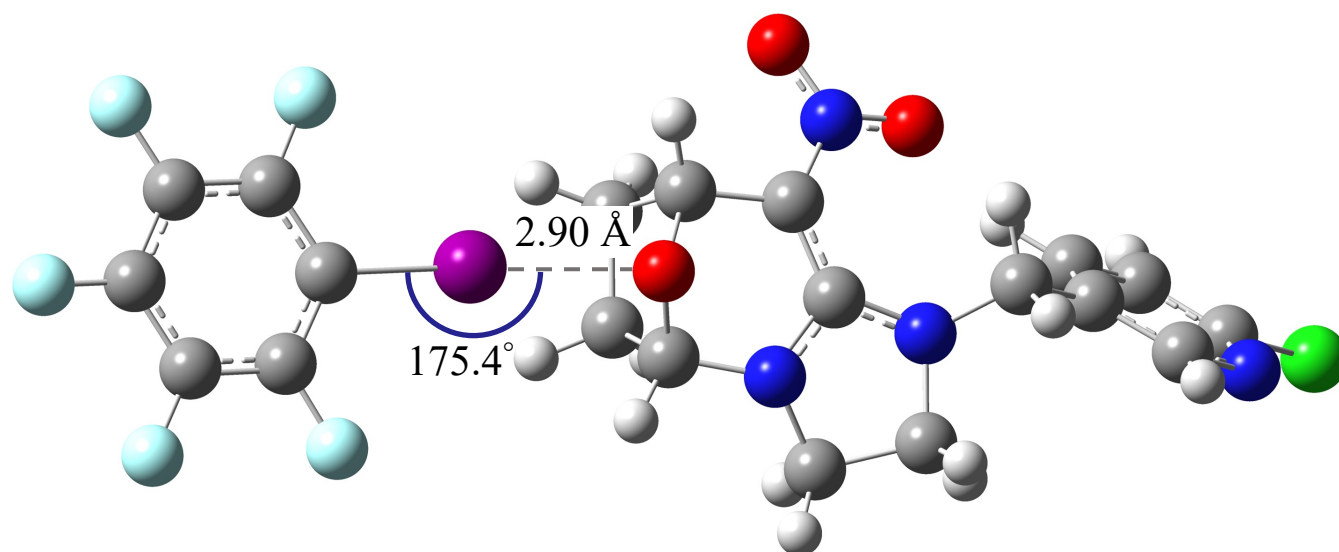
A**B**

Figure S1. Geometry-optimized XB adducts of XB acceptor **cyclozaprid** ($C_{14}H_{15}ClN_4O_3$) at (A) N^1 and (B) O^1 with XB donor **iodopentafluorobenzene (IPFB)**.

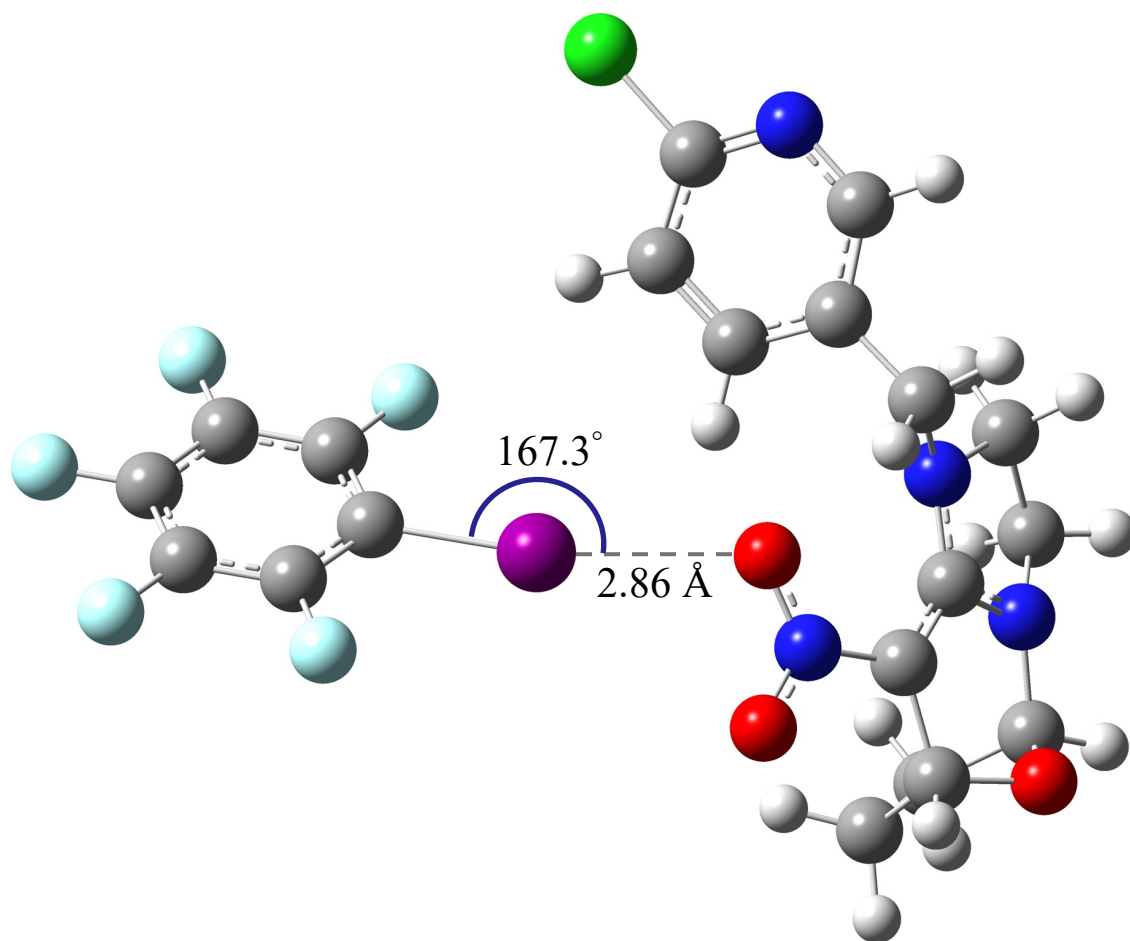


Figure S2. Geometry-optimized XB adducts of XB acceptor **cyclozaprid** ($C_{14}H_{15}ClN_4O_3$) at NO_2 with XB donor **iodopentafluorobenzene (IPFB)**.

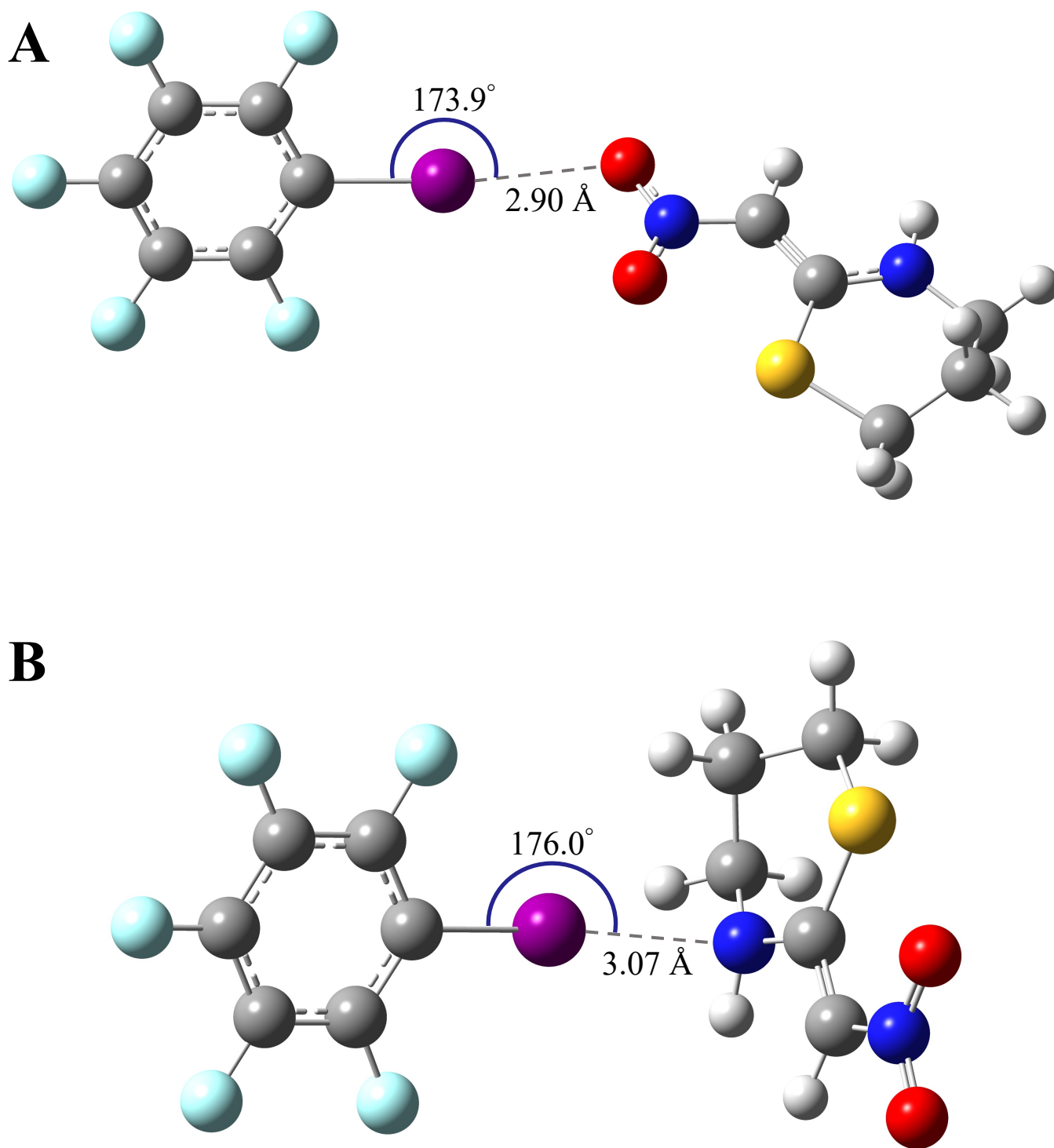


Figure S3. Geometry-optimized XB adducts of XB acceptor **nithiazine** ($C_5H_8N_2O_2S$) at (A) NO_2 and (B) N^1 with XB donor **iodopentafluorobenzene** (IPFB).

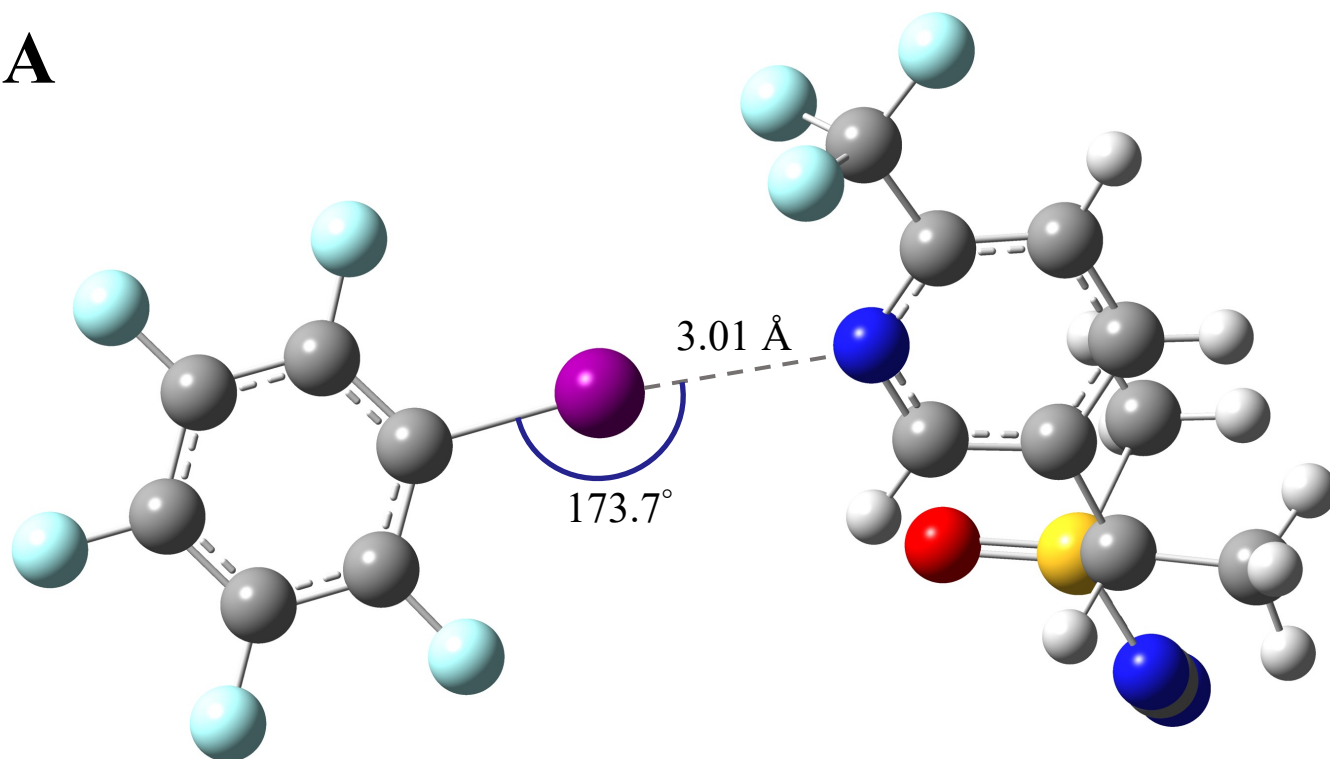
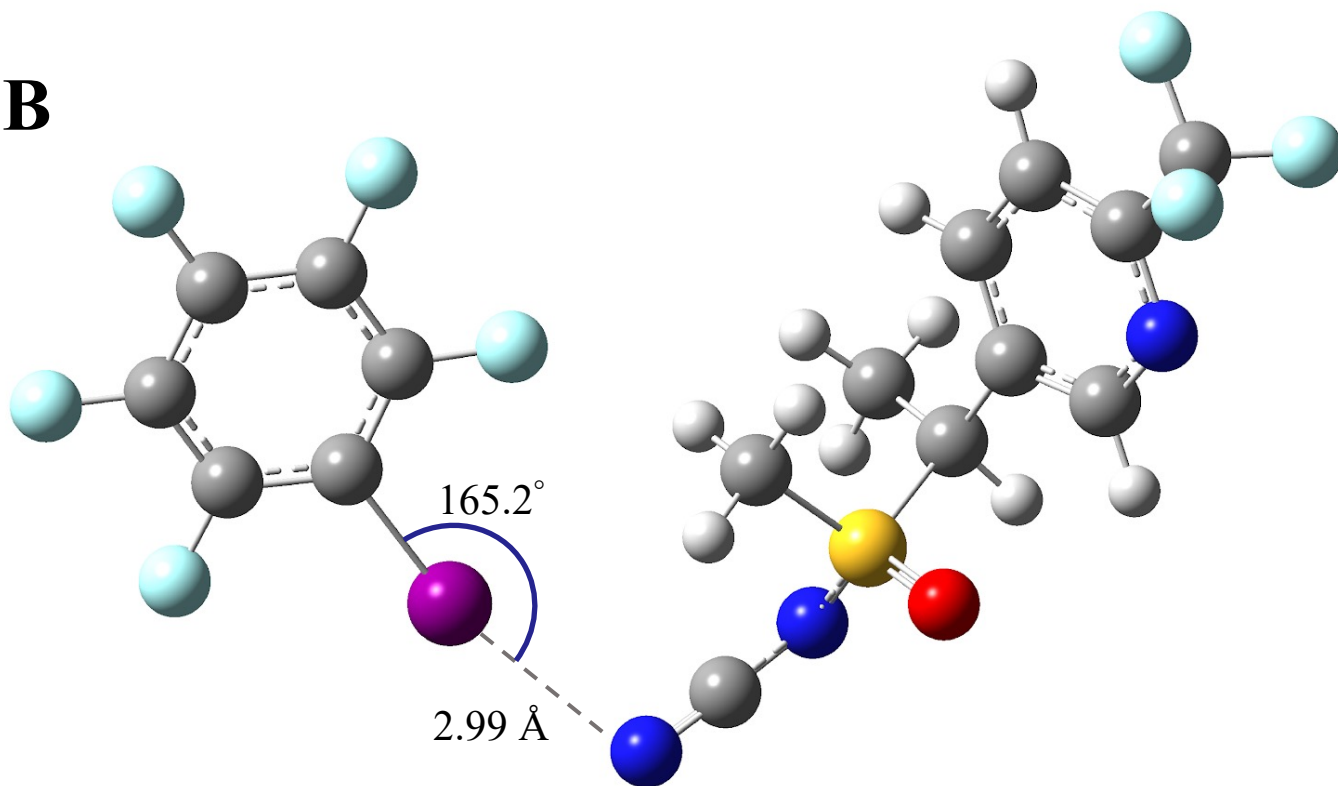
A**B**

Figure S4. Geometry-optimized XB adducts of XB acceptor **sulfoxaflor** ($C_{10}H_{10}F_3N_3OS$) at (A) N^1 and (B) N^2 with XB donor **iodopentafluorobenzene** (IPFB).

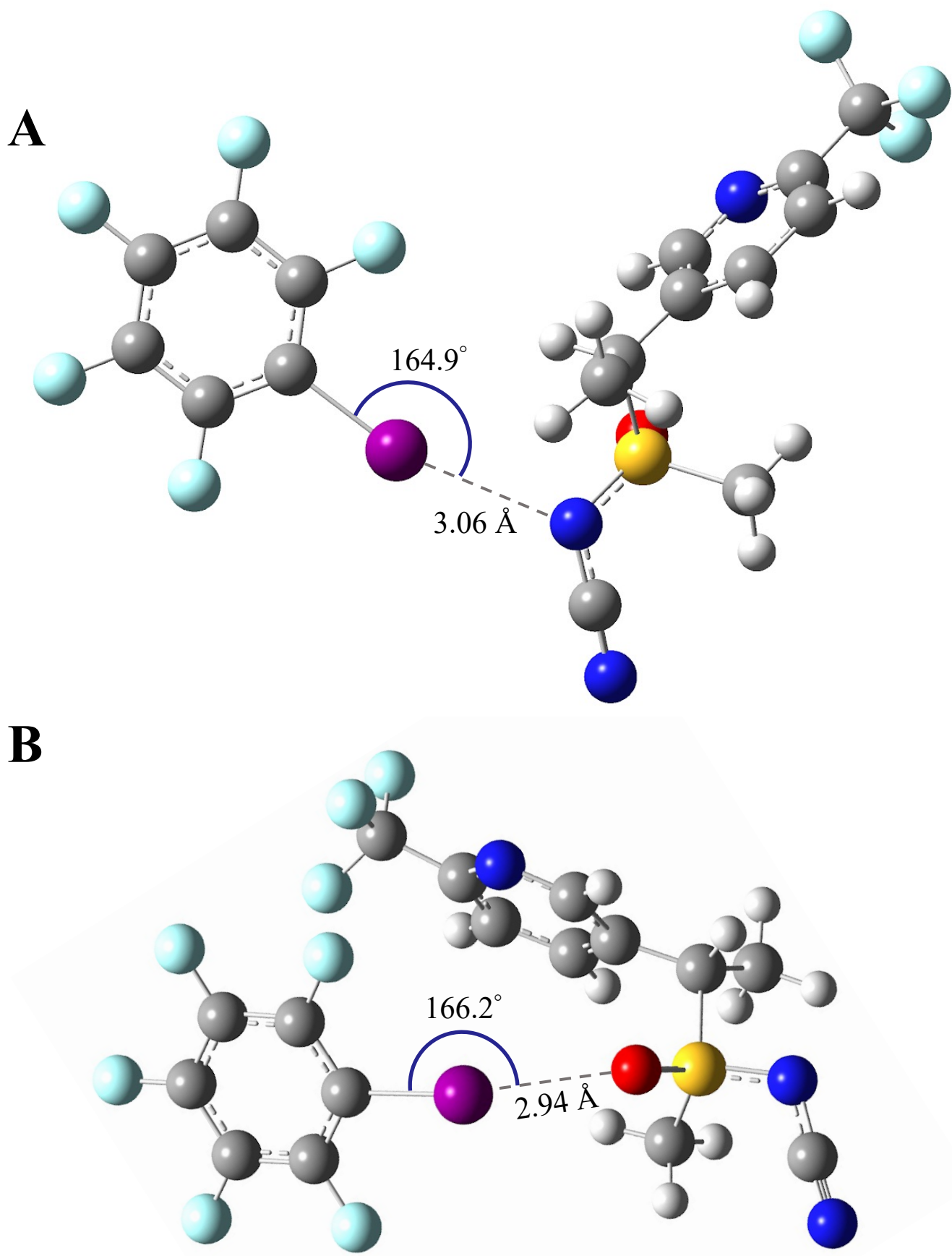


Figure S5. Geometry-optimized XB adducts of XB acceptor **sulfoxaflor** ($C_{10}H_{10}F_3N_3OS$) at (A) N^3 and (B) O^1 with XB donor **iodopentafluorobenzene** (IPFB).

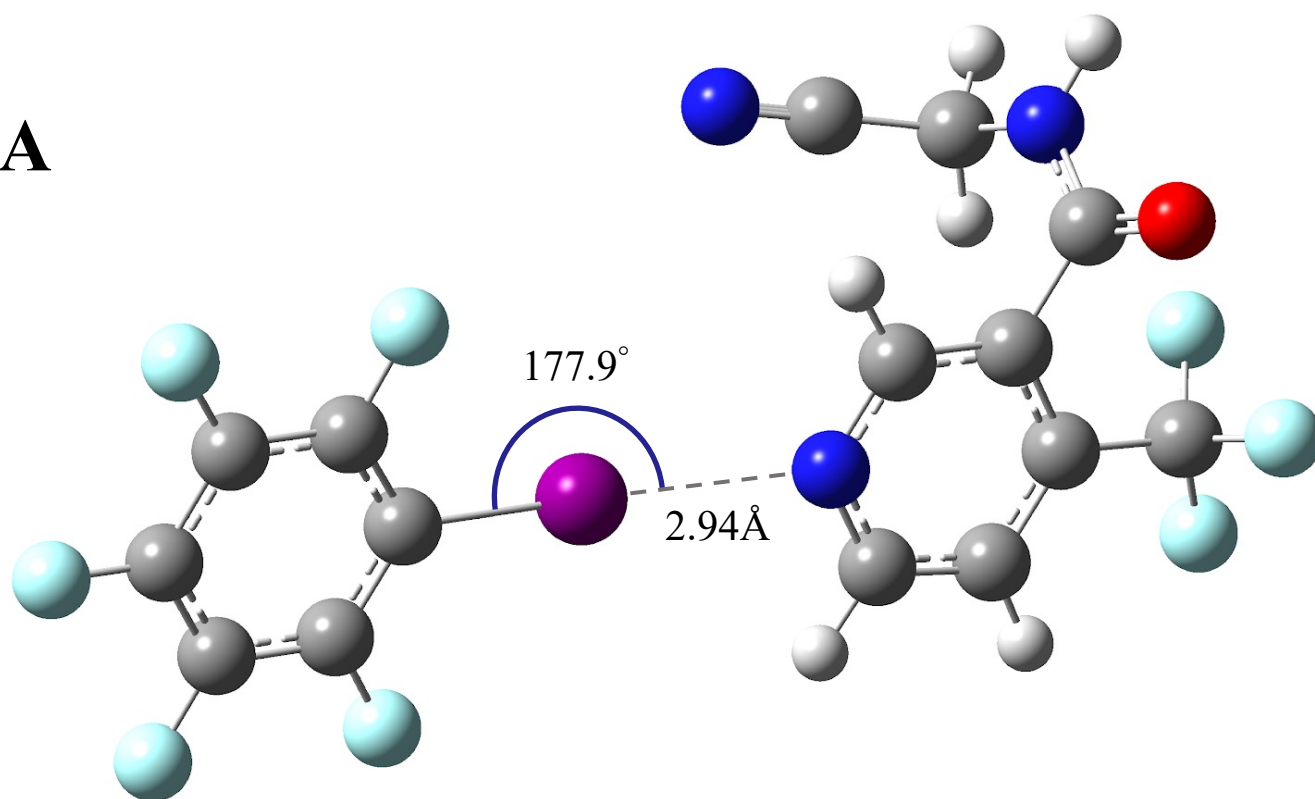
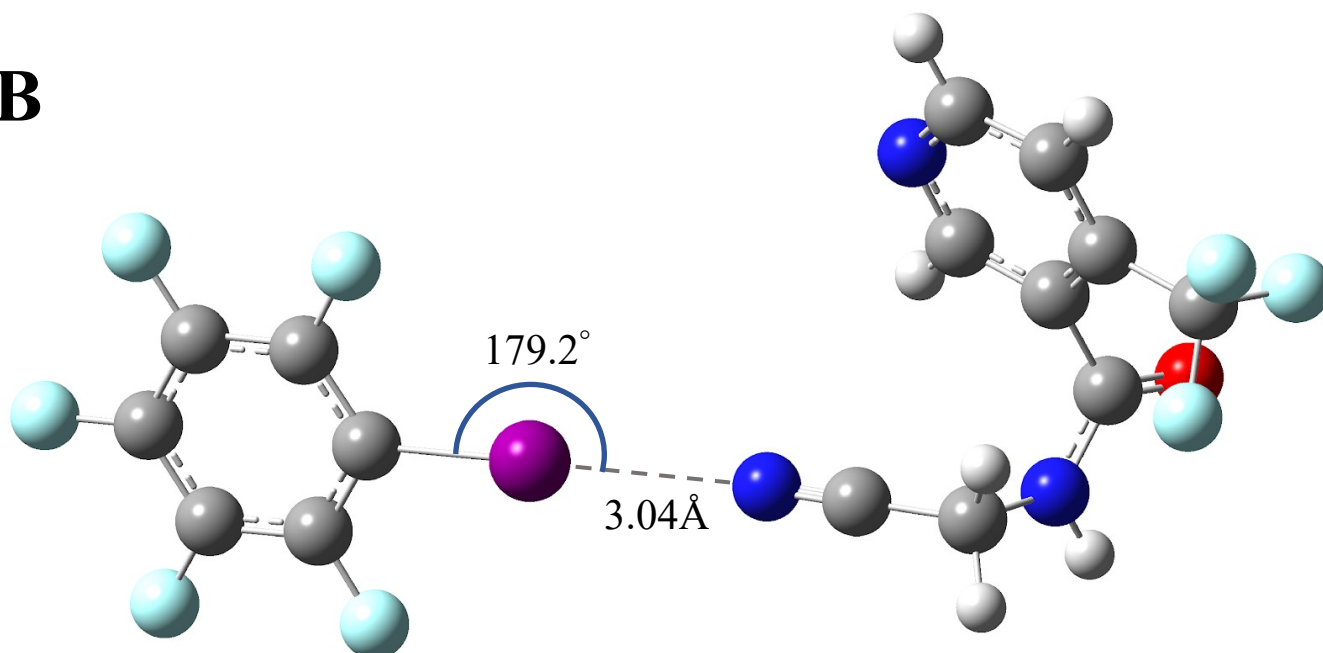
A**B**

Figure S6. Geometry-optimized XB adducts of XB acceptor **flonicamid** ($C_9H_6F_3N_3O$) at (A) N^1 and (B) N^2 with XB donor **iodopentafluorobenzene (IPFB)**.

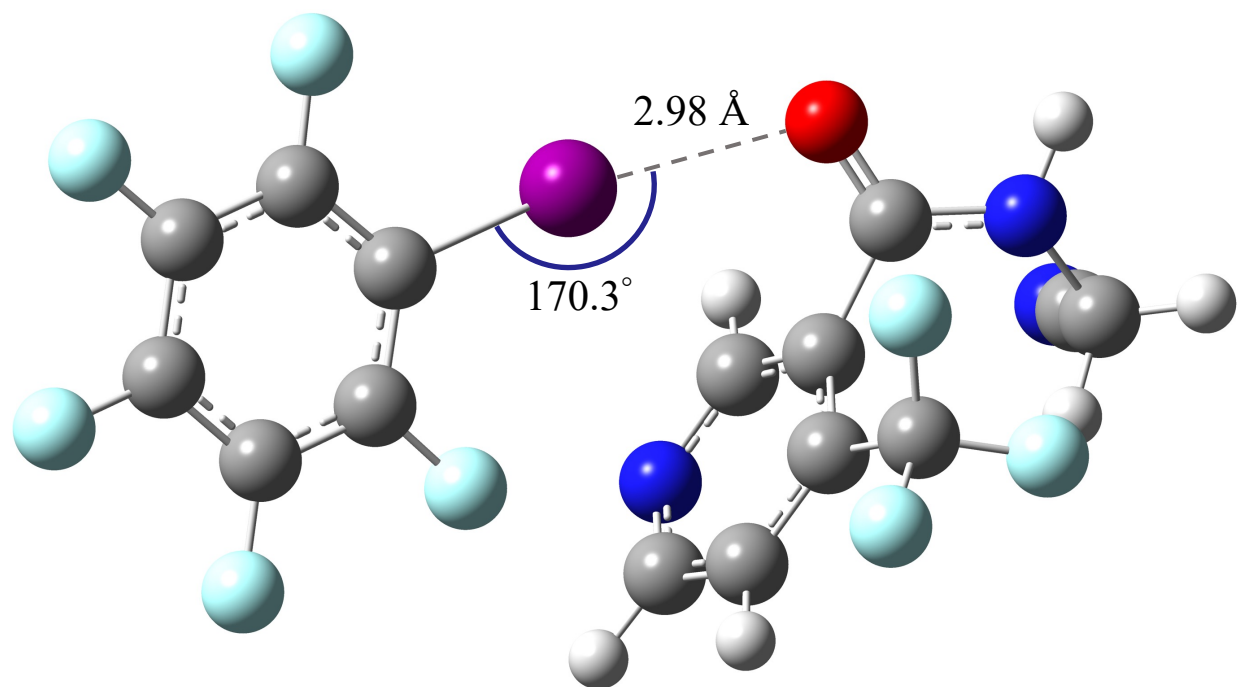


Figure S7. Geometry-optimized XB adducts of XB acceptor **flonicamid** (C₉H₆F₃N₃O) at O¹ with XB donor **iodopentafluorobenzene (IPFB)**.

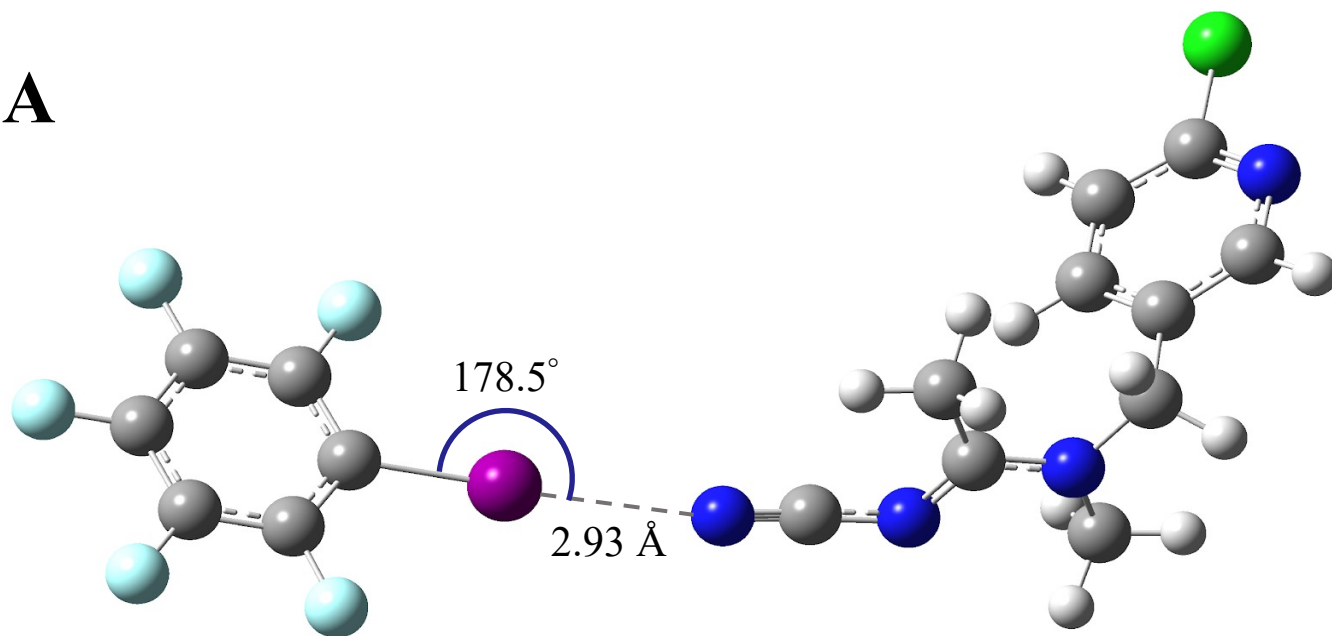
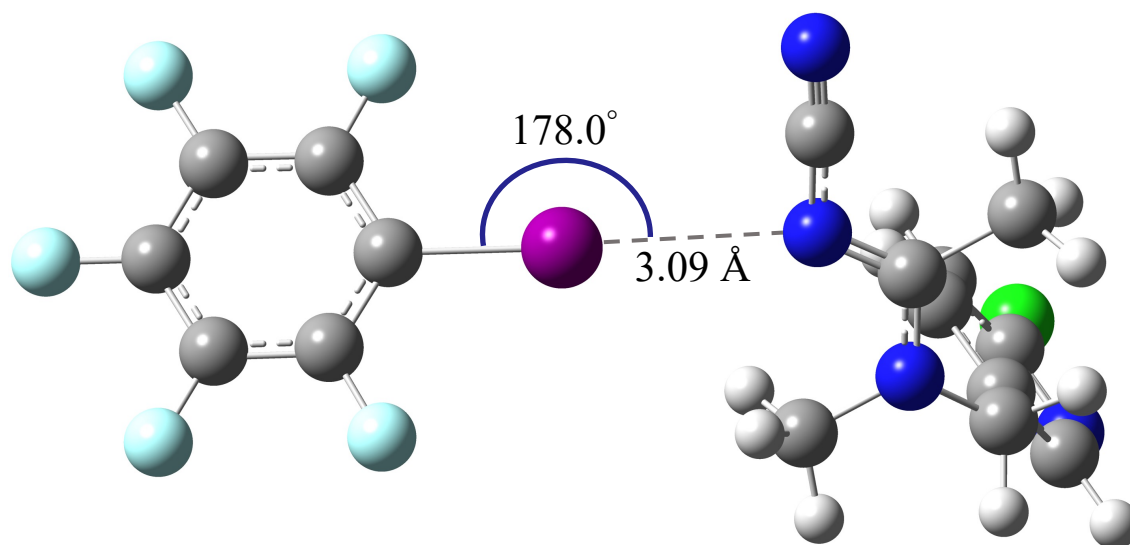
A**B**

Figure S8. Geometry-optimized XB adducts of XB acceptor **acetamiprid** ($C_{10}H_{11}ClN_4$) at (A) N^1 and (B) N^2 with XB donor **iodopentafluorobenzene** (IPFB).

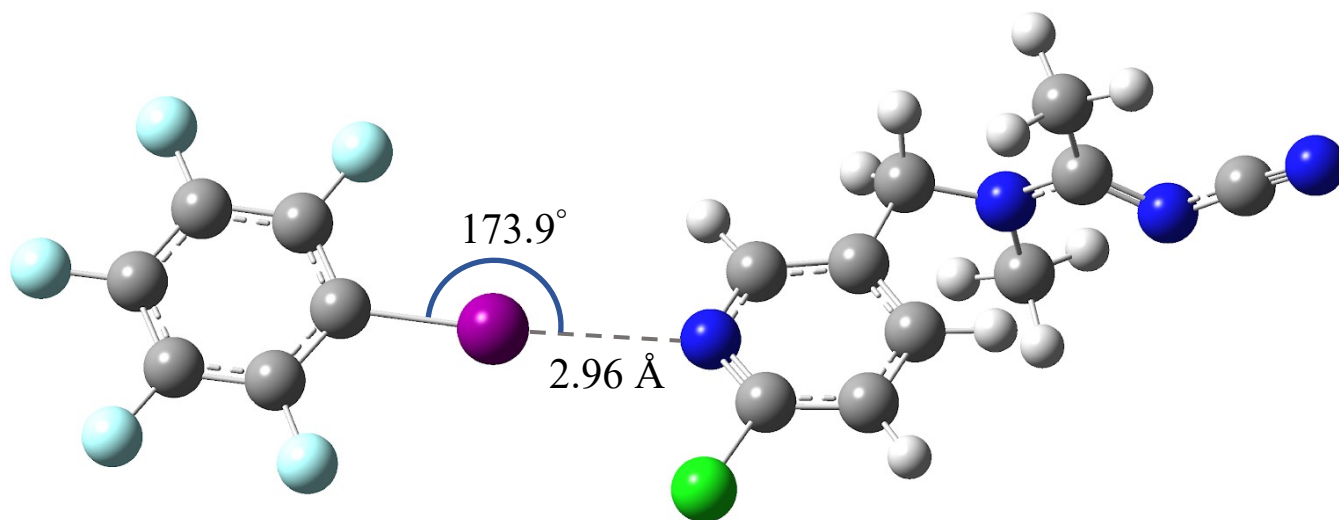


Figure S9. Geometry-optimized XB adducts of XB acceptor **acetamiprid** (C₁₀H₁₁ClN₄) at N³ with XB donor **iodopentafluorobenzene** (IPFB).

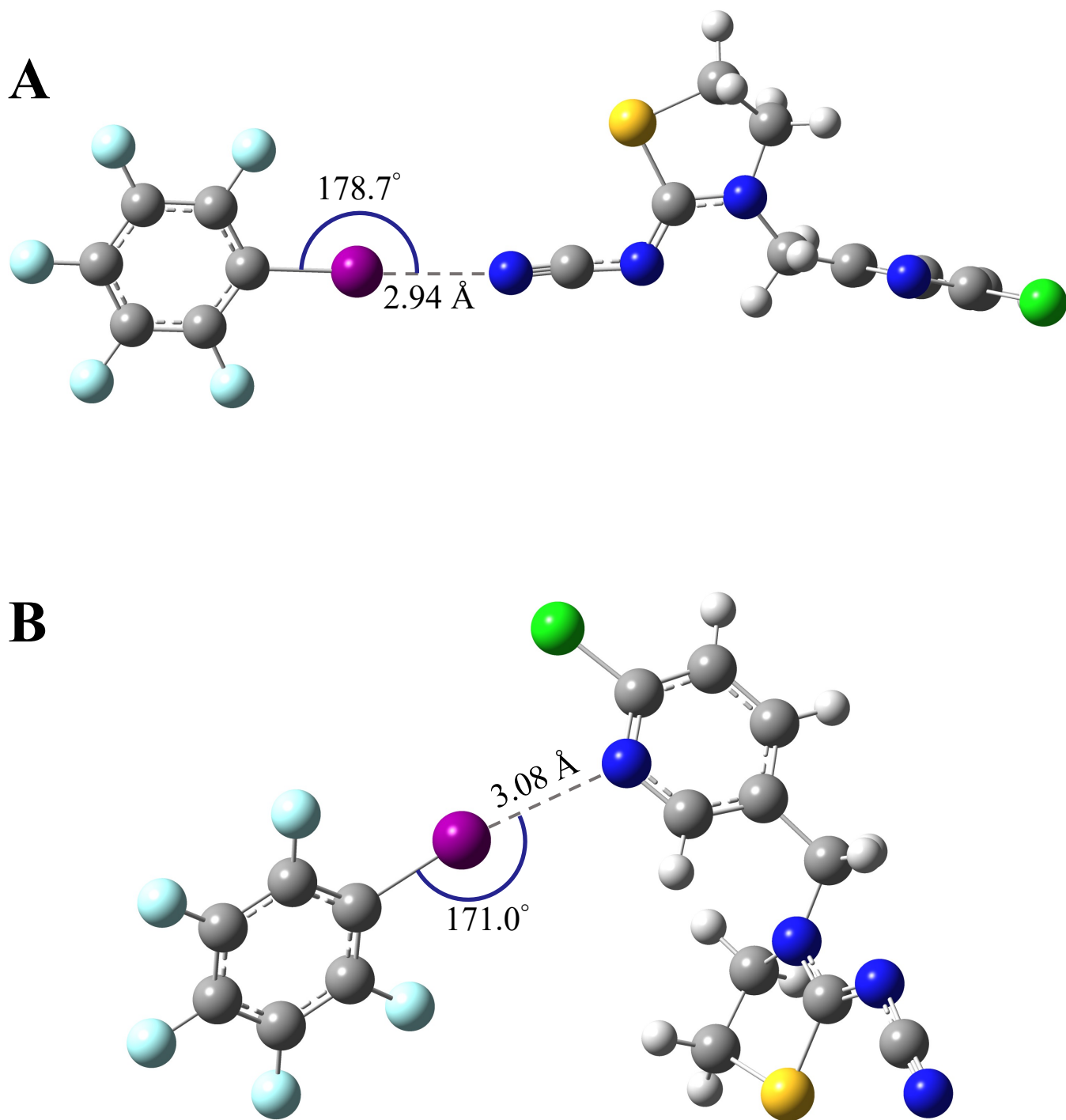


Figure S10. Geometry-optimized XB adducts of XB acceptor **thiacloprid** ($C_{10}H_9ClN_4S$) at (A) N^1 and (B) N^2 with XB donor **iodopentafluorobenzene** (IPFB).

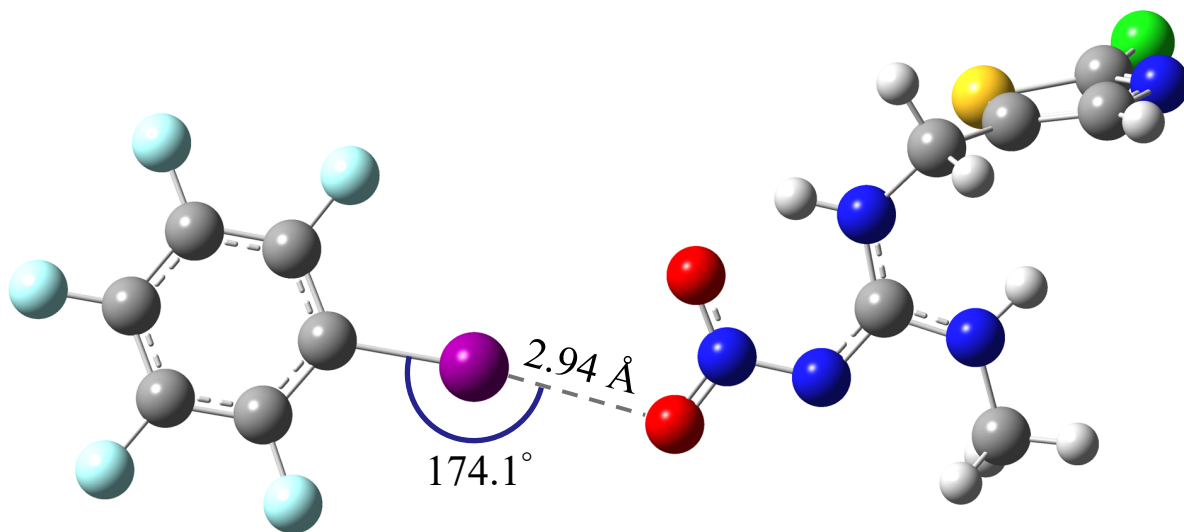
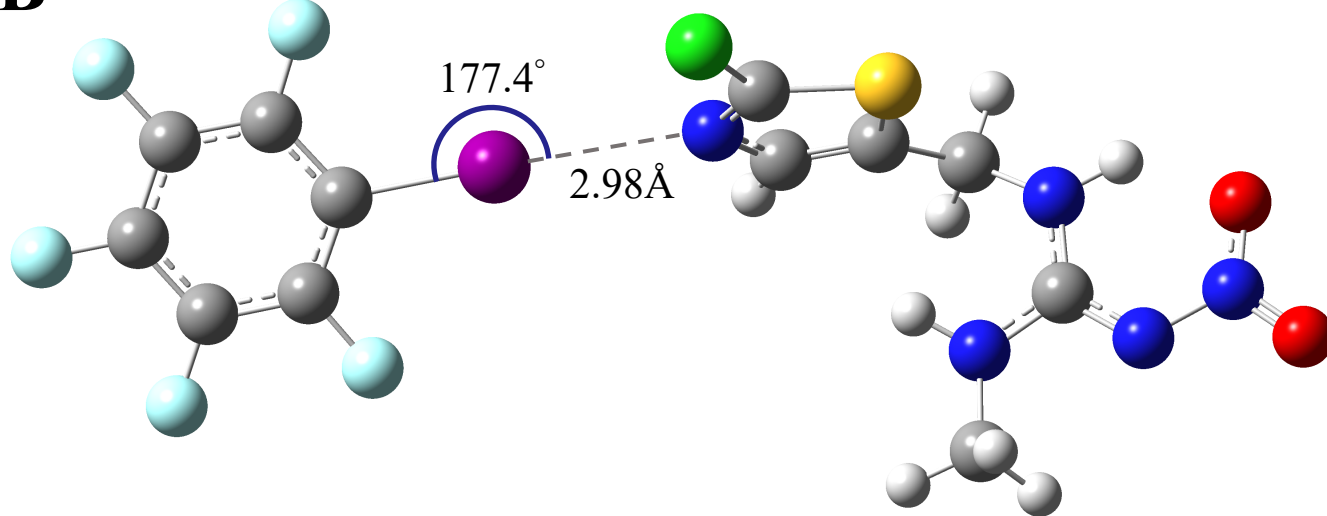
A**B**

Figure S11. Geometry-optimized XB adducts of XB acceptor **clothianidin** ($\text{C}_6\text{H}_8\text{ClN}_5\text{O}_2\text{S}$) at (A) NO_2 and (B) N^1 with XB donor **iodopentafluorobenzene (IPFB)**.

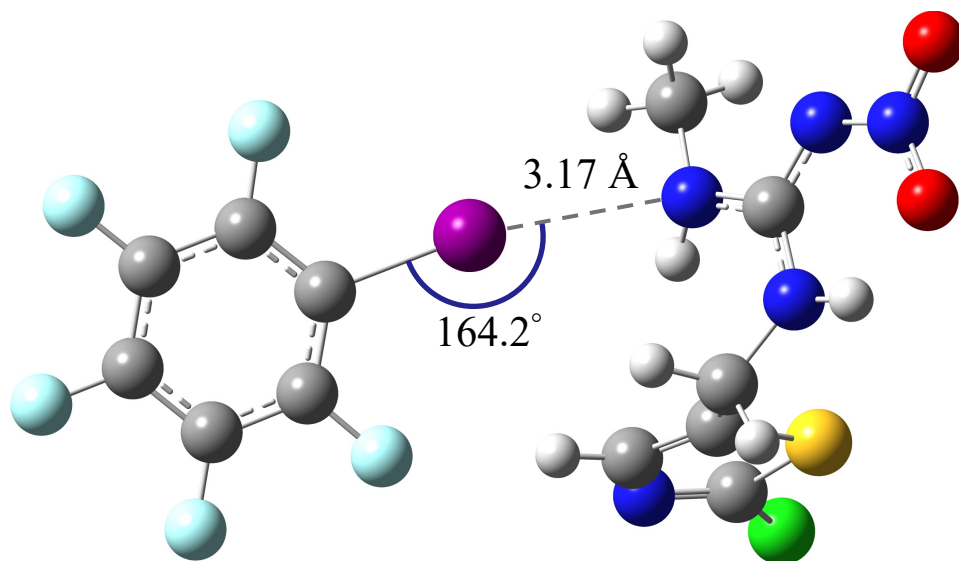


Figure S12. Geometry-optimized XB adducts of XB acceptor **clothianidin** ($C_6H_8ClN_5O_2S$) at N^2 with XB donor **iodopentafluorobenzene (IPFB)**.

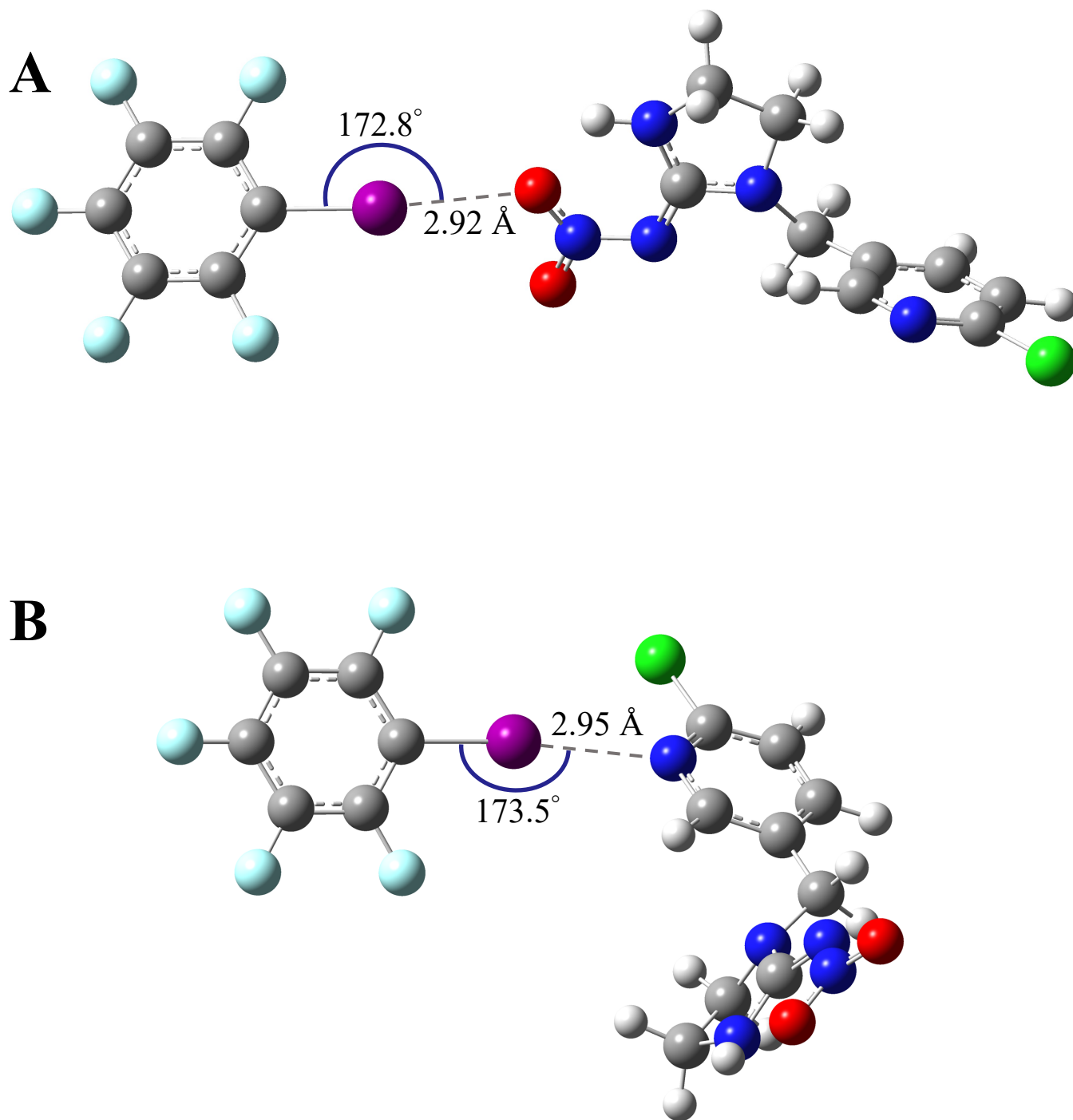


Figure S13. Geometry-optimized XB adducts of XB acceptor **imidacloprid** ($C_9H_{10}ClN_5O_2$) at (A) NO_2 and (B) N^1 with XB donor **iodopentafluorobenzene (IPFB)**.

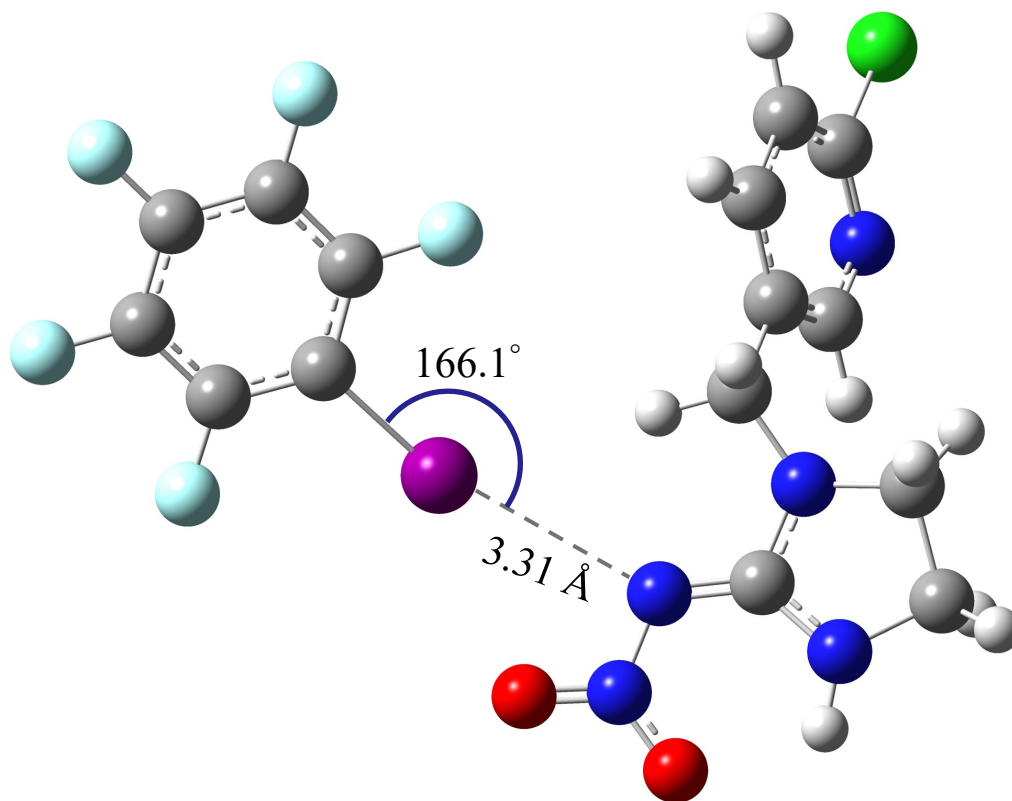


Figure S14. Geometry-optimized XB adducts of XB acceptor **imidacloprid** ($C_9H_{10}ClN_5O_2$) at N^2 with XB donor **iodopentafluorobenzene (IPFB)**.

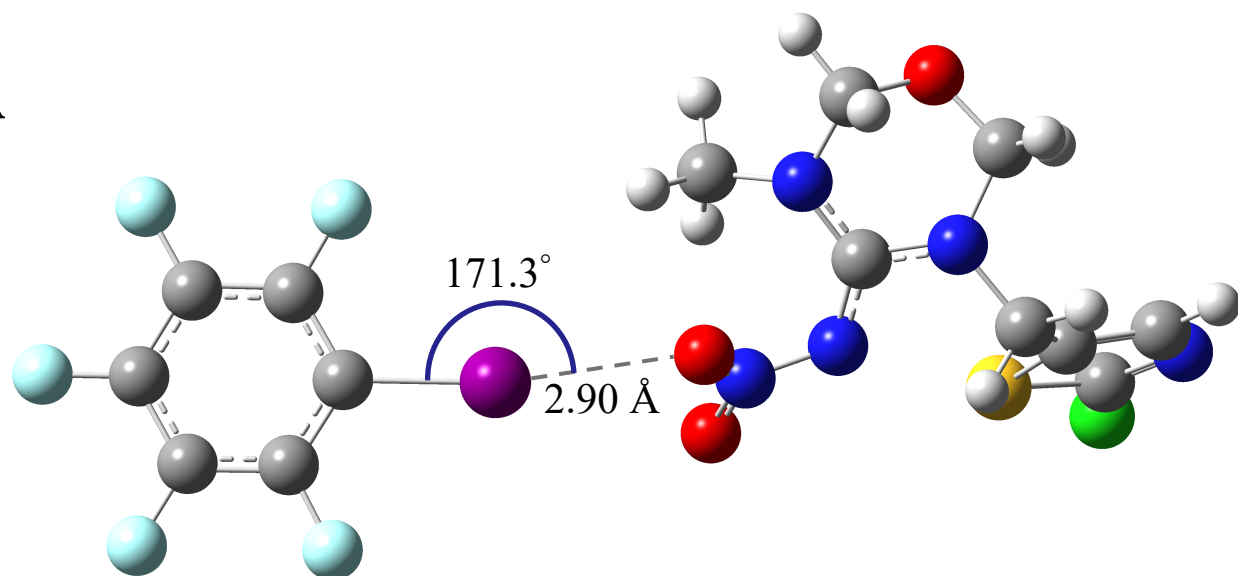
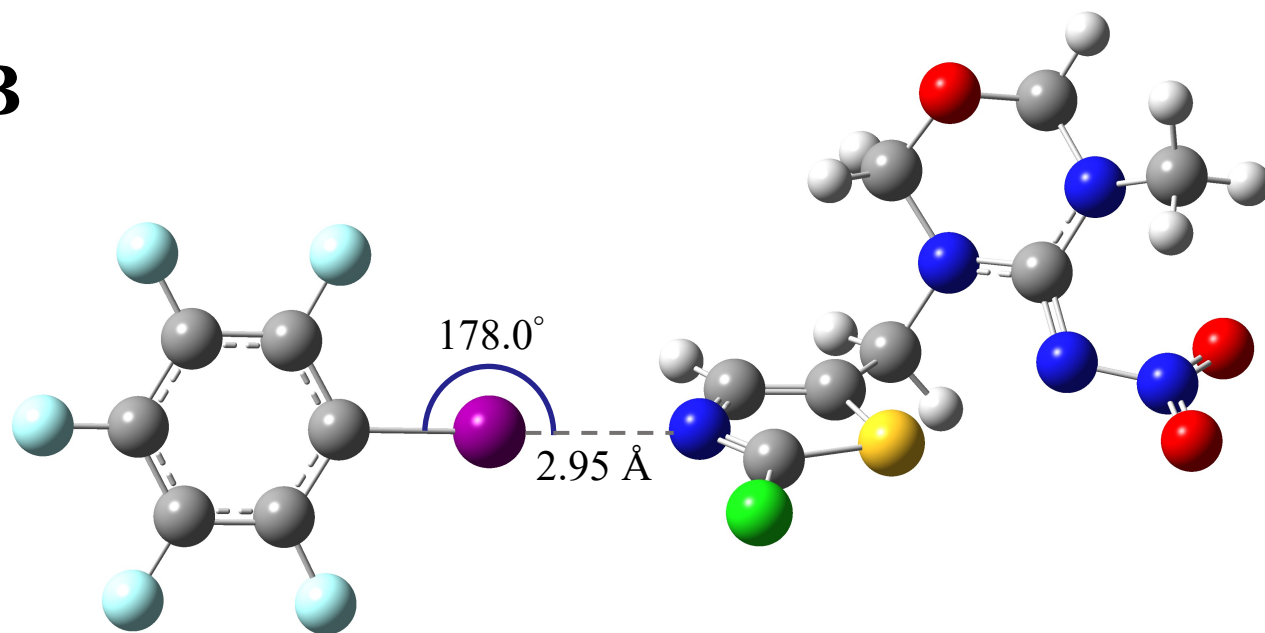
A**B**

Figure S15. Geometry-optimized XB adducts of XB acceptor **thiamethoxam** ($\text{C}_8\text{H}_{10}\text{ClN}_5\text{O}_3$) at (A) NO_2 and (B) N^1 with XB donor **iodopentafluorobenzene (IPFB)**.

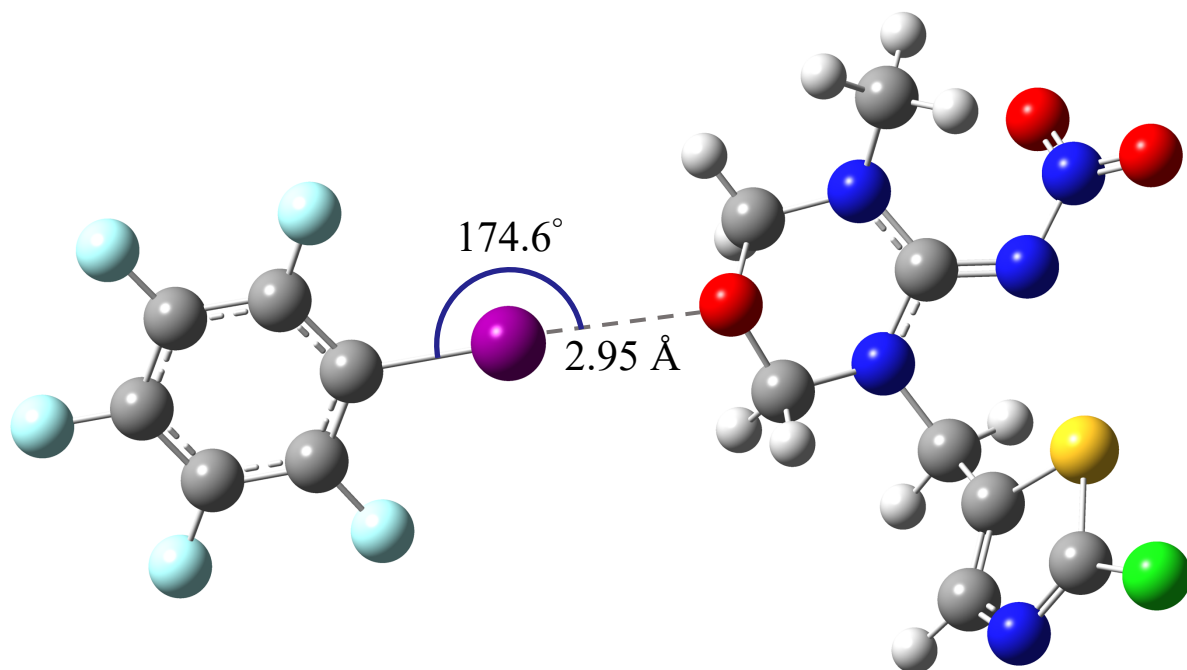


Figure S16. Geometry-optimized XB adducts of XB acceptor **thiamethoxam** ($C_8H_{10}ClN_5O_3$) at O^1 with XB donor **iodopentafluorobenzene (IPFB)**.

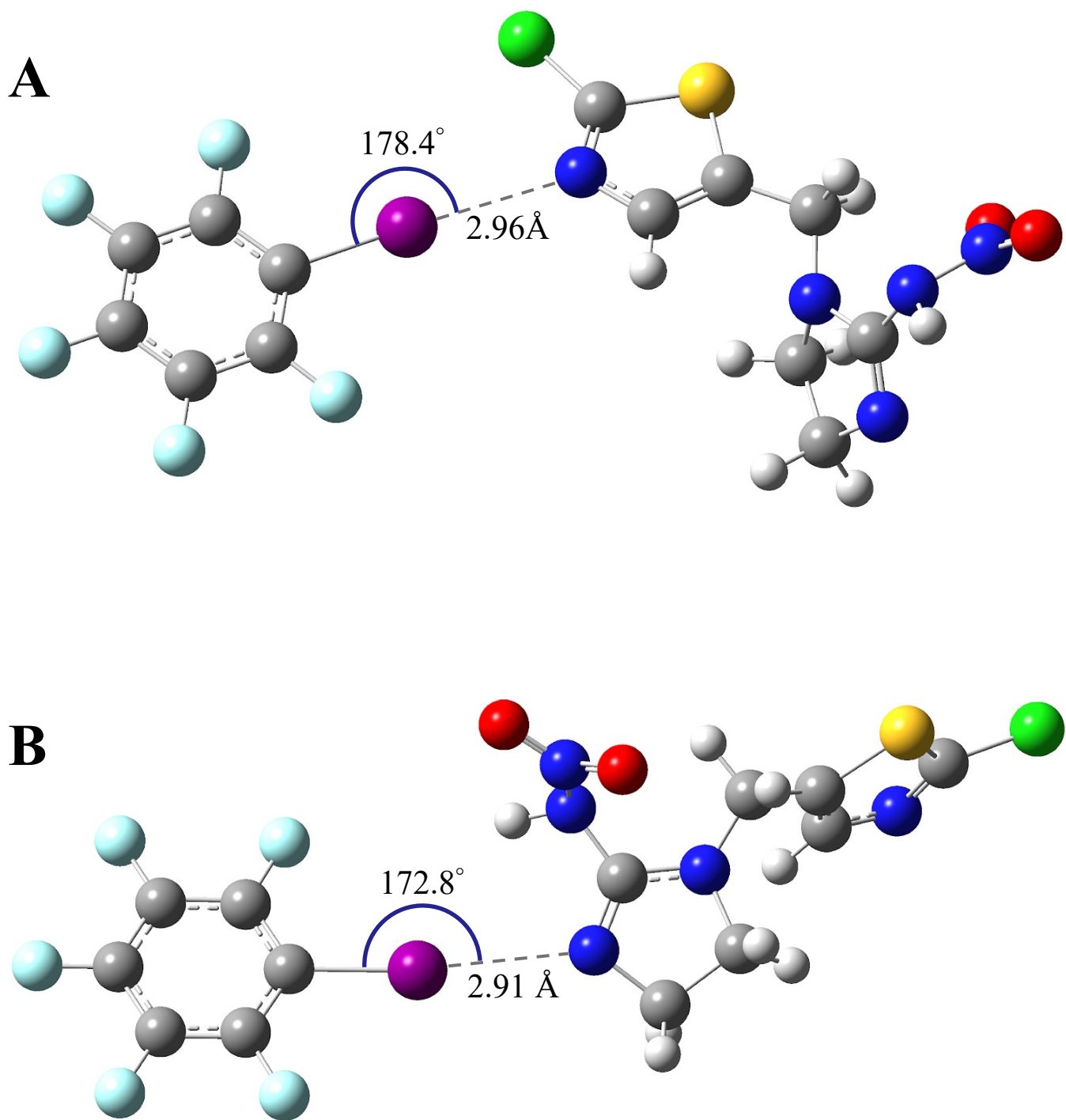


Figure S17. Geometry-optimized XB adducts of XB acceptor **imidaclothiz** ($C_7H_8ClN_5O_2S$) at **(A)** N^1 and **(B)** N^2 with XB donor **iodopentafluorobenzene (IPFB)**.

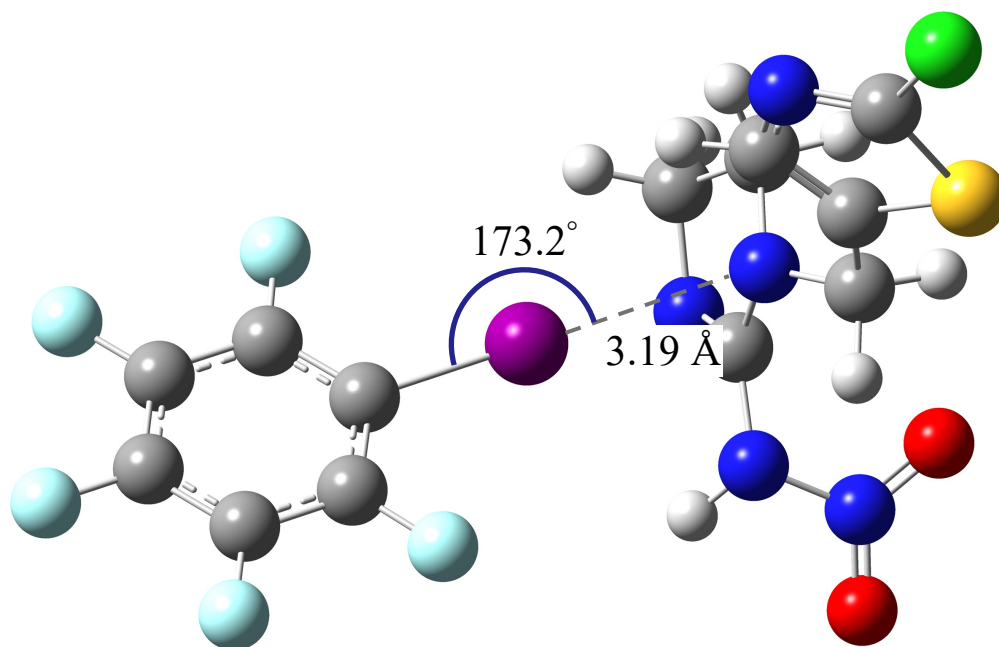
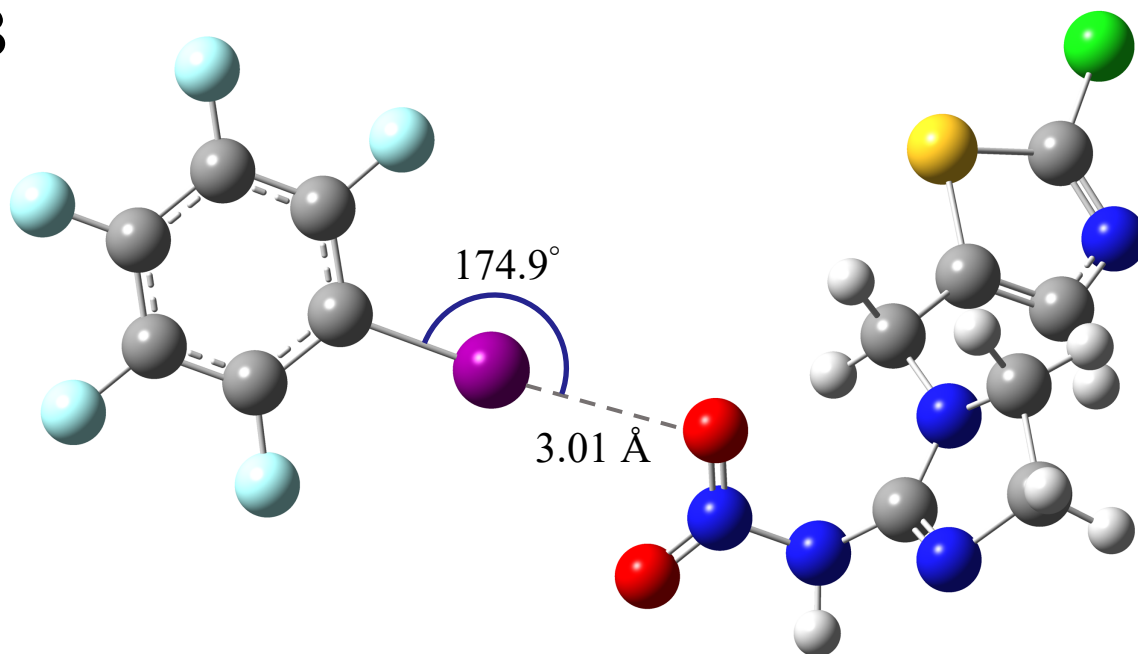
A**B**

Figure S18. Geometry-optimized XB adducts of XB acceptor **imidaclothiz** ($C_7H_8ClN_5O_2S$) at (A) N^3 and (B) NO_2 with XB donor **iodopentafluorobenzene (IPFB)**.

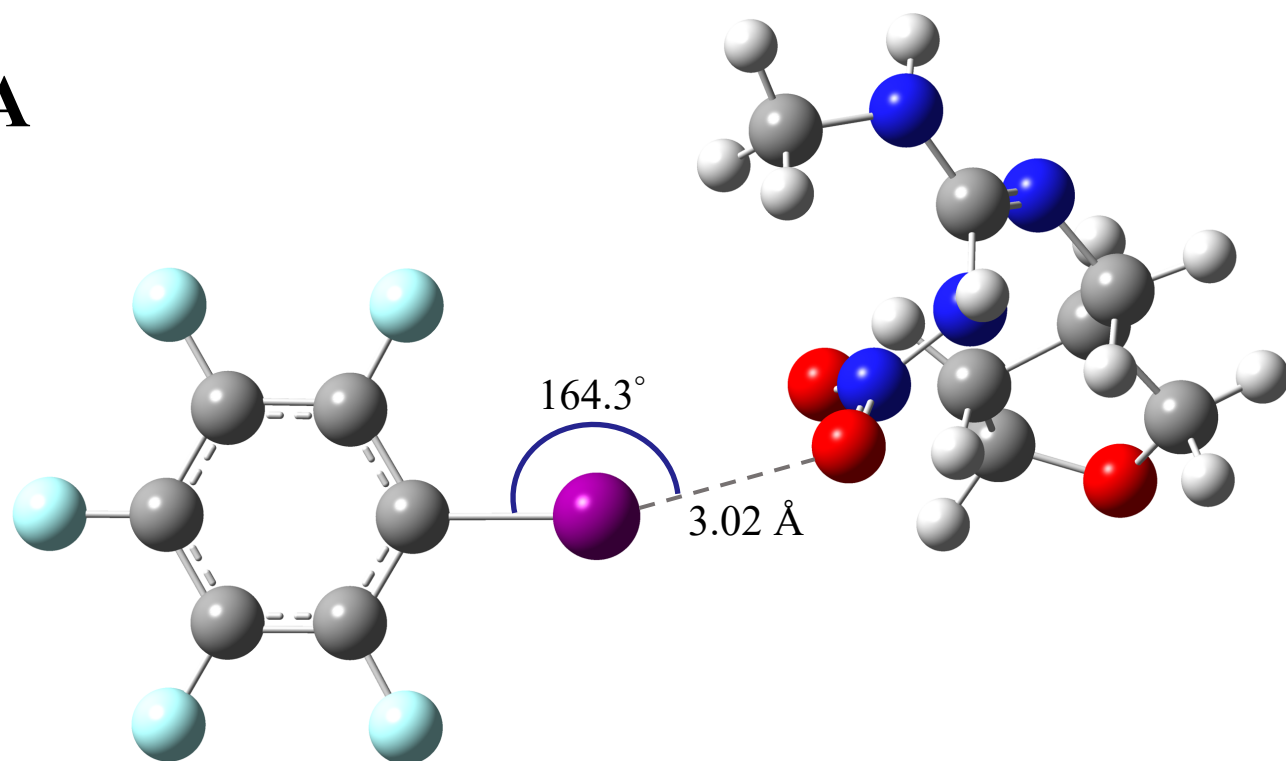
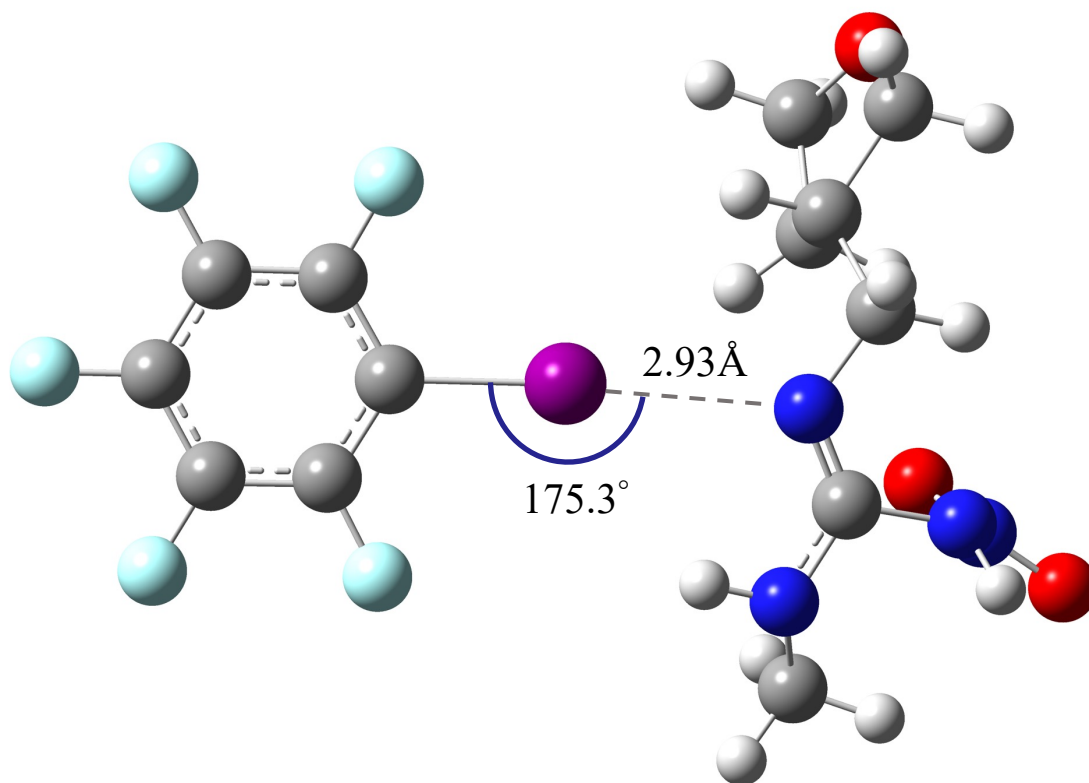
A**B**

Figure S19. Geometry-optimized XB adducts of XB acceptor **dinotefuran** ($C_7H_{14}N_4O_3$) at (A) NO_2 and (B) N^1 with XB donor **iodopentafluorobenzene** (IPFB).

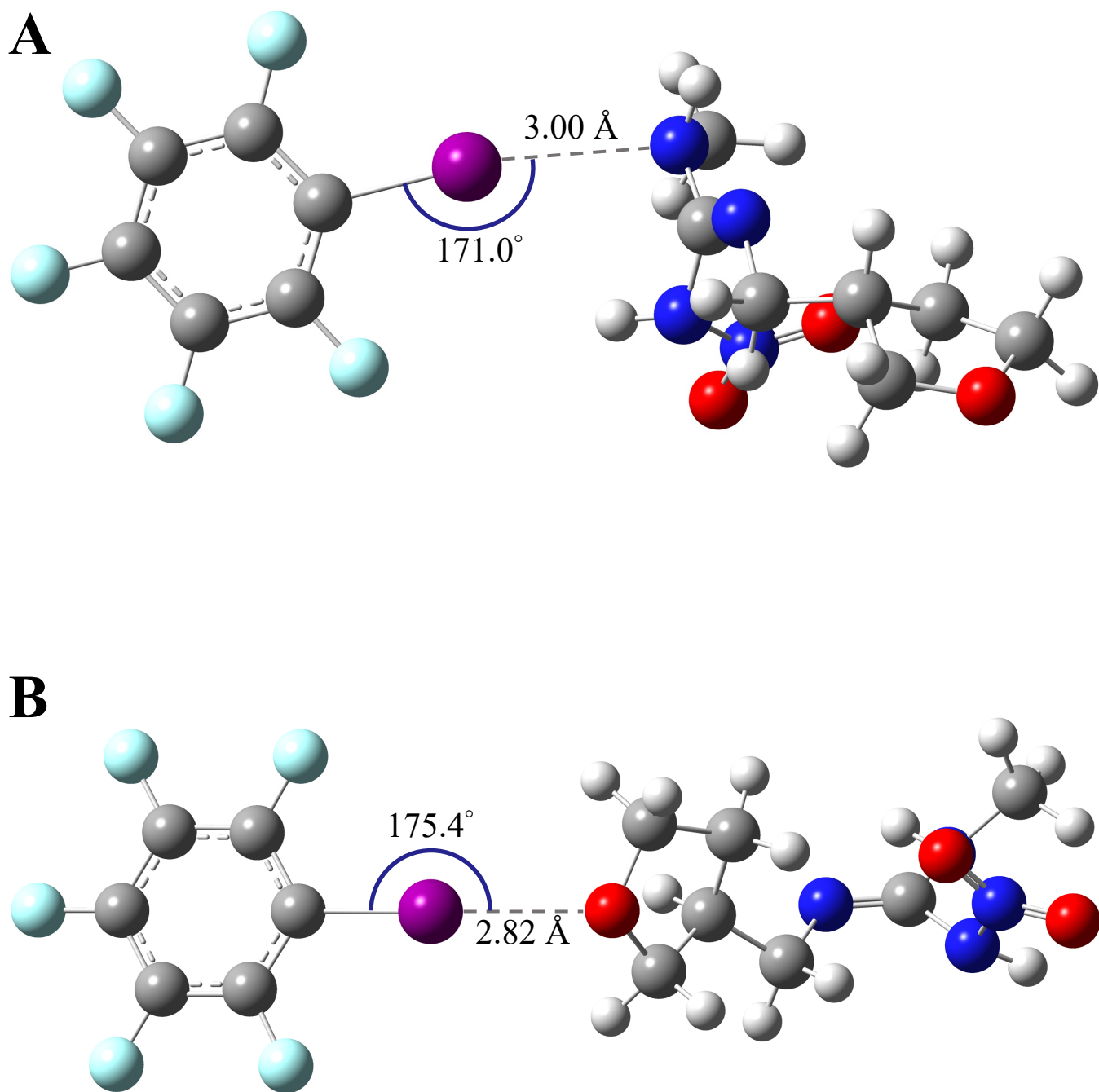


Figure S20. Geometry-optimized XB adducts of XB acceptor **dinotefuran** ($C_7H_{14}N_4O_3$) at (A) N^2 and (B) O^1 with XB donor **iodopentafluorobenzene (IPFB)**.

Table S1. Diffusion-Ordered Spectroscopy (DOSY) NMR Measurements of Diffusion Coefficients (D) for XB Interactions of Thiamethoxam with XB Donors and Control Systems.

#	XB Acceptor	Solvent	XB Donor	Target	Log D (log(m ² /sec))
S-1			None		-8.80 (±0.04)
S-2			IPFB (70 mM)	¹ H Thiamethoxam	-8.85 (±0.04)
S-3	Thiamethoxam (70 mM)	THF-d ₈	PFT (70 mM)		-8.80 (±0.08)
S-4			None		-8.51 (±0.04)
S-5			IPFB (70 mM)	¹ H THF-d ₇ h ₁	-8.53 (±0.03)
S-6			PFT (70 mM)		-8.51 (±0.02)

Notes: DOSY NMR measurements were carried out at 15 minutes after sample preparation.

Table S2. Diffusion-Ordered Spectroscopy (DOSY) NMR Measurements of Diffusion Coefficients (D) of Thiamethoxam in the Presence of *f*-MPCs and *unf*-MPCs.

#	XB Acceptor	Solvent	XB Donor	Target	Log D (log(m ² /sec))
S-7			<i>unf</i> -MPCs	¹ H Thiamethoxam	-8.72 (±0.03)
S-8	Thiamethoxam (70 mM)	THF-d ₈	<i>f</i> -MPCs		-8.76 (±0.04)
S-9			<i>unf</i> -MPCs	¹ H THF-d ₇ h ₁	-8.48 (±0.05)
S-10			<i>f</i> -MPCs		-8.48 (±0.06)

Notes: Concentrations of *unf*-MPCs and *f*-MPCs are equivalent to A₅₁₈ = 0.50 a.u. DOSY NMR measurements of the sample of each NN with either *unf*-MPCs or *f*-MPCs were carried out at 15 minutes after sample preparation.

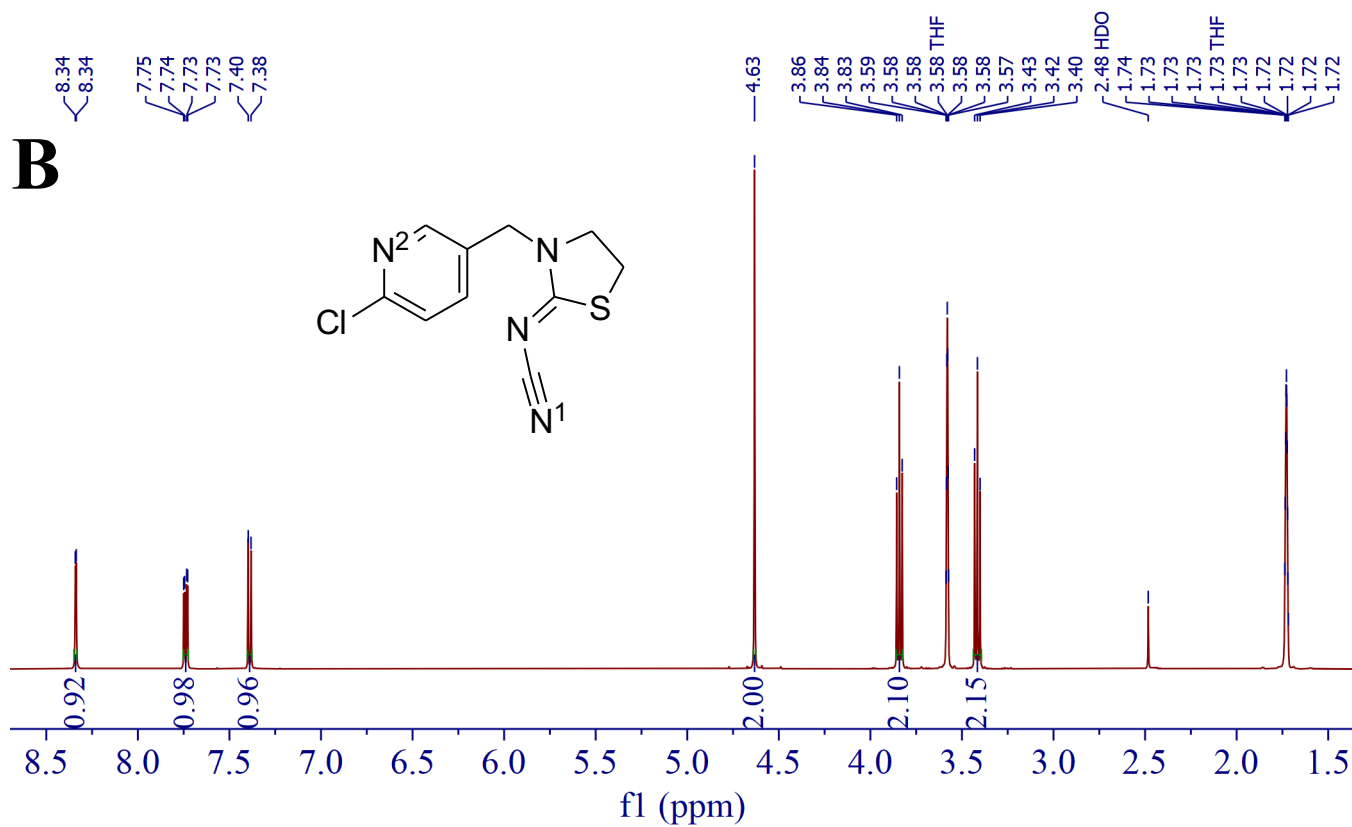
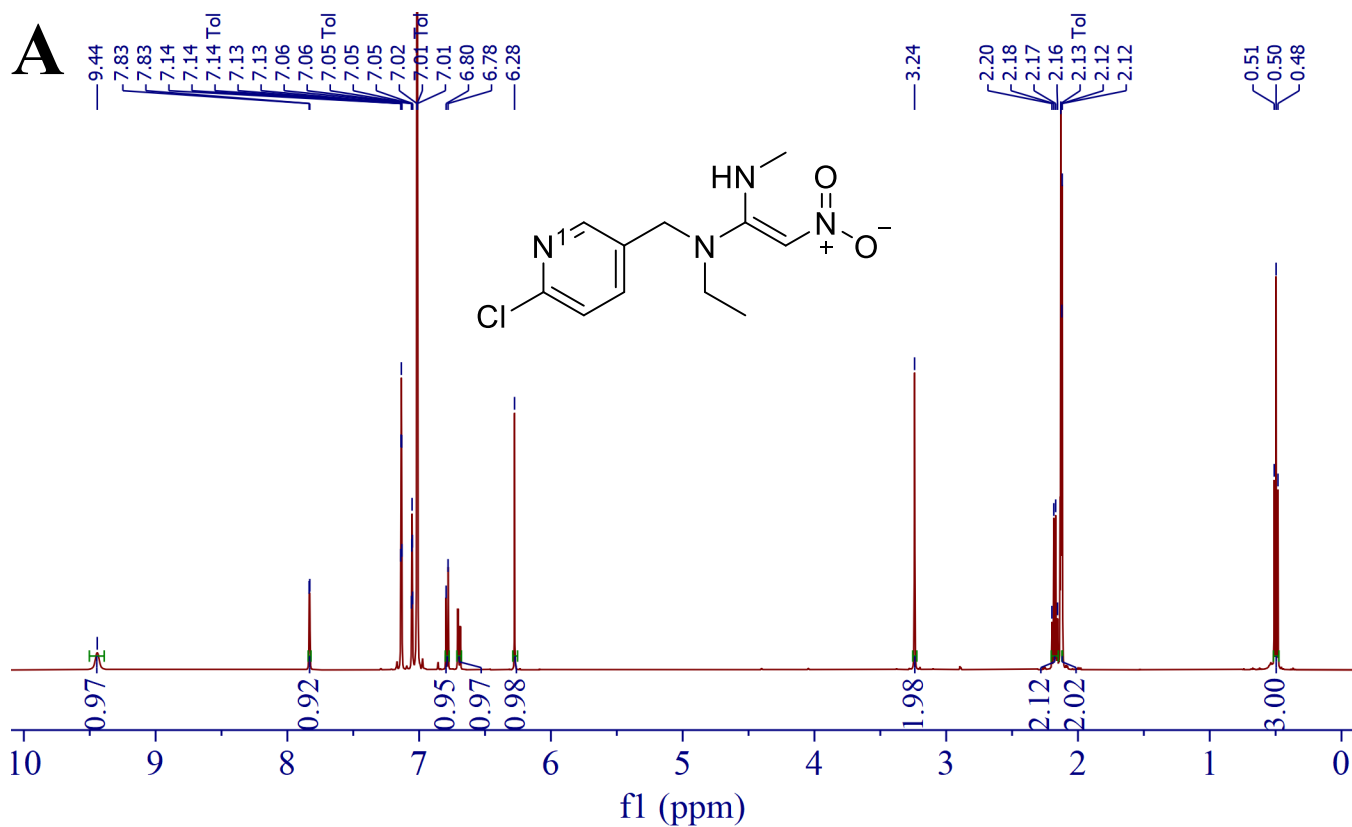


Figure S21. (A) ^1H NMR (400 MHz) spectra of (A) nitenpyram (in toluene- d_8) and (B) thiacloprid (in tetrahydrofuran- d_8) at 298K.

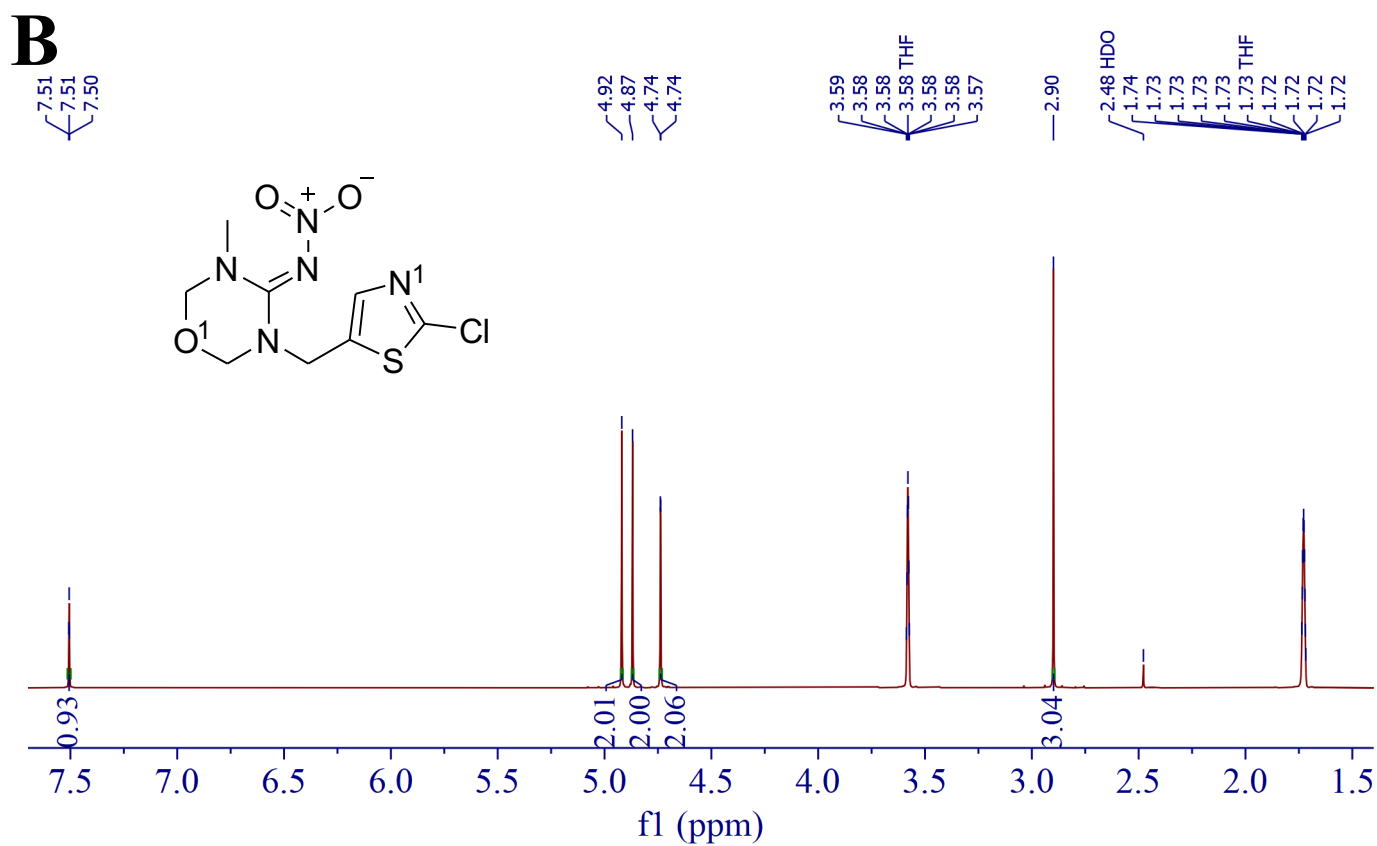
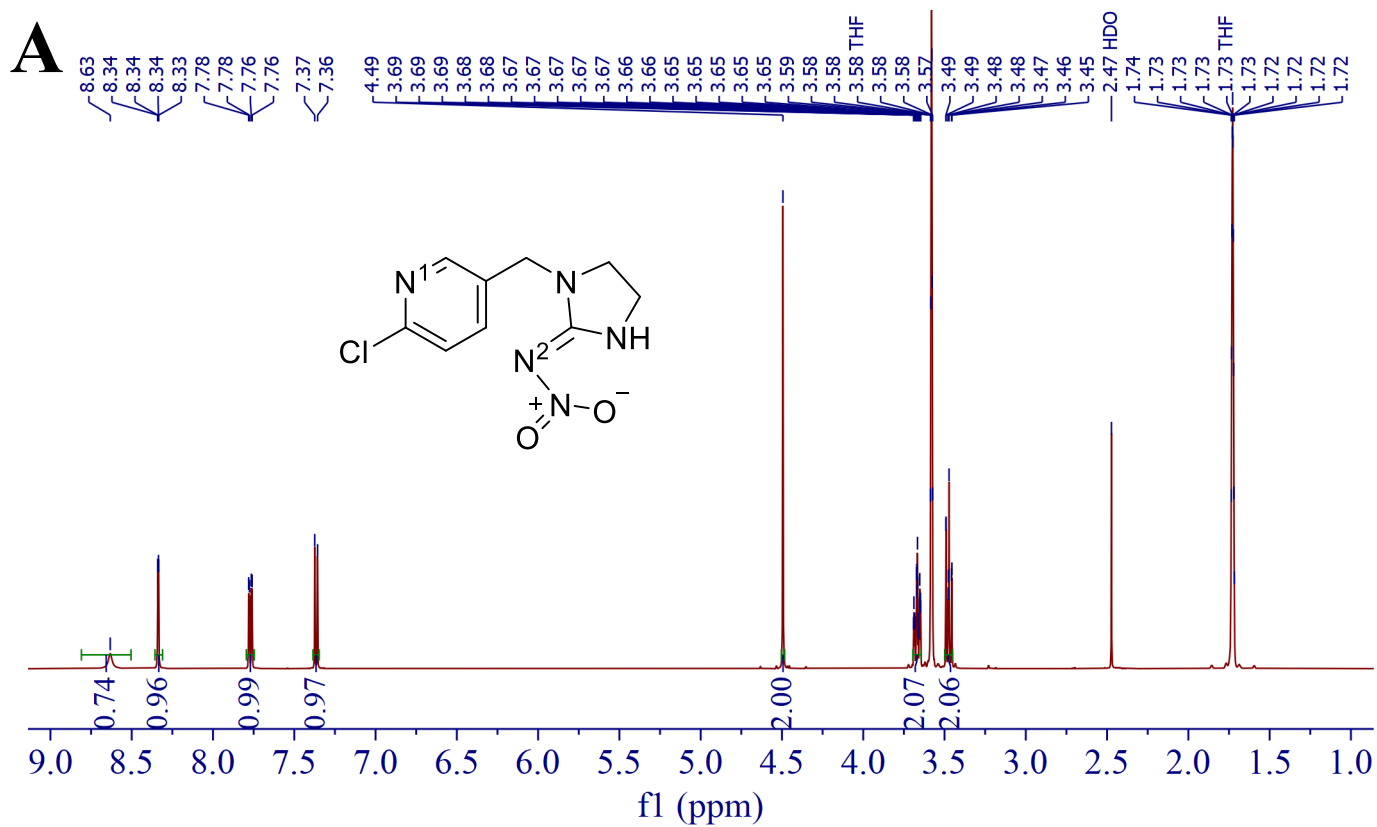


Figure S22. (A) ¹H NMR (400 MHz) spectra of (A) imidacloprid and (B) thiamethoxam in tetrahydrofuran-d₈ at 298K.

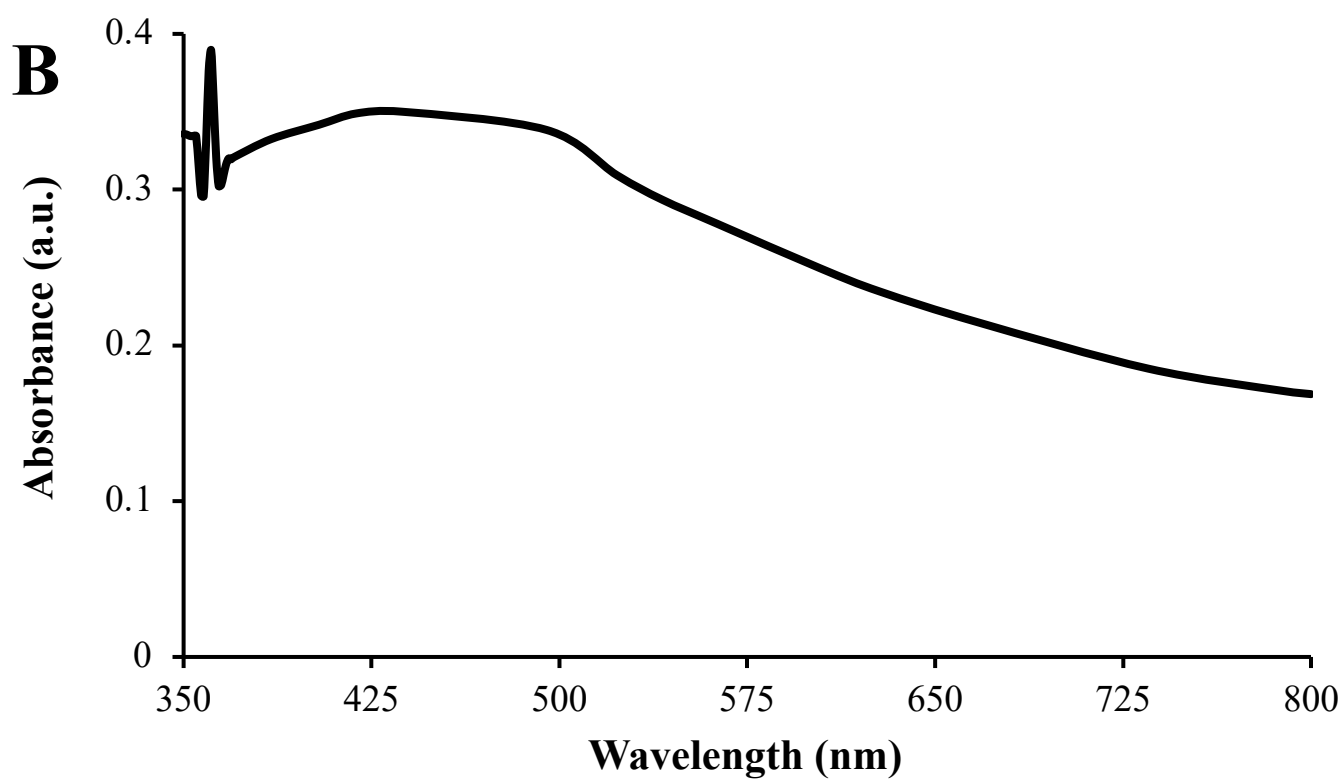
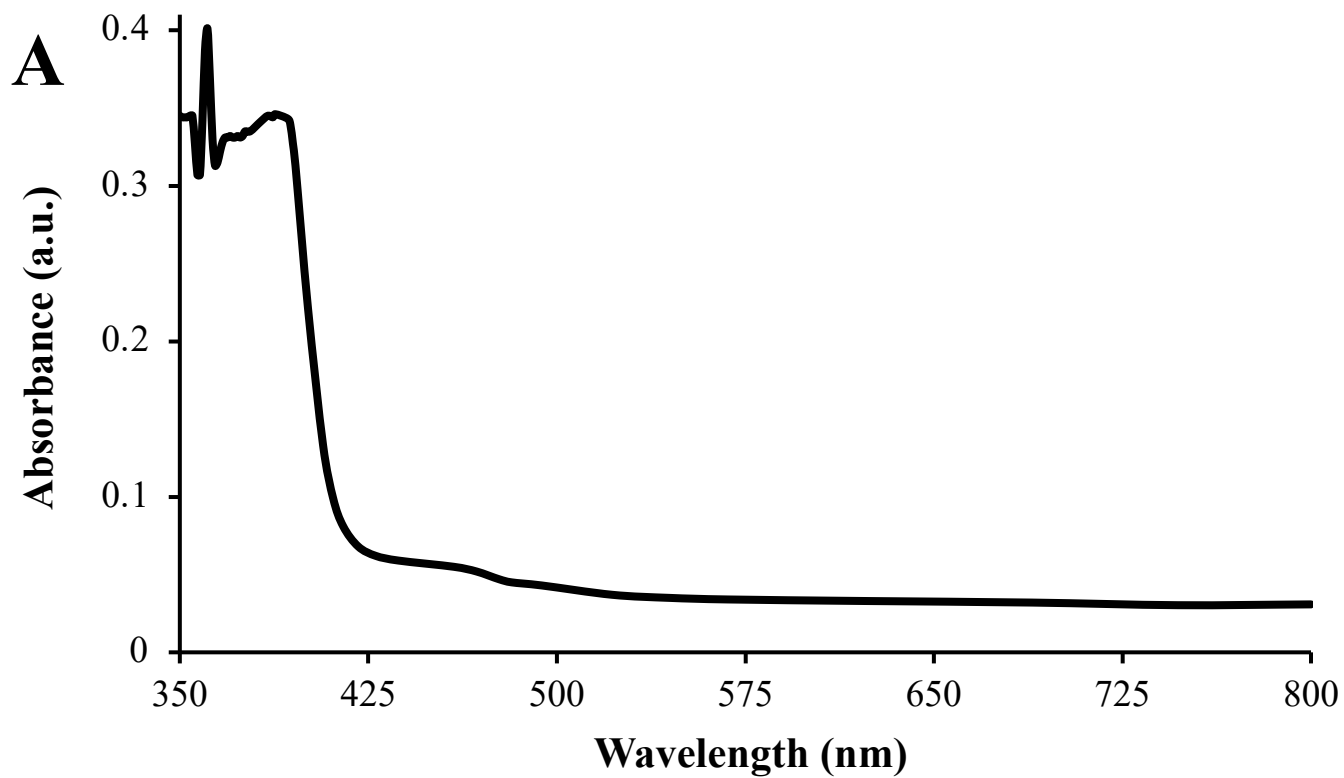


Figure S23. UV-Vis spectra of **nitenpyram** at (A) 11 mM in toluene and (B) 246 mM in tetrahydrofuran.

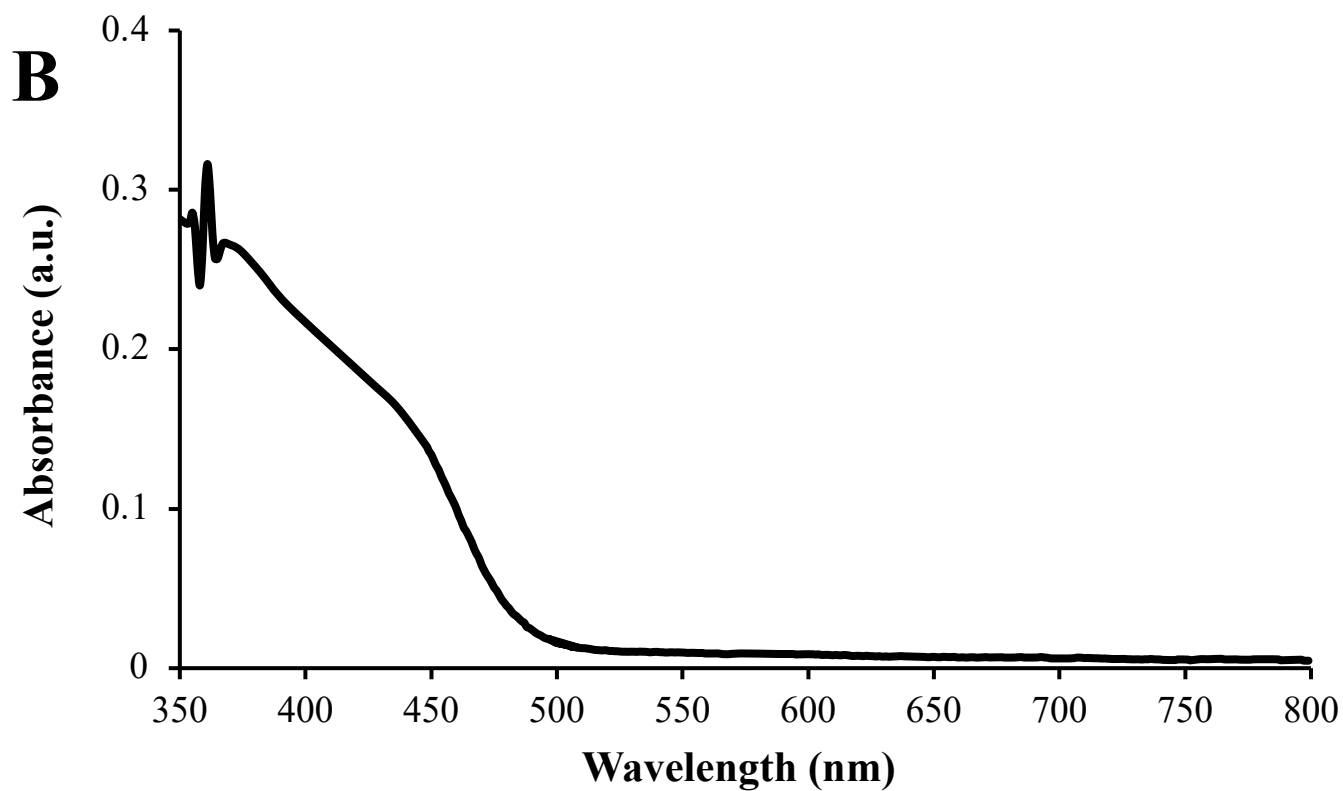
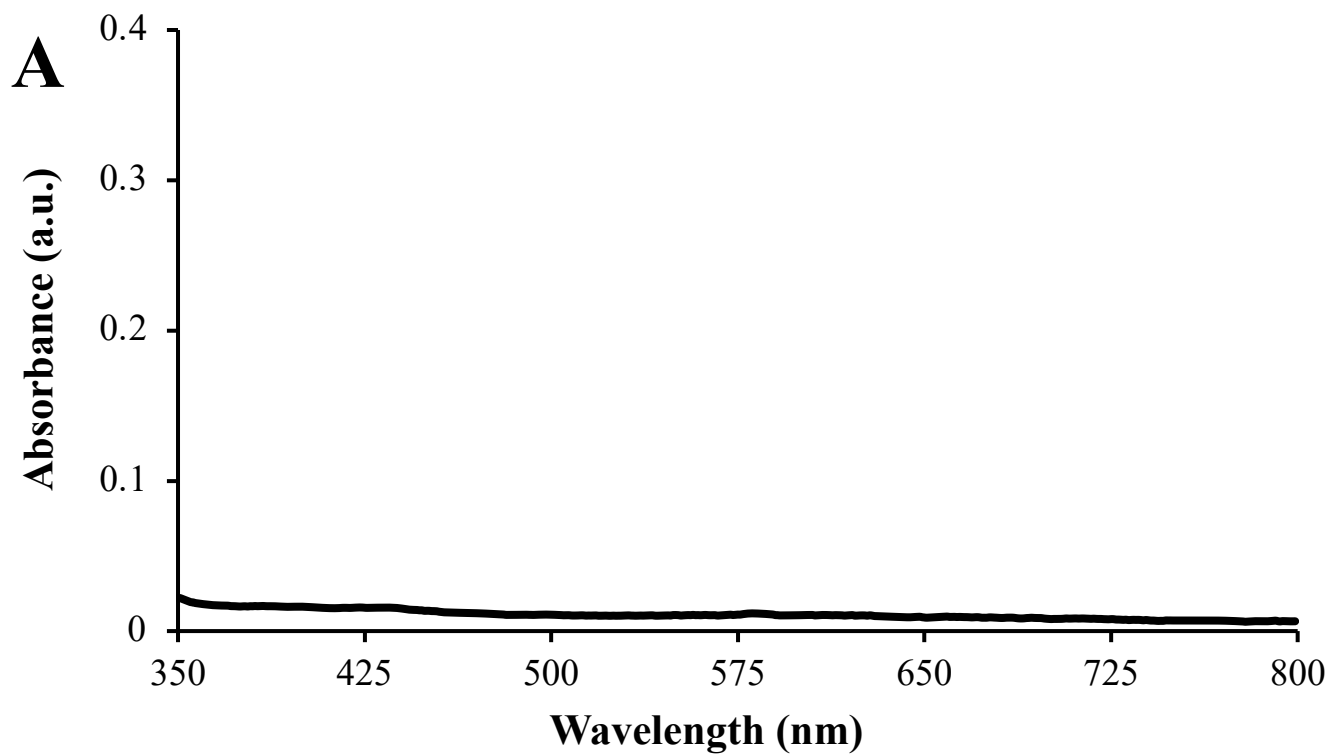


Figure S24. UV-Vis spectra of **(A) sulfoxaflor (72 mM)** and **(B) acetamiprid (75 mM)** in tetrahydrofuran.

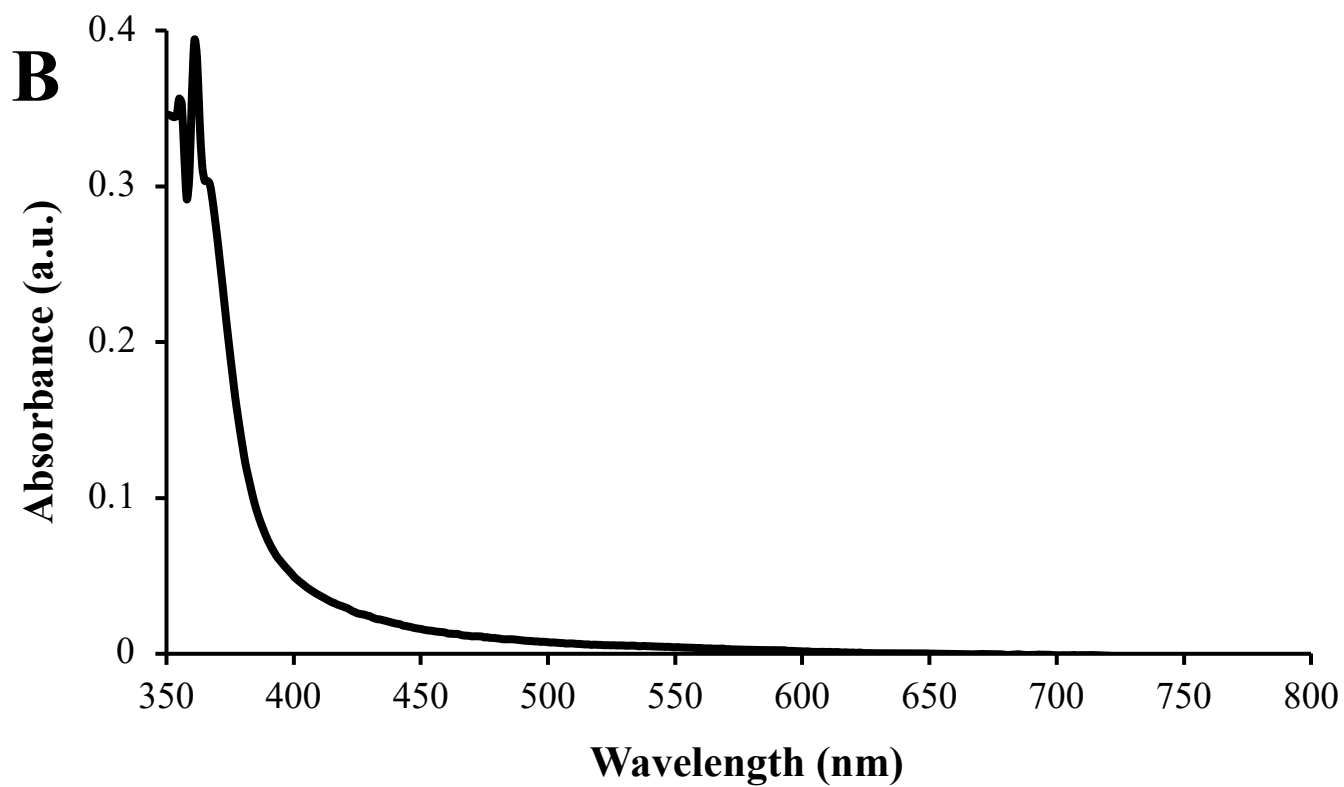
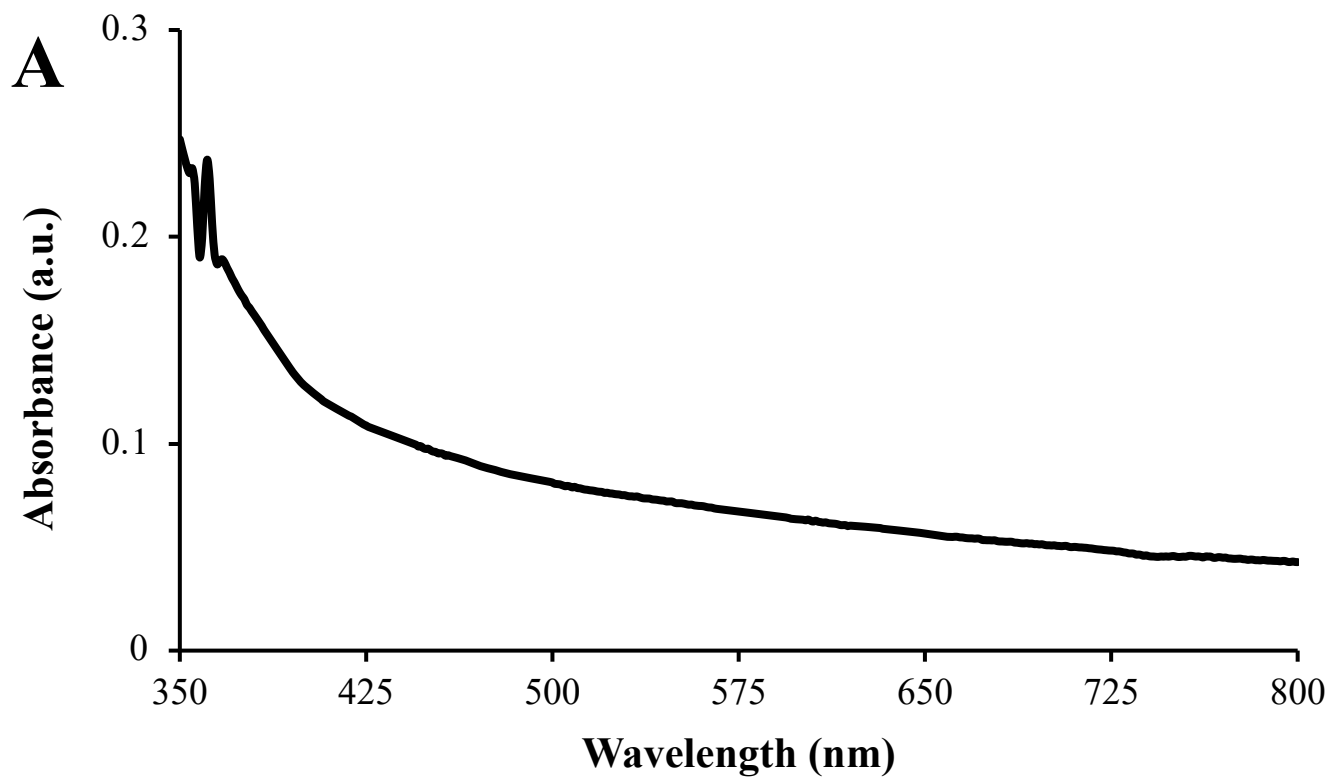


Figure S25. UV-Vis spectra of **(A) thiacloprid** (113 mM) and **(B) clothianidin** (67 mM) in tetrahydrofuran.

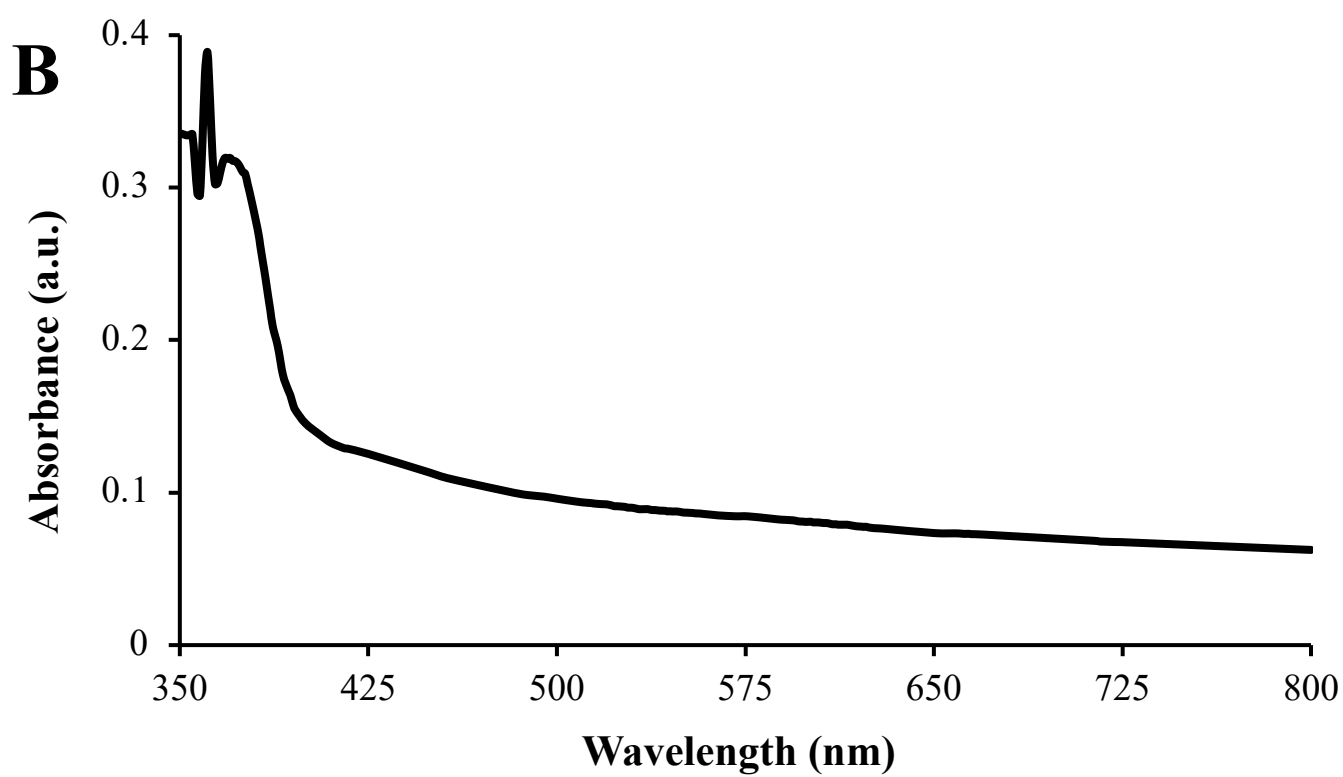
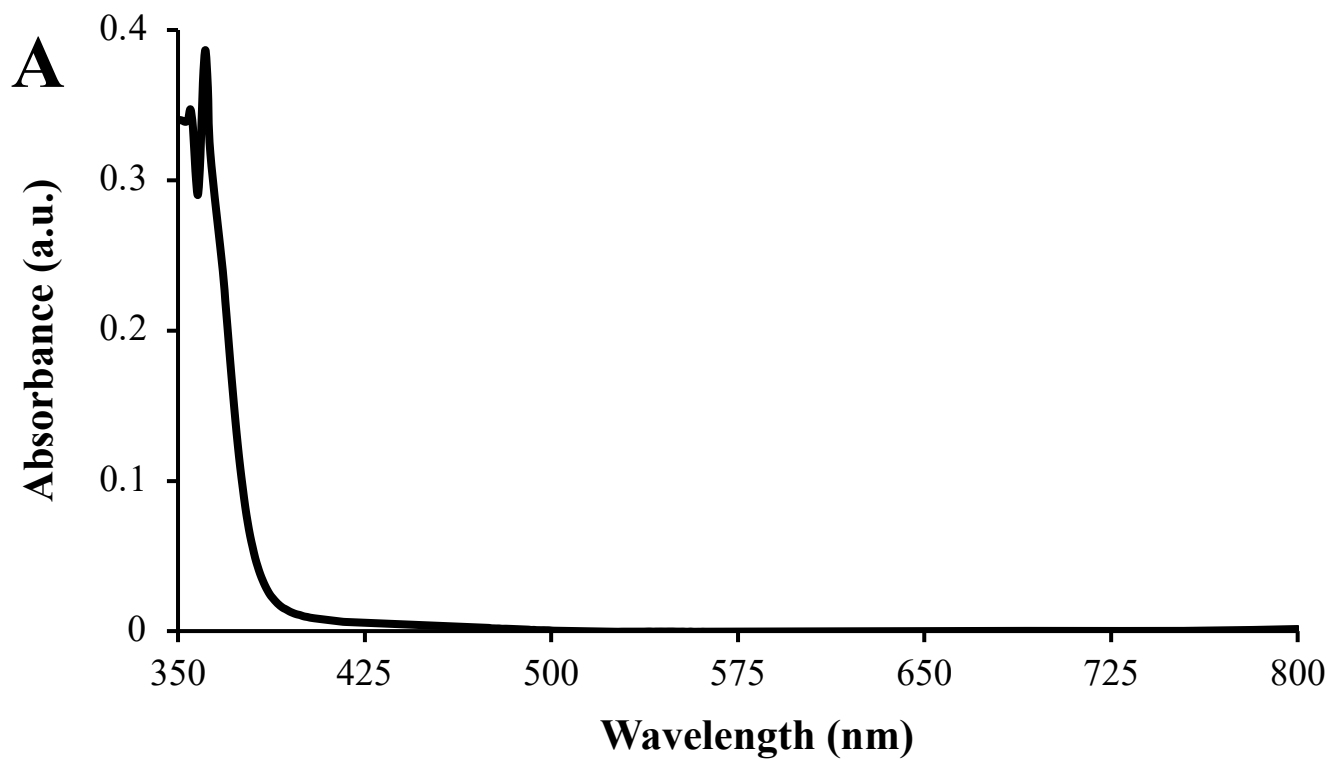


Figure S26. UV-Vis spectra of **(A) imidacloprid (50 mM)** and **(B) thiamethoxam (70 mM)** in tetrahydrofuran.

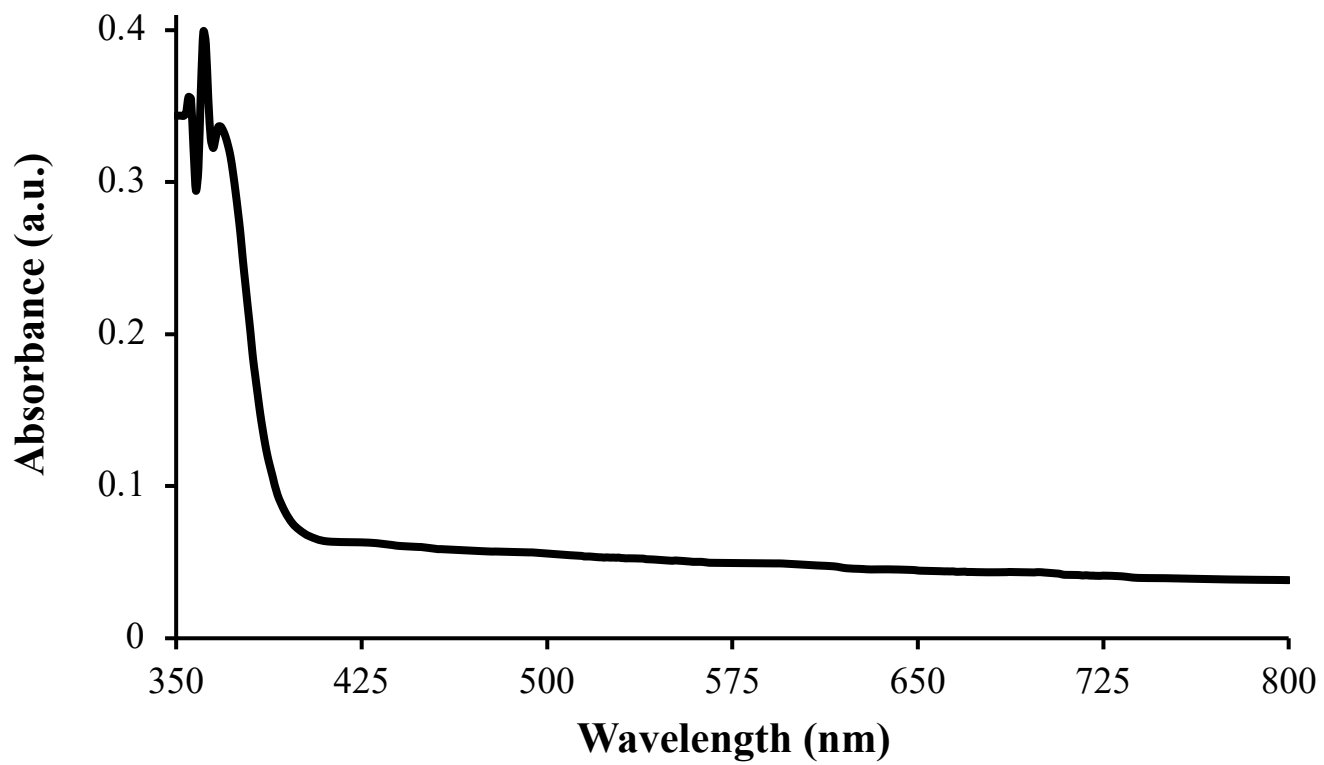


Figure S27. UV-Vis spectrum of **dinotefuran** (75 mM) in tetrahydrofuran.

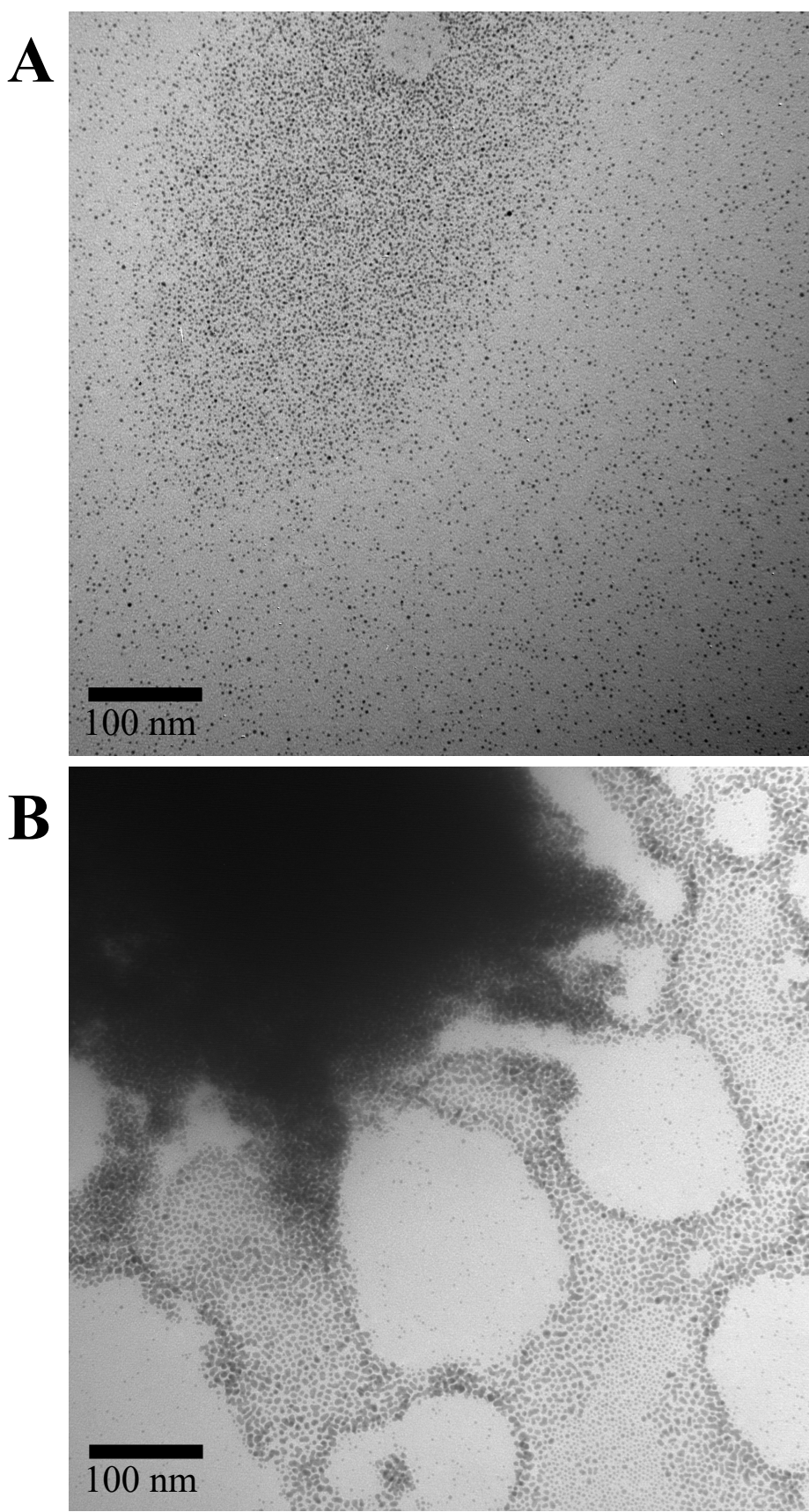


Figure S28. TEM images of *f*-MPCs (A) before and (B) 2 minutes after the addition of imidacloprid (50 mM). Images are representative of multiple sites imaged of each sample.

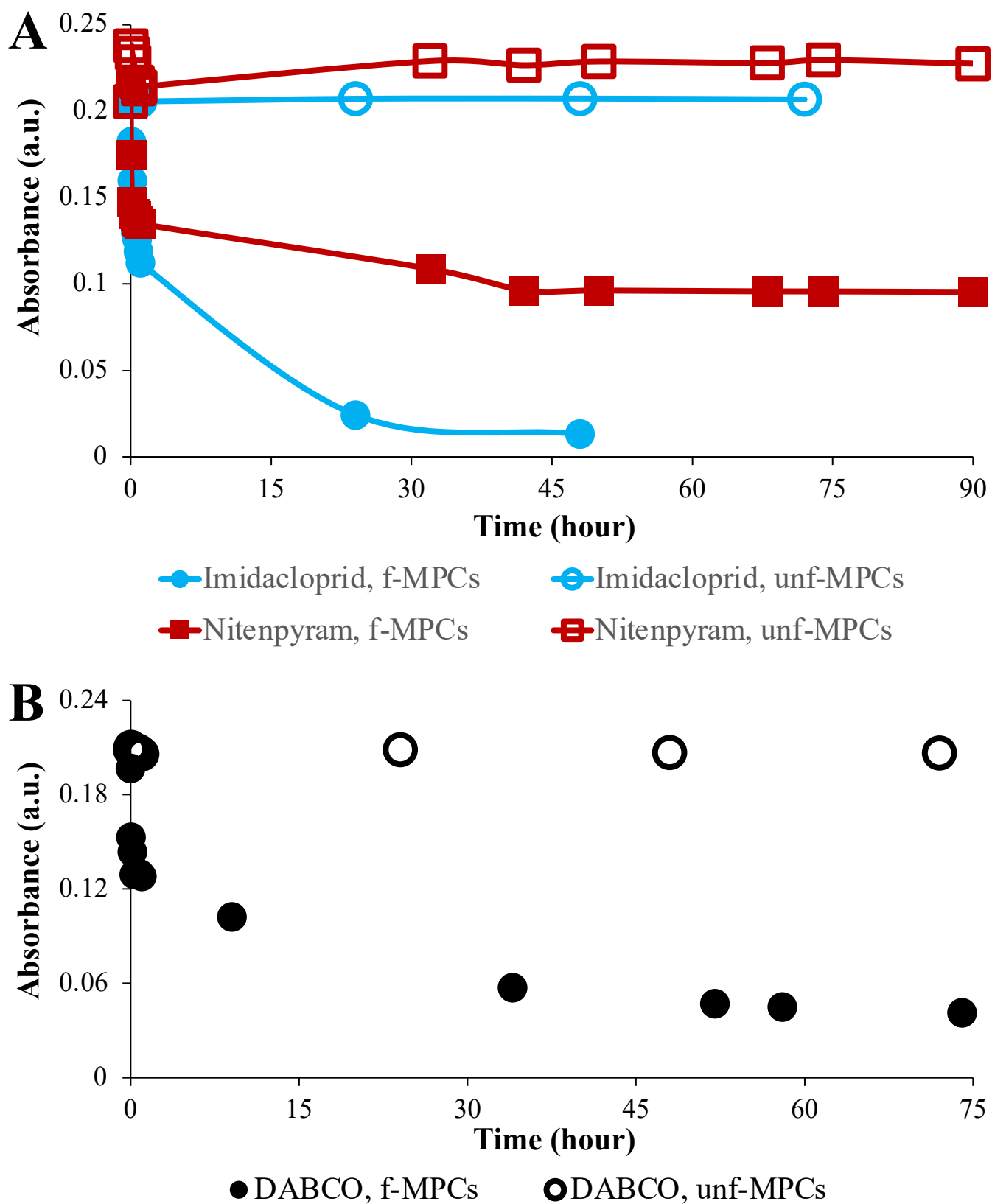


Figure S29. Spectroscopic tracking of $\text{Abs}_{@518\text{nm}}$ as a function of time of the mixtures of either *f*-MPCs or *unf*-MPCs exposed to **(A)** either **imidacloprid** and **nitenpyram** (longer time-scale analysis) or **(B)** DABCO (control).

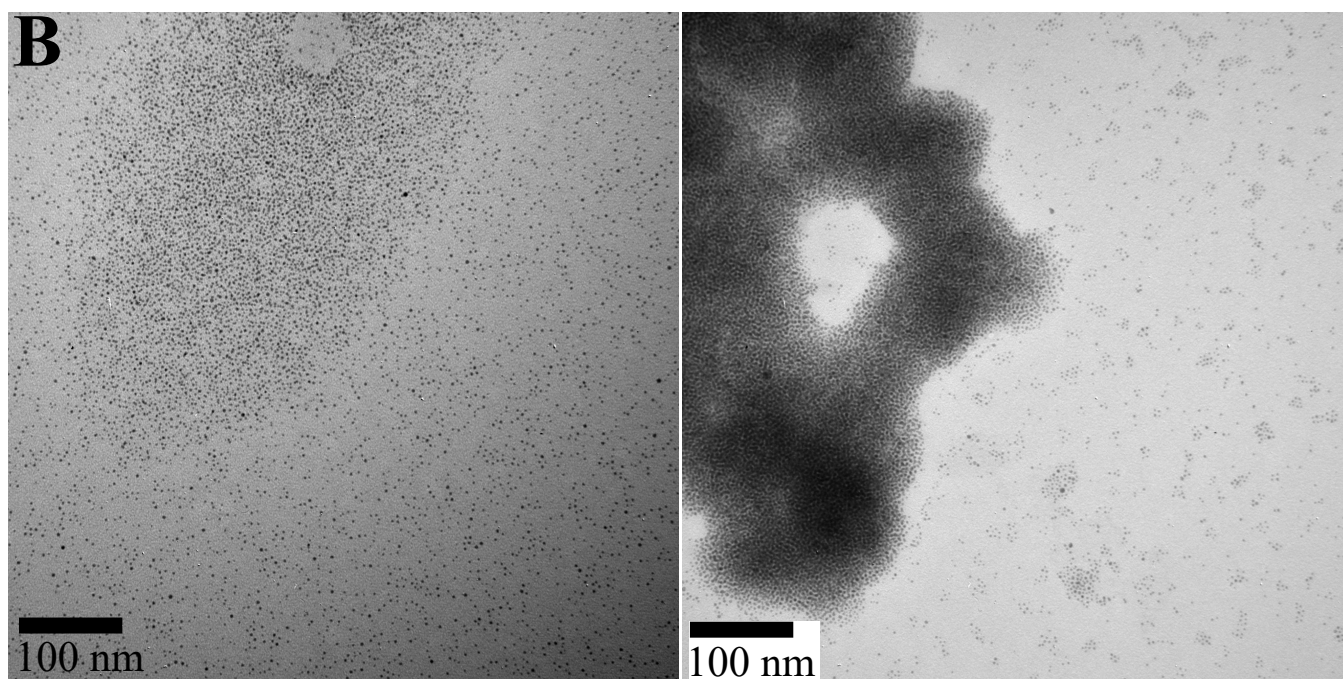
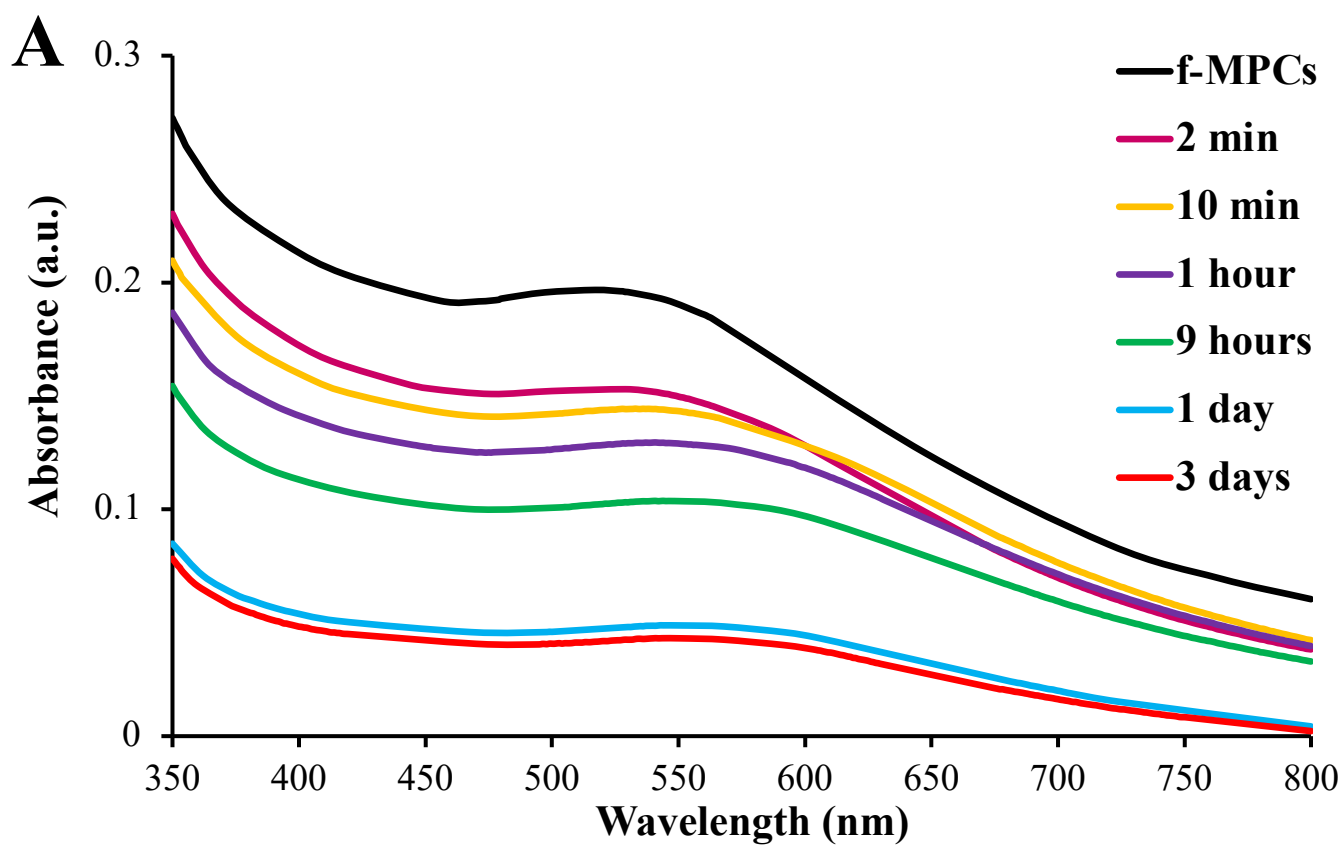


Figure S30. (A) UV-Vis spectra of *f*-MPCs in toluene upon exposure to DABCO (1 mM) over time. (B) TEM images of *f*-MPCs (left) before and (right) 5 minutes after DABCO addition.

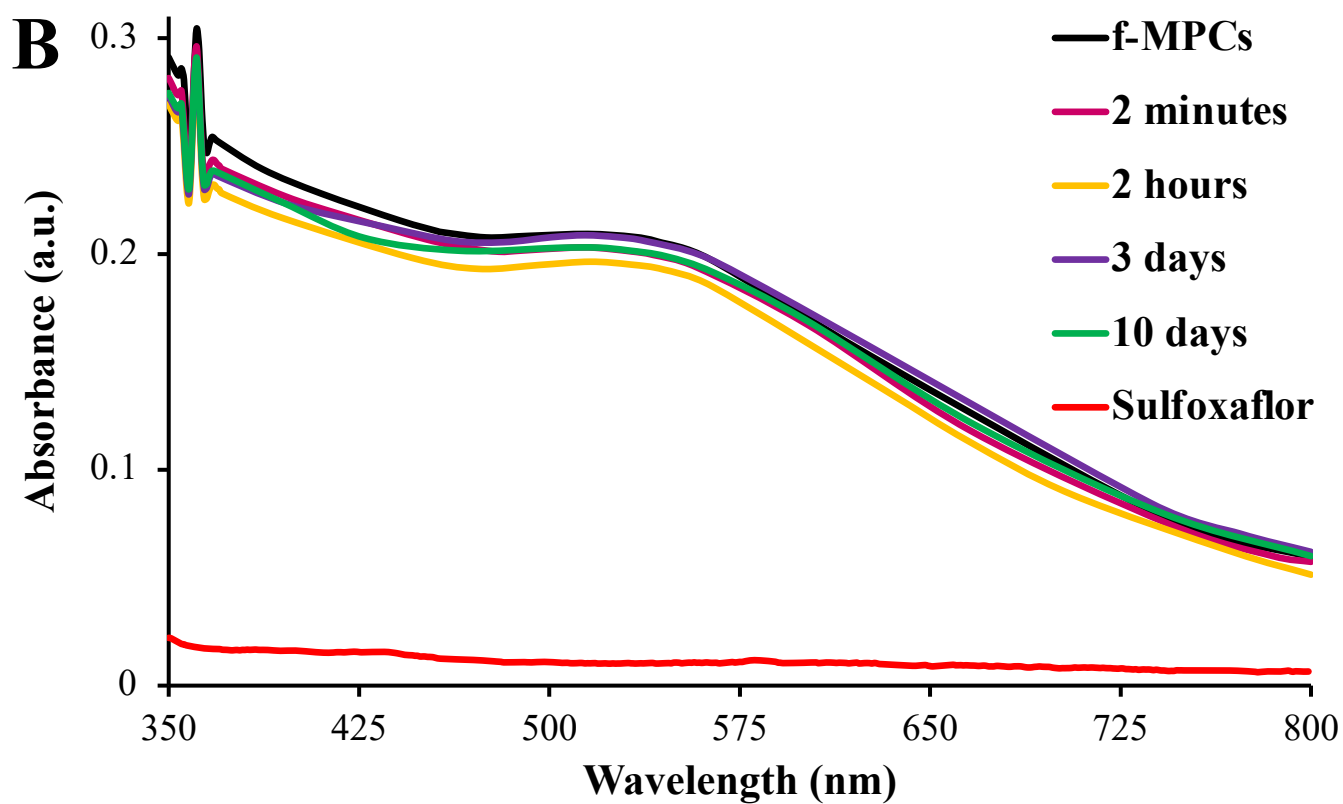
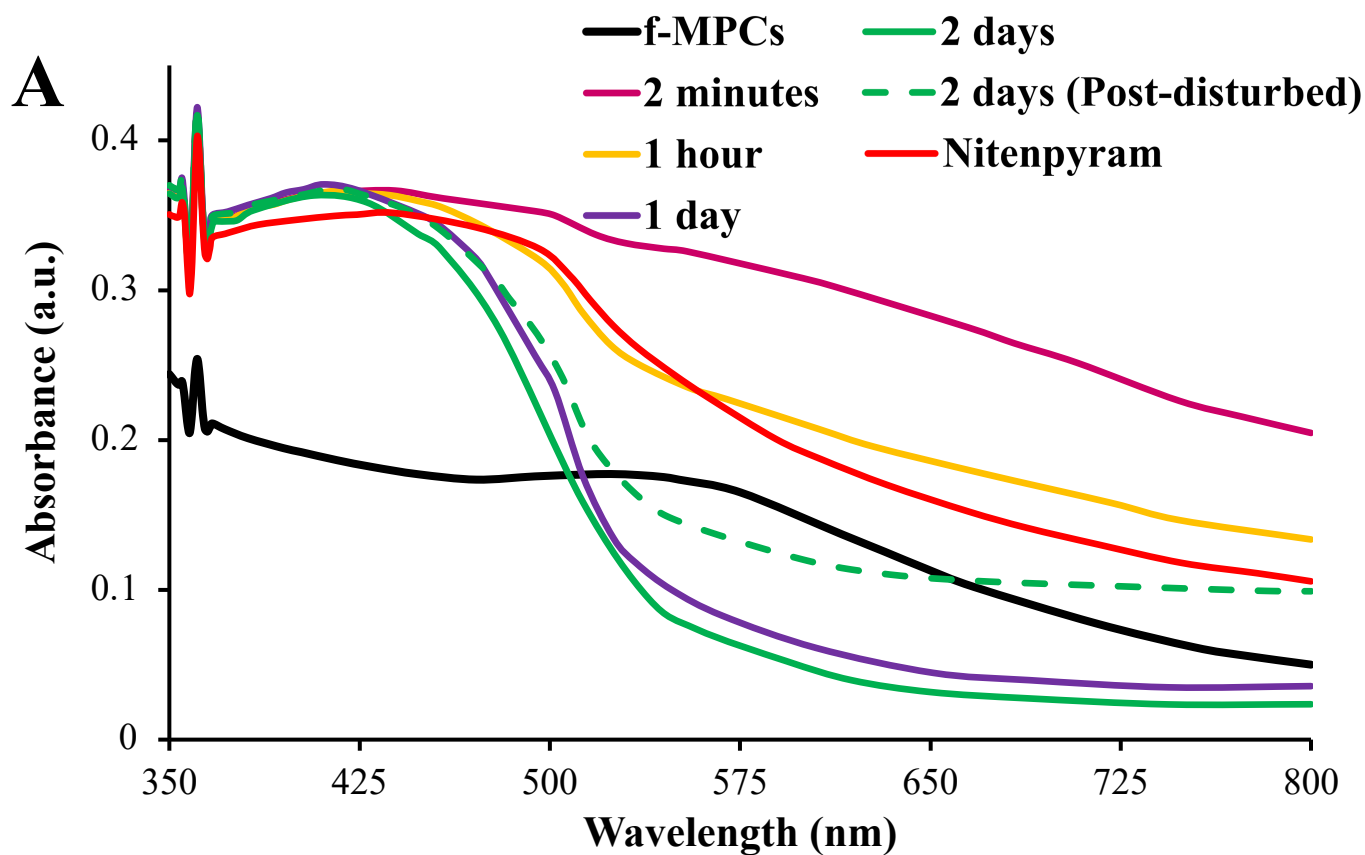


Figure S31. UV-Vis spectra of *f*-MPCs in THF upon exposure to (A) nitenpyram (200 mM) and (B) sulfoxaflor (72 mM) over time.

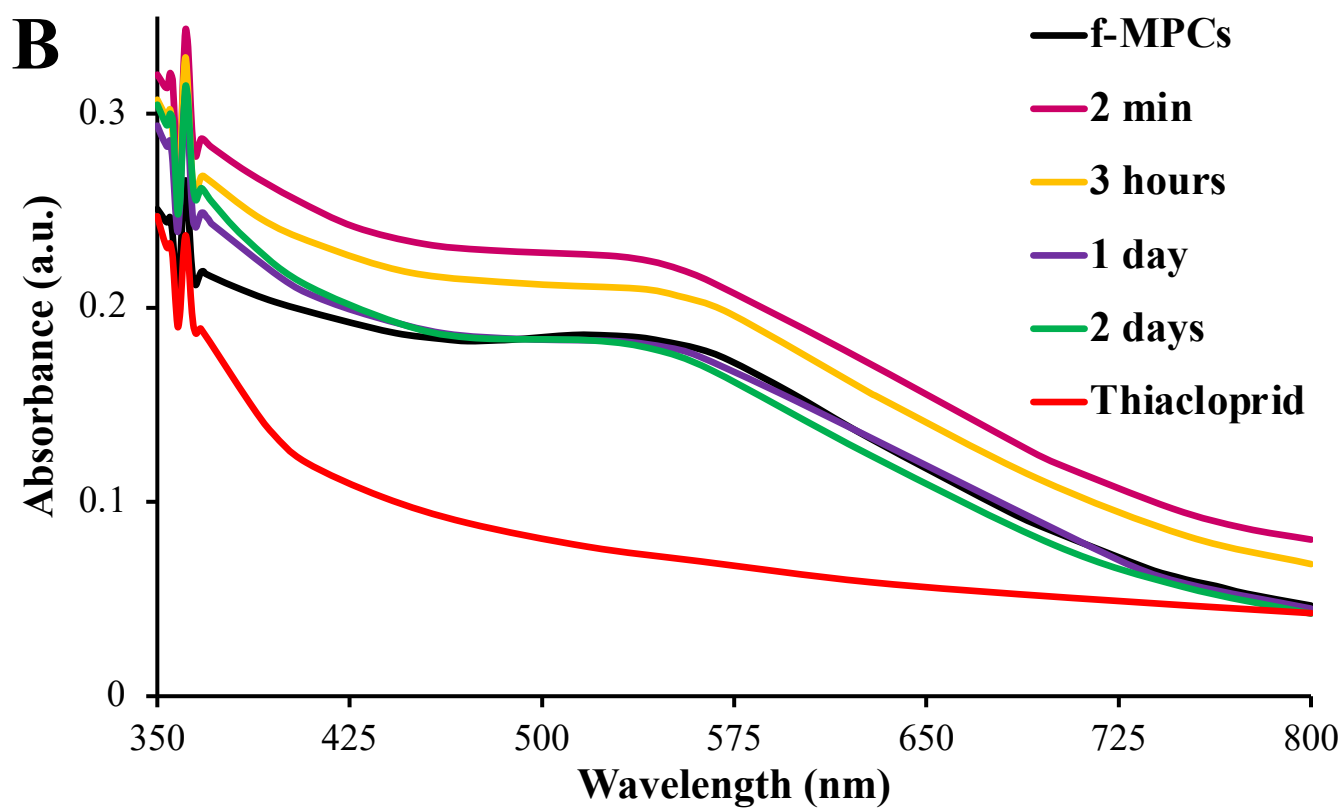
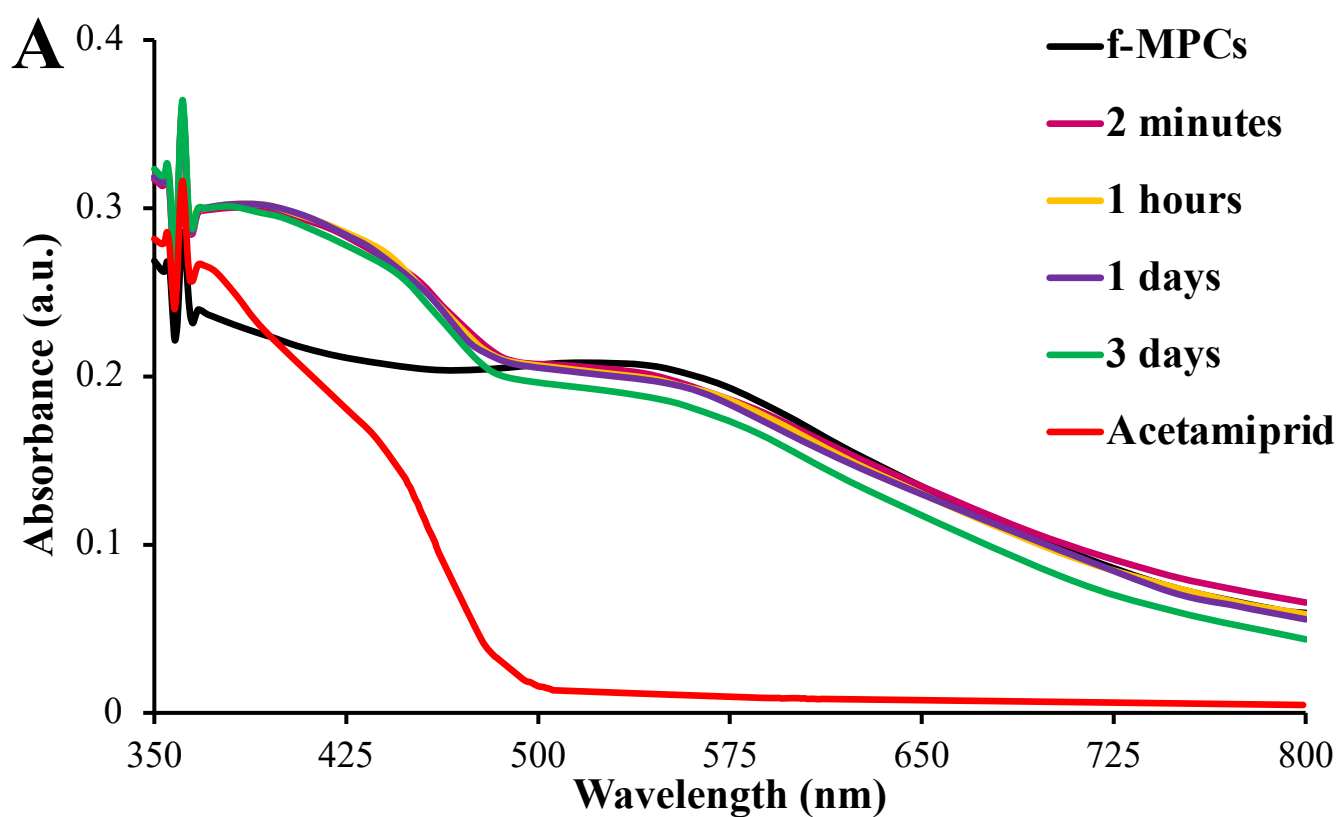


Figure S32. UV-Vis spectra of *f*-MPCs in THF upon exposure to (A) acetamiprid (75 mM) and (B) thiacloprid (113 mM) over time.

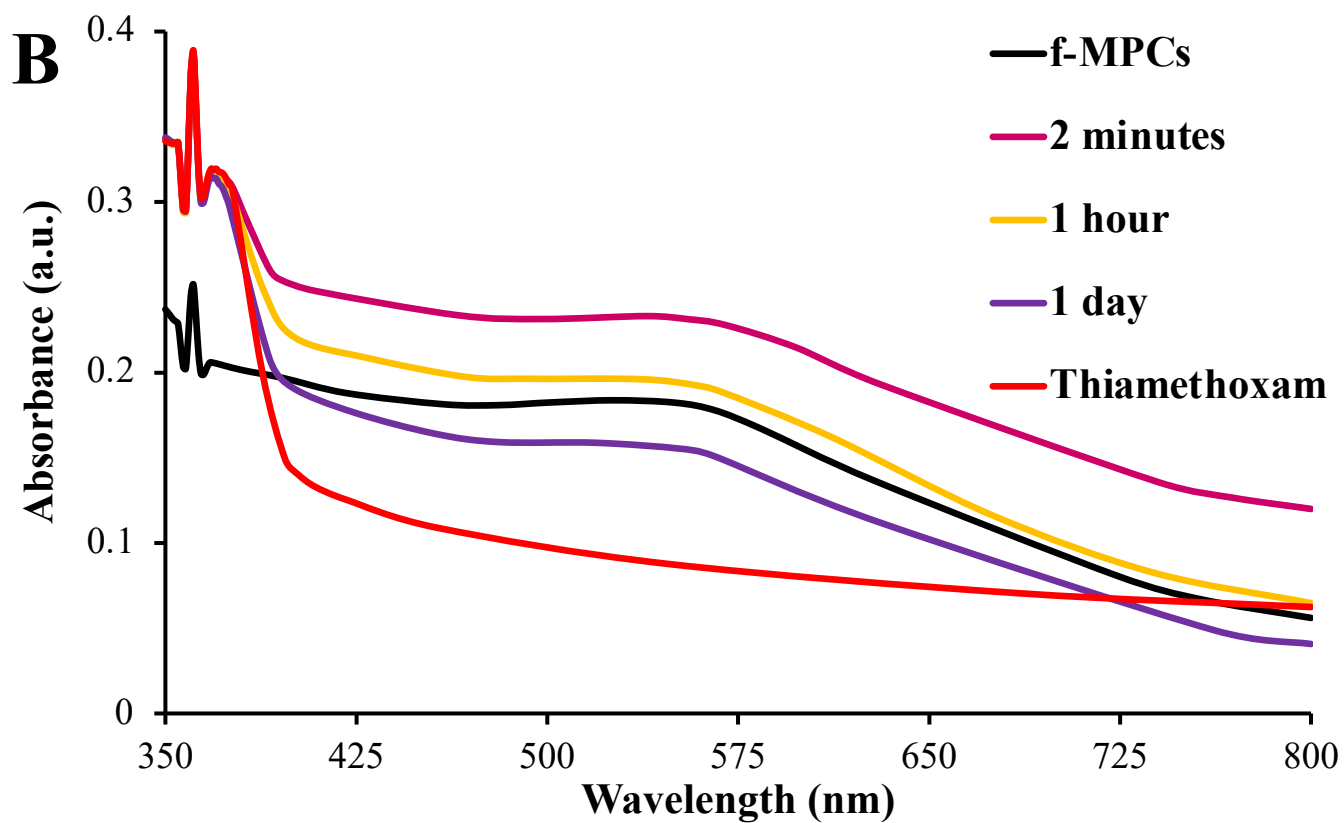
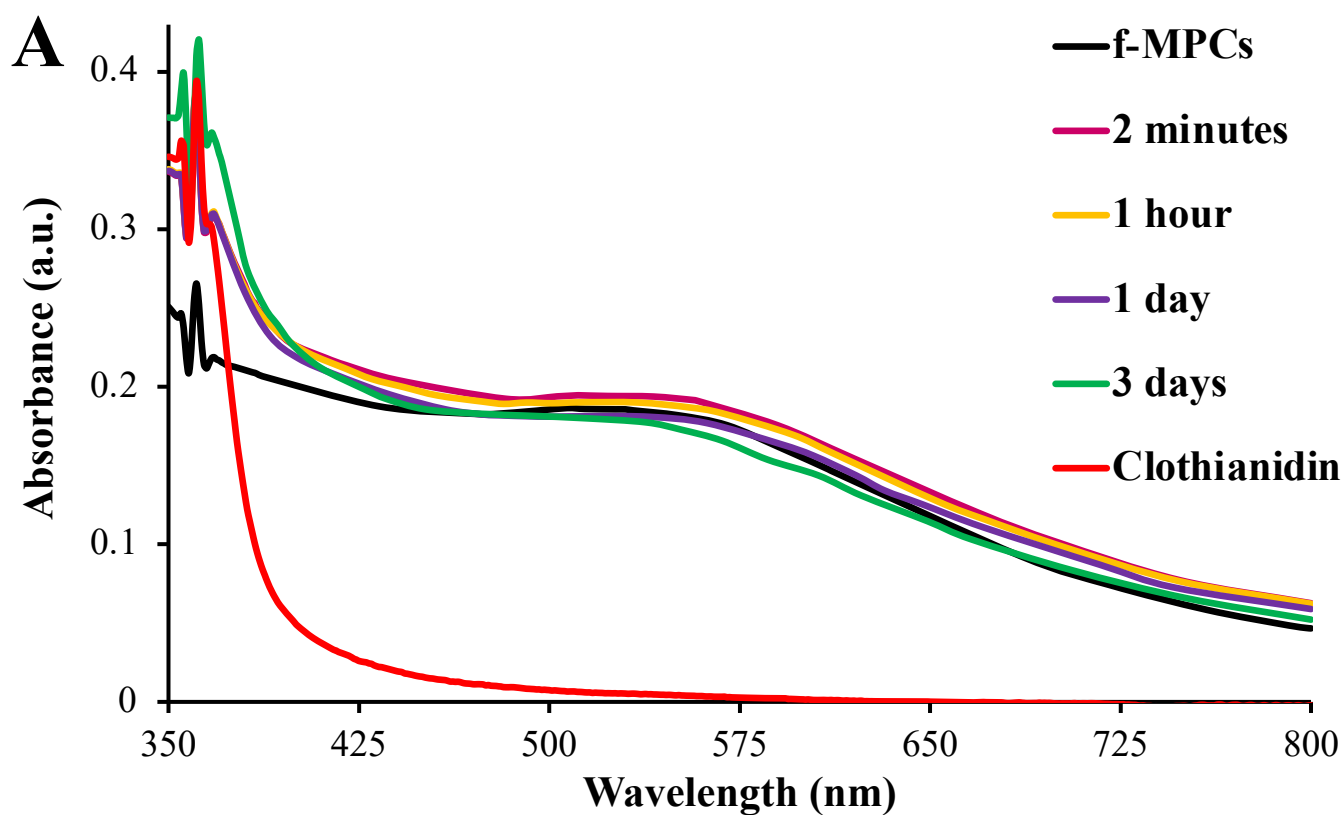


Figure S33. UV–Vis spectra of *f*-MPCs in THF upon exposure to (A) clothianidin (67 mM) and (B) thiamethoxam (50 mM) over time.

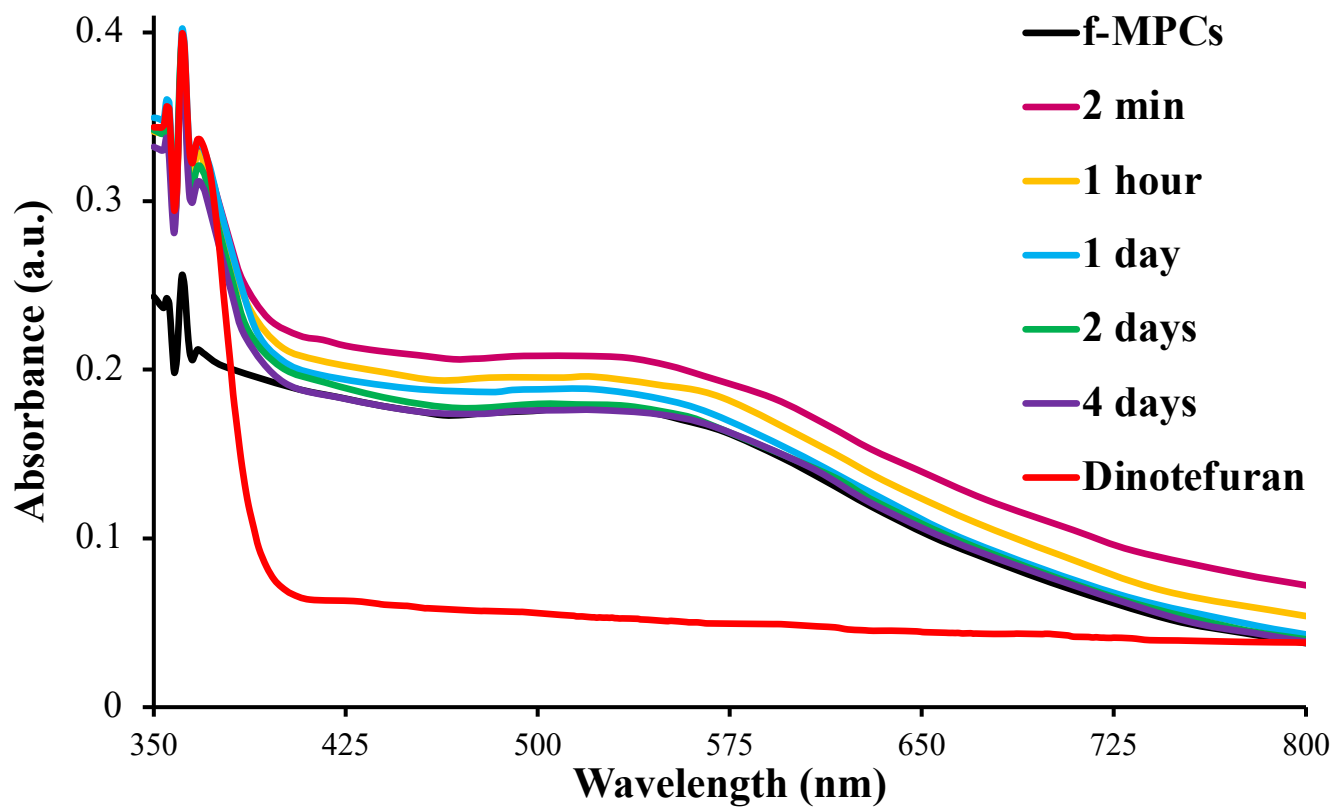


Figure S34. UV-Vis spectra of *f*-MPCs in THF upon exposure to dinotefuran (73 mM) over time.

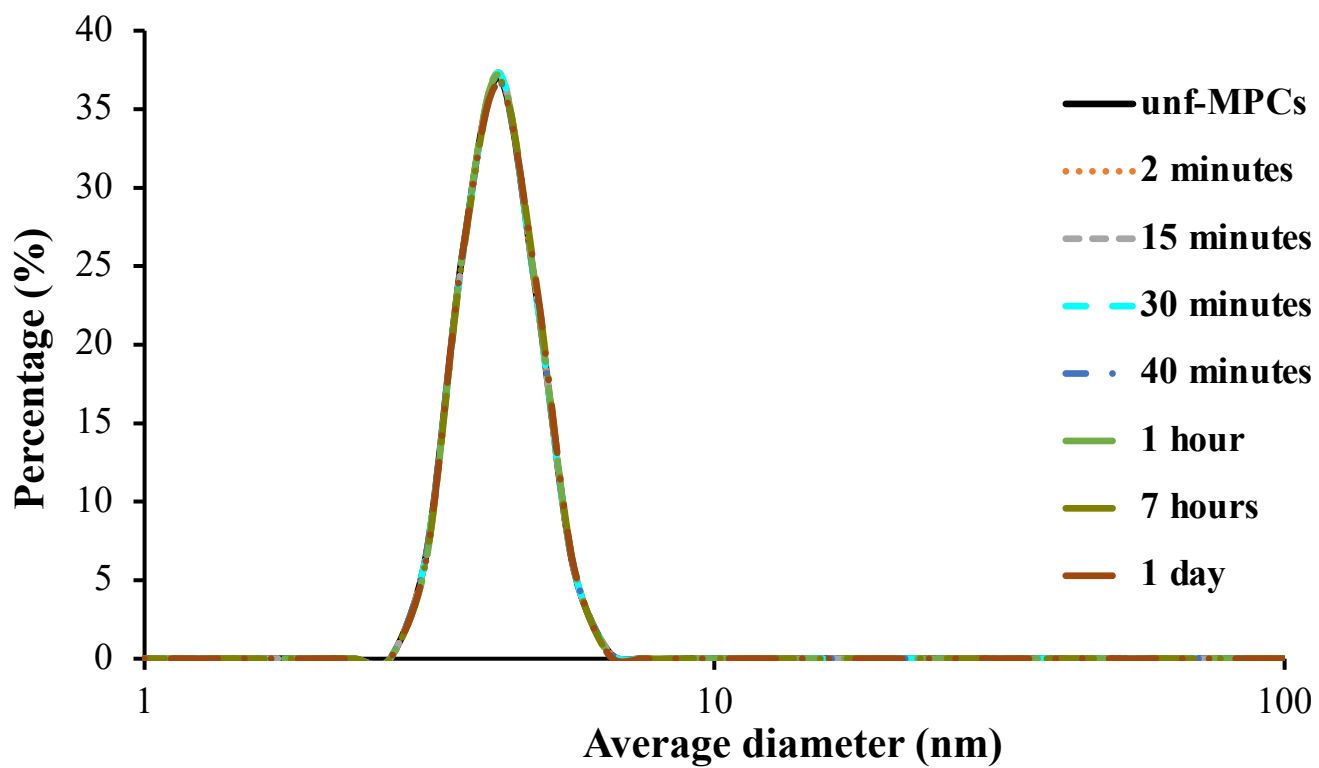


Figure S35. DLS results of *unf*-MPCs in THF ($Abs_{@518} = 0.20$ a.u.) before and after the addition of imidacloprid (12 mM) as a function of time.

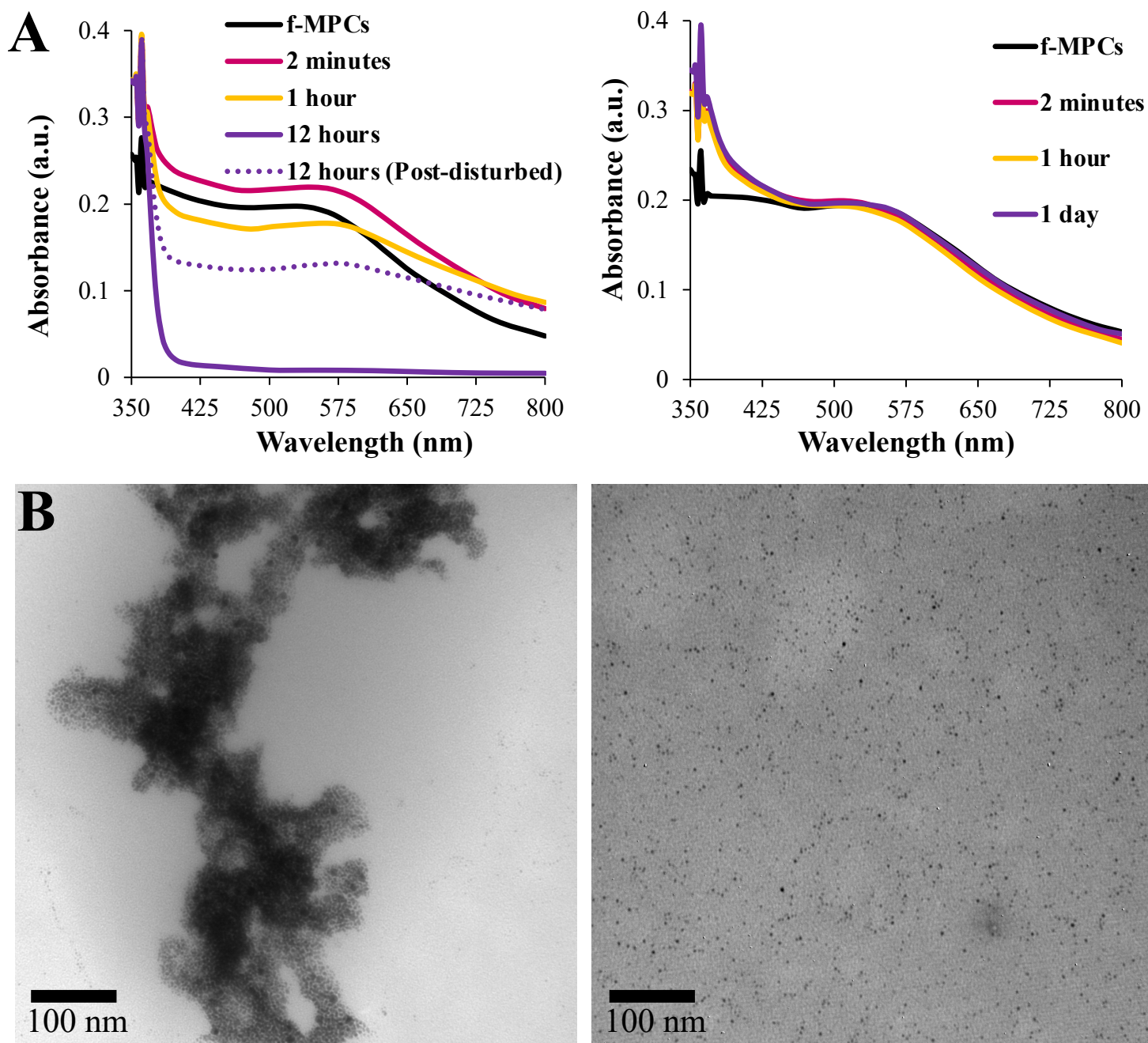


Figure S36. (A) UV-Vis spectra and (B) corresponding TEM images (at 1 hour) of *f*-MPCs upon exposure to other neonicotinoid compounds (50 mM clothianidin and 50 mM acetamiprid) in the presence (*left*) and absence (*right*) of 50 mM imidacloprid over time.

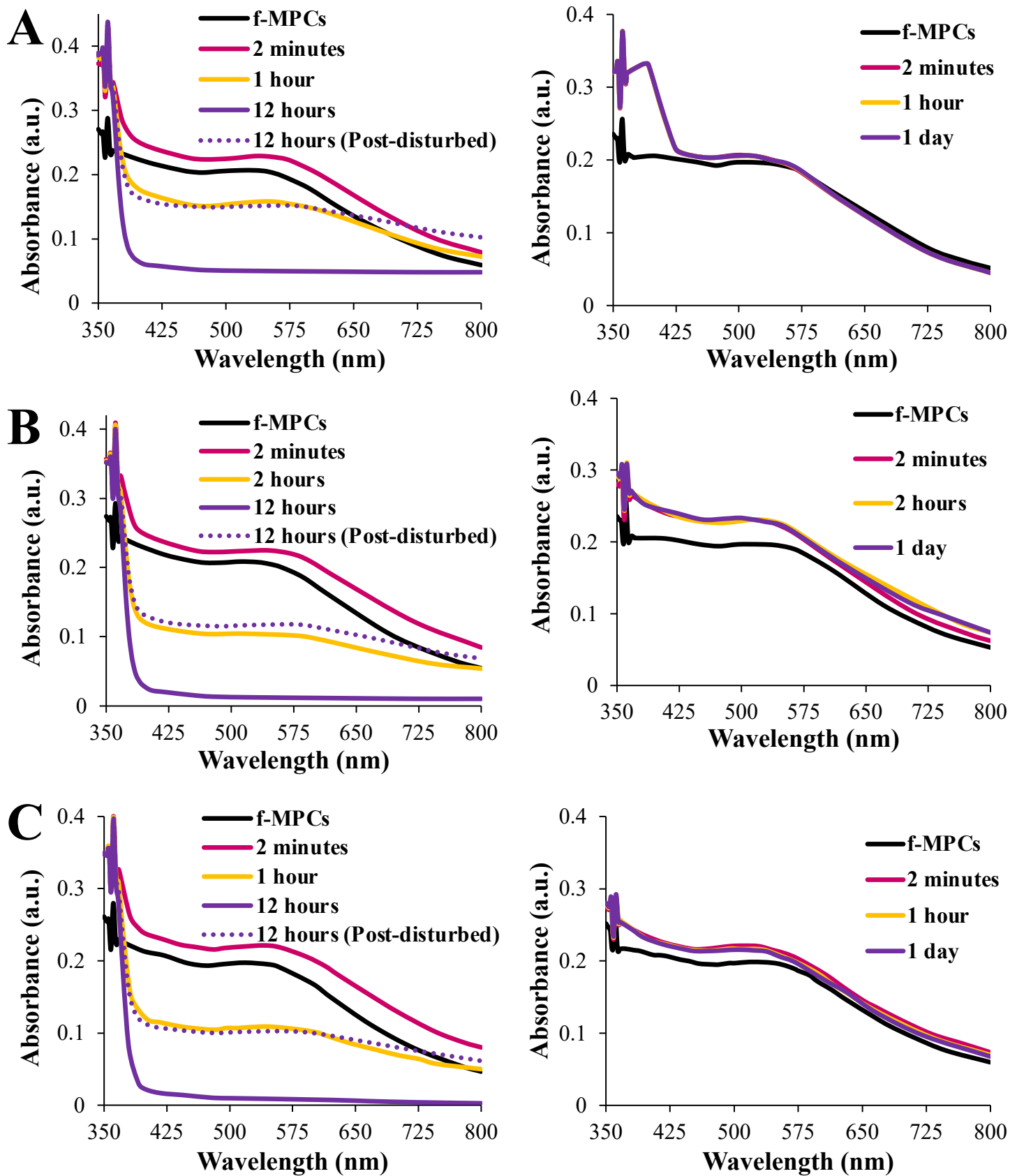


Figure S37. UV-Vis spectra of *f*-MPCs upon exposure to other organophosphate pesticides (A) 50 mM parathion, (B) 50 mM chlorpyrifos, and (C) carbamate pesticide carbaryl (50 mM) in the presence (*left*) and absence (*right*) of 50 mM imidacloprid over time.

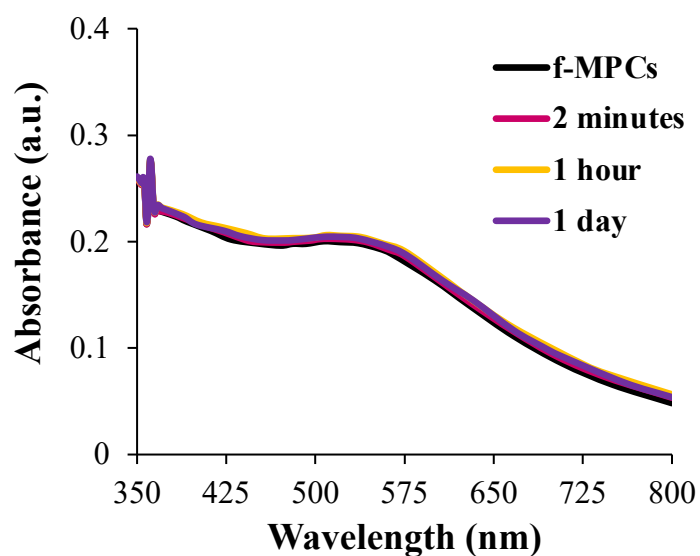
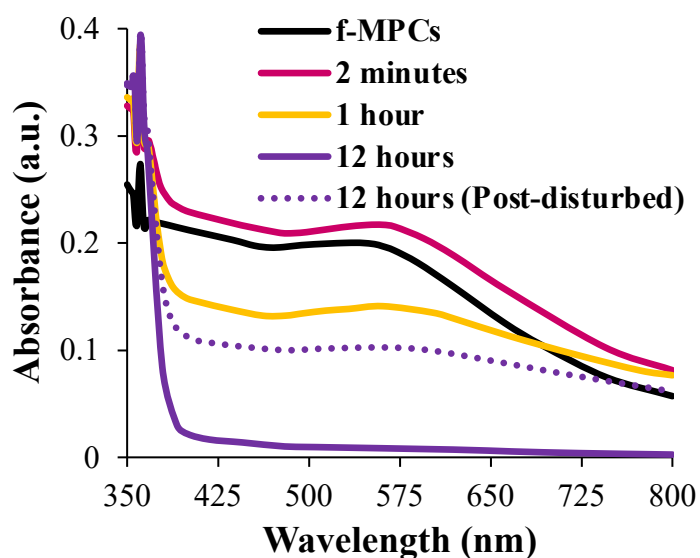


Figure S38. UV-Vis spectra of *f*-MPCs with a common plasticizer found in the environment (50 mM dioctyl phthalate) in the presence (*left*) and absence (*right*) of 50 mM imidacloprid over time.

References

1. Frisch, M. J.; Trucks, G. W.; Schlegel, H. B.; Scuseria, G. E.; Robb, M. A.; Cheeseman, J. R.; Scalmani, G.; Barone, V.; Petersson, G. A.; Nakatsuji, H. *Gaussian 16*, Gaussian Inc.: Wallington, CT, 2016.
2. Zhao, Y.; Truhlar, D. G., The M06 suite of density functionals for main group thermochemistry, thermochemical kinetics, noncovalent interactions, excited states, and transition elements: two new functionals and systematic testing of four M06-class functionals and 12 other functionals. *Theor Chem Acc* **2008**, *120* (1-3), 215-241.
3. Dunning, T. H., Gaussian-Basis Sets for Use in Correlated Molecular Calculations .1. The Atoms Boron through Neon and Hydrogen. *J Chem Phys* **1989**, *90* (2), 1007-1023.
4. Kendall, R. A.; Jr., T. H. D.; Harrison, R. J., Electron affinities of the first-row atoms revisited. Systematic basis sets and wave functions. *The Journal of Chemical Physics* **1992**, *96* (9), 6796-6806.
5. Peterson, K. A.; Shepler, B. C.; Figgen, D.; Stoll, H., On the Spectroscopic and Thermochemical Properties of Clo, Bro, Io, and Their Anions. *J Phys Chem A* **2006**, *110*, 13877-13883.
6. Stoll, H.; Metz, B.; Dolg, M., Relativistic Energy-Consistent Pseudopotentials--Recent Developments. *J Comput Chem* **2002**, *23*, 767-78.
7. Tomasi, J.; Mennucci, B.; Cammi, R., Quantum Mechanical Continuum Solvation Models. *Chem Rev* **2005**, *105*, 2999-3094.
8. Donald, K. J.; Wittmaack, B. K.; Crigger, C., Tuning Sigma-Holes: Charge Redistribution in the Heavy (Group 14) Analogues of Simple and Mixed Halomethanes Can Impose Strong Propensities for Halogen Bonding. *J Phys Chem A* **2010**, *114*, 7213-7222.
9. Donald, K. J.; Tawfik, M., The Weak Helps the Strong: Sigma-Holes and the Stability of Mf4 Center Dot Base Complexes. *J Phys Chem A* **2013**, *117*, 14176-14183.
10. Parker, A. J.; Stewart, J.; Donald, K. J.; Parish, C. A., Halogen Bonding in DNA Base Pairs. *Journal of the American Chemical Society* **2012**, *134*, 5165-5172.
11. Tawfik, M.; Donald, K. J., Halogen Bonding: Unifying Perspectives on Organic and Inorganic Cases. *J Phys Chem A* **2014**, *118*, 10090-10100.
12. Dang, Q. M.; Simpson, J. H.; Parish, C. A.; Leopold, M. C., Evaluating Halogen-Bond Strength as a Function of Molecular Structure Using Nuclear Magnetic Resonance Spectroscopy and Computational Analysis. *J Phys Chem A* **2021**, *125* (42), 9377-9393.